Master Thesis in Theoretical Physics
Utrecht University

Order-Disorder Transition on a Range-3 Ising Model on the Square Lattice

---

Author:
Rodolfo Subert

Supervisors:
prof.dr. Bela M. Mulder
prof.dr. René H.H.G. van Roij

Utrecht, 2021

Abstract

The Ising model is arguably the most studied model in the history of physics, yet it is not fully understood in all its facets. In the present thesis we will focus on the frustration effects induced by long range, competing anti-ferromagnetic interactions. To study this behaviour, we consider a minimal model retaining the phenomenology: the range-3 Ising model on the square lattice. Previous investigation highlighted the role of the third range coupling in tuning the infinitely many modulated phases. Our approach relies on a fresh take on the standard Mean Field Theory framework. We derive an infinite set of self-consistency equations and show that the solutions depend solely on the Fourier transform of the interaction neighbour through the wave vectors available on the lattice. Each of the infinite wave vectors defines a modulated phase of the system as a periodic magnetization pattern. Constraining the system in Periodic Boundary Conditions, forces only a finite set of modes to define a phase. In the present work, we will first provide a systematic way to enumerate all the phases up to an arbitrary size N of the square lattice. Then, we will show that the region of stability of the high temperature paramagnetic phase is a convex polytope, whose faces are in a one-to-one relation with the underlying periodicities, modulo the point group symmetry of the lattice. The polytopes can be explicitly determined using a standard vertex enumeration procedure and, on the infinite lattice, through a convex body reconstruction. The onset of complexity is found in the $J_3 < 0$ region, while for positive J_3 our results correctly reduce to the range-2 model, exhibiting only three phases. Finally, we validate the theoretical framework with Monte Carlo simulations, once again enforcing the expected phases with PBC constraints. Our analysis correctly predicts the dominant mode that bifurcates from the disorder region beyond each face of the polytopes.

Contents

Chapter 1

Introduction

Lattice systems with interacting spins arose in the past century as a paradigm to study complex collective behaviour. The dynamic of these systems is typically governed by an Hamiltonian, that encodes all the information on the interactions. Originally employed in the field of condensed matter, this approach is now ubiquitous throughout the natural sciences and beyond. Escaping its original context of ferromagnetism, lattice models are nowadays studied in highly varied and sometimes exotic settings and successfully applied to describe highly diverse fields, ranging from language modelling[1] to quantum gravity[2], up to the studies for their own sake with a recent interest in universal models[3]. Our focus is on lattice Hamiltonians with competing antiferromagnetic interactions. The emerging order may be very complicated both in the number and the nature of the phases, which may arise as spatially modulated periodic magnetization patterns on the lattice. A comprehensive and shared paradigm in the study of modulated phases is still lacking, as many results are controversial[4] because they rely on numerical calculations and approximations, which explains the call by Per Bak[5] which states that it is *"of imperative importance"* the study of these phenomena.

Our original motivation is the development of a coarse grained model for the crystalline phases of DNA-coated colloidal particles[6], systems whose coupling parameters are experimentally tunable. To know beforehand what is the Hamiltonian that leads to a certain crystallization pattern would be of great importance to engineer materials with designed physical properties. Nonetheless, the versatility of lattice models, makes the study of modulated phases relevant beyond colloidal crystals. Other systems that exploit these kind of phenomena include periodic lattice distortions, charge-density waves[7], periodic arrangement of atoms in a host lattice[8] or spin-density waves[9]. The field of Iron Chalcogenids requires special mention, as we will be able to show magnetic ground states that exactly match the ground states recently found by Glassbrenner et al.[10] by different means.

We will provide a fresh perspective to study the onset of order on lattice Hamiltonians with competing interactions. The power of the theoretical framework that we propose lies in its versatility: it allows to include an arbitrary number of interactions on any lattice geometry of interest. Nonetheless, as it will become clear, it is limited to the order-disorder transition, the calculation of the full phase diagram (and of the ground states) is an NP problem and might intrinsically be uncomputable[11]. To illustrate our procedure, we will focus on the field free range-3 Ising model on the square lattice, the simplest geometry (square lattice), with the minimal dimension and the

minimal number of neighbours, necessary and sufficient[12] to exhibit an infinity of modulated phases as we will subsequently argue. The essential idea is that introducing an anti-ferromagnetic third neighbour interaction term in the Hamiltonian, the full symmetry point group of the lattice can be broken. To sort out the complexity of this infinite number of phases, we will work with finite systems, introducing an enumeration procedure to account for more and more complex phases, and eventually taking the whole, infinite square lattice.

Our intuition levarages and is built upon a century worth of literature. We will here review in historical order the groundwork underlying the development of our model. We begin reviewing the birth of the Ising model as it has been originally introduced, briefly mention the phenomenon of frustration as the mechanism that leads to multiple modulated phases. Next, we discuss key findings in systems exhibiting modulated phases. Ultimately, we will review previous investigations on both the range-2 and the range-3 Ising model with competing interactions.

1.1 Historical Background

The so called "Ising model" made its first appearance on *Zeitschrift für Physik*[13] in 1925, as discussed by Ernst Ising in his doctoral thesis. His calculations relied on an original intuition[14] by his supervisor, Wilhelm Lenz, which a few years earlier proposed a coarse grained model for ferromagnetism, which only retains the major local degree of freedom: spin orientation. In the absence of an external field, the average spin orientation at fixed temperature is affected only by its nearest neighbours. We expect to exist a critical temperature above which thermal fluctuations keep the system in a paramagnetic (disordered) phase and under which it is energetically convenient to establish long range order. Among the many historical reviews on the origin of the model we suggest the early work by Brush[15].

The Ising model is nowadays the "fruit fly" of statistical physics, the archetypal example to illustrate the quantitative nature of phase transitions and the constructionist paradigm of statistical physics. The emergence of collective behaviour is encoded in the microscopic physical mechanisms (reductionist hypothesis), but does not trivially follow from it. The essential idea, better illustrated by P.W. Anderson[16], is that *"in the so called $N \to \infty$ limit of large systems (on our own, macroscopic scale) it is not only convenient but essential to realize that matter will undergo mathematically sharp, singular "phase transitions" to states in which the microscopic symmetries, and even the microscopic equations of motion, are in a sense violated."*

A century after Lenz seminal work, the Ising model is arguably the most studied model in statistical physics, a quick search on Google Scholar gives more than 420.000 hits[1]. Its popularity resides both in its simplicity and versatility. It exploits the simplest possible local symmetry $\mathbb{Z}_2$, which makes it the model for which most exact results are available. The most studied equivalent formulations are arguably the grand canonical lattice gas and the binary alloys, where the binary orientations are respectively interpreted as presence or absence of particles, and as different particles species. Although these would be the natural formulation that inspired the present work, for the sake of simplicity we will stick to the language of magnetism.

[1] Google Scholar, `scholar.google.com`, [Accessed: April 2021].

In its original formulation the nearest neighbour Ising Hamiltonian couples spins on adjacent lattice sites i, j with a coupling parameter J and takes the form

$$H = -J \sum_{\langle i,j \rangle} \sigma_i \sigma_j, \tag{1.1}$$

where the angular bracket denotes nearest neighbours and the minus sign is conventional such that positive J favours alignment of neighbouring spins and negative J favours anti-alignment. We start focusing on the ferromagnetic case. In a one dimensional system the competition between energy and entropy favours the creation of anti-aligned neighbouring pairs (domain walls). In other words, thermal fluctuations are too strong to give rise to finite temperature[2] spontaneous symmetry breaking, to a fully aligned state. For lattices in two and more dimensions the same is not true and the system effectively undergoes a phase transition. Many scientists contributed to this important result in the Thirties and Fourties of the 20th century: the first to recognize a phase transition had been Bragg and Williams[18], who in 1934, neglecting correlations, extended the tool now known as mean field theory to lattice models. However, their result needed further refinement, as the same technique applied to the one dimensional lattice would wrongly predict a phase transition. An improvement on this is due to Bethe and Peierls[19], whose argument has been later formalized by Griffiths[20][3]. The underlying idea is that accounting for further spin correlations, in a simple back of the envelope calculation, shows how the entropic cost to create a domain wall is lower than then the energy loss, such that, under a certain temperature the system will spontaneously magnetize. This is more general, the critical dimension for systems exploiting discrete local symmetries is $d = 2$[4]. In 1943 Onsager[22] proposed the celebrated exact derivation (later refined by Kaufmann[23][24]) of the diverging correlation functions in terms of elliptic integrals. Finally Yang[25] in 1950, leveraging on Onsager's result, computed the exact magnetization, with what he remembers as the longest calculation of his career.

More intriguing phenomena appear for negative, anti-ferromagnetic interactions. The ferromagnetic case is peculiar, as geometry only affects the critical temperature. The global ground state is trivially achieved on any conceivable lattice when all the spins are aligned, which trivially implies that each site is aligned with all the neighbours. This does not hold if we consider negative values of the coupling parameter J. In this scenario a single spin contribution is minimal when it is anti-aligned to all its neighbours. Whether this implies that the global and local ground states coincide depends on the topology of the underlying lattice. As shown in Fig.1.1a, on the square lattice all sites can simultaneously be anti-aligned[5] with their neighbours. The chessboard-like global ground state is called Neel ordered state[26]. The same, however, does not hold for the triangular lattice. As shown in Fig.1.1b, the topology forbids even the minimal plaquette of three spins, to simultaneously minimize the energy of each of its three bonds. This leads to a global ground state degenerate with

[2] Observed in lab Birgeneau and Shirane[17].

[3] The cited proof depends on the boundary conditions and the dimensionality, nonetheless it has been generalized to the infinite lattice and to higher dimensions.

[4] To be compared with local continuous symmetry, whose critical dimension, as proved by Mermin and Wagner[21], is $d = 3$.

[5] The underlying reason being that one can partition the lattice in two disjoint sub-lattices.

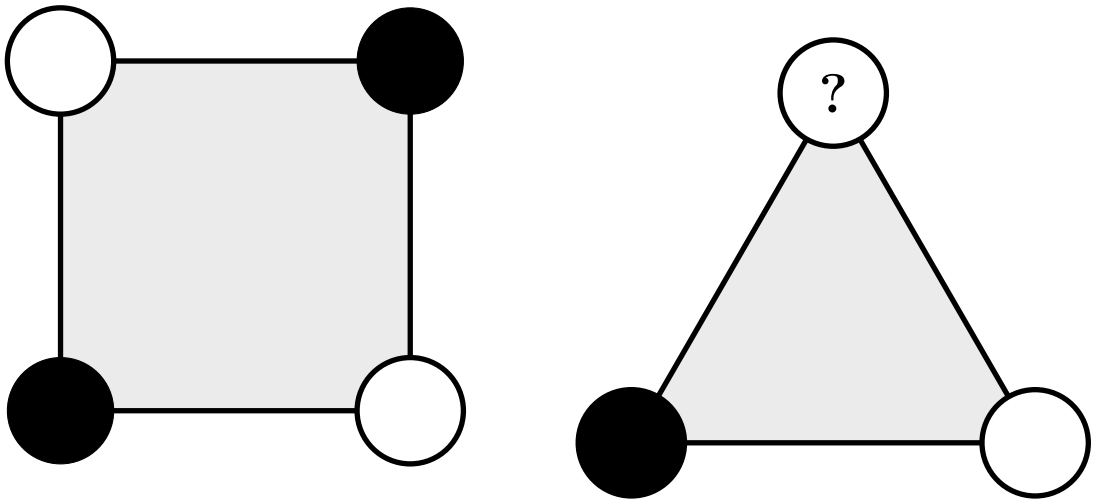

(A) Ground state of the anti-ferromagnetic nearest neighbours Ising Hamiltonian. Each spin is anti-aligned with all its four neighbours.

(B) Frustration on the anti-ferromagnetic triangular lattice. The energy is degenerate with respect to the orientation of the upper site.

FIGURE 1.1: Comparison of a square and triangular anti-ferromagnets on their minimal plaquette. Solid circles represent up spins, empty circles represent down spins.

respect to individual spin flips. This phenomenon is known as *frustration*. The term was coined in 1977 by G. Toulouse and Vanneminus[27][28]. The Ising model on the triangular lattice was originally investigated by Wannier[29] in 1950, who, exploiting an Onsager-Kaufmann like calculation, was able to explicitly quantify the degree of frustration in terms of a zero temperature, residual entropy. We refer to the phenomena occurring on triangular kind of systems as geometrical frustration[30]. To be contrasted with interaction frustration, the phenomenon of our interest that arises in presence of long range, competing, anti ferromagnetic interactions, as shown in the lattice Fig.1.3b.

Our purpose is to construct the minimal model for which the square lattice with isotropic interactions exhibits an analogous behaviour. To this end we will have to introduce up to range three anti-ferromagnetic couplings. Ising models with competing long range interactions have been extensively studied during a flurry of activity in the Seventies and Eighties, with more sparse work in recent years. Most of the effort focused on anisotropic interactions to match the experimental observations of anistropic modulations observed in the crystal structure of Erbium, Tullium and other rare earth metals. The model that best described the modulations and which sparked theoretical interest in this class of phenomena was originally proposed by Elliot[9] and later renamed Anisotropic (or Axial) Next Nearest Neighbour Ising (ANNNI) model, an Ising model on a cubic lattice with a nearest neighbour ferromagnetic coupling on two coordinate axes and two competing nearest and next nearest couplings on the third axis. The ferromagnetic coupling, forces sites lying on parallel planes to have a unique orientation of the spins. The two out of plane couplings compete to the emergence of infinite modulated phases labelled by a wave vector. This infinity of

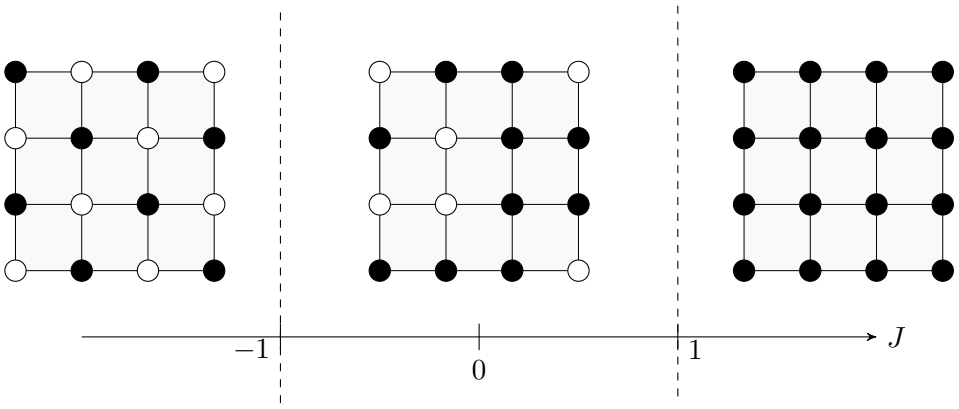

FIGURE 1.2: Phase diagram of the nearest neighbour Ising model on the square lattice.

phases goes under the suggestive name of *devil's staircase*, as originally named by Serge Aubry[31]. The ANNNI model phase diagram has been studied using several techniques ranging from various degrees of mean field theory and the soliton expansion (Bak and Van Boehm, 1980[4][5]) to the Monte Carlo simulation and low temperature expansion employed by Selke and Fisher [32][33]. A thorough review on the topic by Selke is the first chapter of [34]. While a review on the nature of phase transitions among phases with a wave vector compatible or incompatible with the underlying lattice (Commensurate-Incommensurate phase transition) was carried on by Janssen[35] and also studied by Mashiyama[36]. The most relevant feature of the ANNNI model is that the phases do not necessarily correspond to ground states. Other relevant or curious findings in the study of long range lattice systems are the work by Redner [37] on the one dimensional chain, where he points out an interesting connection with number theory; the appearance of the devil's staircase on the honeycomb lattice[38]; and the work by Grousson[39] on the phase diagram of the square lattice with Coulomb anti-ferromagnetic interactions. Finally, we mention two modern general techniques to tackle the ground states in this kind of systems: the first leverages on matrix product states, a method borrowed from quantum mechanics[40]; the second is a mapping to a maximum satisfiability problem[41] which we will use in the final part of the present work.

1.2 Previous Investigations

Our ultimate purpose is to study the range-3 Ising model, but the logical intermediate step is to consider Next Nearest Neighbours (NNN) interactions, which on the square lattice are the diagonal neighbours at Euclidean distance $\sqrt{2}$

$$H = -J_1 \sum_{\langle i,j \rangle} \sigma_i \sigma_j - J_2 \sum_{\langle\langle i,j \rangle\rangle} \sigma_i \sigma_j, \tag{1.2}$$

where the NNN interactions are represented by double angular brackets. In Fig.1.3a we show a 2×2 plaquette of this model, which also contains diagonal interactions. We emphasized a green triangle (out of the four possible), the two catheti are nearest neighbour interactions, while the hypotenuse is a next neighbour interaction. The

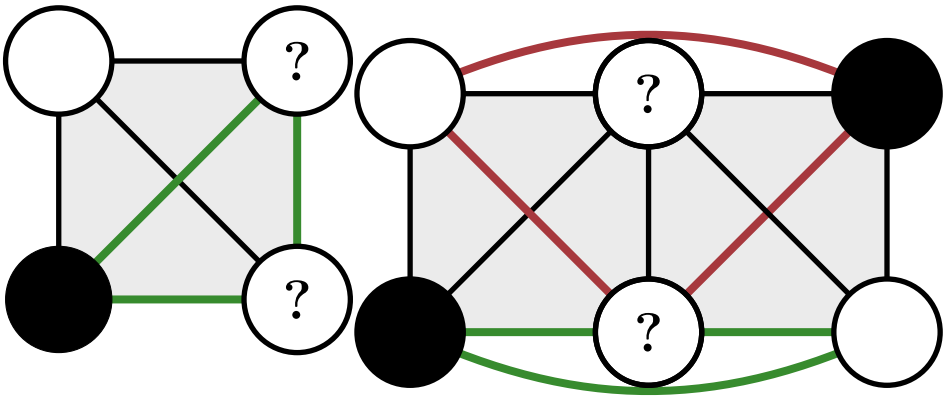

(A) Frustration on the range-2 Ising model. It creates one type of triangles.

(B) Frustration on the range-3 Ising model. It creates two additional types of triangles.

FIGURE 1.3: Frustration on the square lattice with two (left) and three (right) neighbours. Both lattices present frustration on the triangles.

competition happens at the level of triangles, a stable configuration depends on the sign of the two coupling parameters. When both J_1 and J_2 are negative we find a similar situation to the one described in Fig.1.1b. On each triangle the minimal energy configuration is degenerate with respect to single spin flips. Moreover, the system is complicated by a non trivial entanglement among all the triangles. The range 2 Ising model has been first studied by means of mean field theory, Renormalization Group Monte Carlo [42], and Cluster Variation Method[43]. A comprehensive review of these results and of the physics of this model through exact Monte Carlo has been studied by Landau and Binder[44] in 1980. Other than the ferromagnetic and anti-ferromagnetic phases, this model possesses a striped phase, as shown in the phase diagram of Fig.1.4a. The three ordered phases are separated by continuous phase transitions[45]. The striped phase arises for negative J_2 only and breaks the $\mathbb{Z}_4$ symmetry of the model[46] (only a subset of the whole point group symmetry). Changes in the intensity of the ferromagnetic next nearest neighbour coupling, J_2, only shift the critical temperature without introducing new orders.

Finally, we present the few attempts to tackle the range-3 model. The essential idea[48] is that the third range interaction affects the whole point symmetry group[12] $\mathfrak{D}_4$ of the square lattice. In Fig.1.3b we show the unit cell of the model. The range three interaction is parallel to the nearest neighbour interaction but double in distance, consequently the minimal subset considered is a 3×2 rectangle. In the figure, we emphasized how the introduction of a long range coupling introduces yet another level of frustration in the form of other two possible triangles (the smaller triangle present in the adjacent figure will of course still be present). One, shown in green, couples two range-1 interactions and one range-3 interaction, the other, shown in red, couples two range-2 interactions and one range-3 interaction.

The first attempts to study this model date back to the Eighties. These are sparse and not exhaustive, starting as spin-off studies from the rush toward the ANNNI model and long range lattice models in general. Kaburagi and Kanamori[49][50], in two successive papers from 1978 and 1983, focused on the ground states, employing their

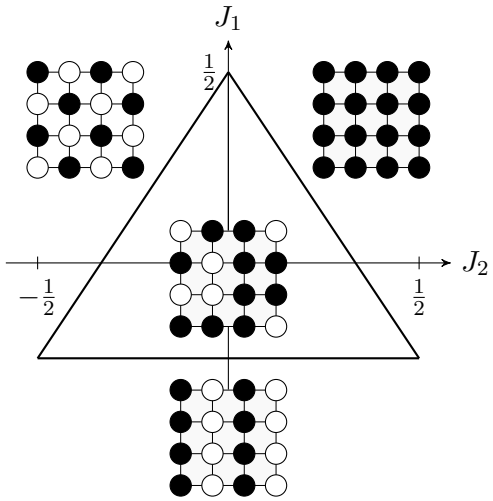

(A) Phase diagram of the range 2 Ising model. The new phase is the striped phase.

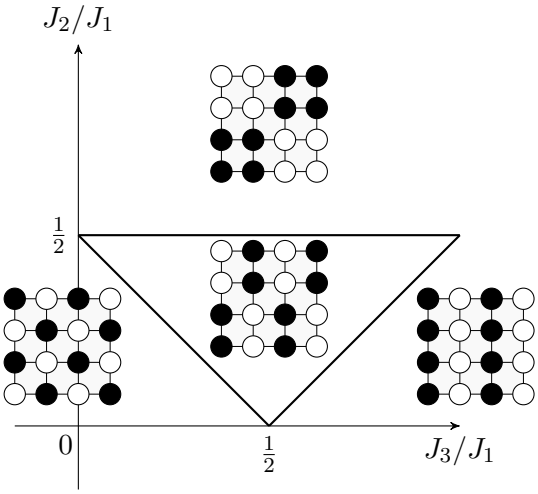

(B) Partial phase diagram of the range three Ising model, replicated from [47], for negative values of J_2 and J_3.

FIGURE 1.4: Phase diagrams.

cryptic method of inequalities[51], later refined by Teramoto and Itoh[52]. It consists in writing a set of inequalities, systematically including bigger and bigger clusters. The most exhaustive attempt using this method is due to Brandt and Liu[53] who, in 1983, claims to have found the exhaustive set of the ground state that amounts to 7 phases. However, these authors only calculated the inequalities up to clusters of the size of an interaction neighbours, while we suspect that longer-range patterns can be possibly stable.

The second important attempt is due to Landau and Binder, with the sole use of extensive Monte Carlo simulations. In Fig.1.4b we present their (incomplete) phase diagram. We recognize other 2 phases other then the striped phase. The upper one is known in the literature as double checkerboard, the central one as staggered dimer. In the same paper, Landau and Binder, characteristically state that *"[...] the phase diagram is expected to be very complicated ("devil's staircase" of phases) [...]"*. Without further investigating the model, they explicitly refer to the ANNNI model as a source for inspiration. In the same paper they also developed the Fourier space mean field theory, which we will use a starting point for our work. Moreover, we will use the given phase diagram as a reference point that we always wish to include and recover.

A final mention goes to a modern work by Kassan Ogly[54] that in 2015 studied the range-3 model separately setting the range-2 or the range-3 interaction to zero, by means of Monte Carlo replica method and the transfer matrix method, with a focus on the magnetization curves at the frustration points.

1.3 Research Question

A comprehensive study of the phase diagram of a range-3 Ising model on the square lattice has yet to be completed. As mentioned by Landau and Binder, we stress that is expected to be very complicated. In the present work we focus on the calculation of the paramagnetic region of stability, limiting ourselves to understand the parameter domain on whose boundary the first phase transitions occur, i.e. the determination of the order-disorder surface. The physics beyond this point is out of the scope of the present project and will be empirically addressed only in the chapter on the simulations.

1.4 Overview

We begin the present work by briefly introducing in Ch.2 the model, its symmetries and define the tools to tackle the phases: the periodic patterns and the order parameter. The take-home message is that a phase is a vector in the First Brillouin Zone of the lattice.

In the third chapter, Ch.3, we introduce the first novelty that we propose: a deconstruction of the Brillouin Zones. First, we introduce an enumeration of the periodic phases that allows to account for more and more complex patterns. Enforcing $N \times N$ periodic boundary conditions on the square lattice, reduces the possibly infinite modulated phases to the finite subset of periodic patterns whose period is commensurate with the size of the lattice. Next, we recover a bijection between the phases and the periodic patterns accounting for the point group symmetry of the square lattice. This is crucial simplification that will allow to understand the structure and the location of the various phases.

The formal core of the theory is in Ch.4. Following traditional arguments, we show how a simple mean field theory naturally leads to an infinite set of self-consistency equations, whose periodic solutions are the modulated phases of interest. Each solution uniquely defines a half-space containing the origin in parameter space, a bifurcation surface to the underlying periodic pattern. Leveraging on the structure of the Discrete Brillouin Zones previously introduced, we can take the intersection of all this planes that defines the paramagnetic region of stability as a convex polyhedron, a complex object whose study is the aim of the present thesis.

The structure of the polyhedra is studied in Ch.5. Systematically increasing the size of the lattices in periodic boundary conditions, we discuss how the structure of the polyhedra is related to the geometry of the Discrete Brillouin Zone and how these converge to similar shapes for large N. This is a non-trivial task and we have to rely on sophisticated numerical and analytical tools. For finite N the conversion of the half-space representation of the polyhedra to a vertex representation is known as vertex enumeration problem. We rely on the technique due to Avis and Fukuda[55][56][57], who, in 2006, propose an algorithm polynomial both in memory and time. Finally, to study the surface in the thermodynamic limit, we use a convex body reconstruction borrowed from elementary differential geometry.

To test the accuracy of the mean field approximation employed, in Ch.6, we present the result of Monte Carlo simulations. Our major goal is to inspect whether

periodic boundary conditions effectively forces periodic pattern to emerge in the coupling space radial direction (the centroid of the polyhedra faces) predicted by our theory. The minor aim is two empirically search for the phenomenology beyond the (first) bifurcation surfaces which we will address in terms of subsequent phase transitions and mode coexistence.

Lastly, in Ch.7 we pave the way to a quantitative analysis of the phenomenology observed in the simulations. To study the ground states of the system, we employ a modern technique[58], which consists in mapping the energy minimization problem to a maximum satisfiability (MAX-SAT) problem. The MAX-SAT algorithm, with respect to traditional optimization algorithm, has the advantage to prove the globality of the solution found. To address mode coexistence, we outline the first steps toward a more general solution of the mean field self-consistency equation.

Chapter 2

Model

Without further hesitation, we present the field free Ising model on the square lattice including up to third nearest neighbour interactions. After briefly introducing the square lattice and the Hamiltonian, we focus on the symmetries of the model. The emerging order breaks the whole symmetry point group of the lattice. Its structure will play a prominent role in characterizing the phases and the geometry of the phase diagram.

2.1 Square Lattice and Hamiltonian

Consider the infinite square lattice

$$\mathrm{L} = \{\mathrm{z} = (\mathrm{z}_1, \mathrm{z}_2) | \mathrm{z}_1, \mathrm{z}_2 \in \mathbb{Z}\}, \tag{2.1}$$

equipped with the usual group structure and scalar product. Throughout this thesis we will conventionally refer to lattice sites (and their duals) with lower case roman characters and to sets of sites with capitalized roman letters. We will also make extensive use of the $N \times N$ square lattice in Periodic Boundary Conditions (PBC), which is defined as

$$\mathrm{L}_N = \{\mathrm{z} = (\mathrm{z}_1, \mathrm{z}_2) | \mathrm{z}_1, \mathrm{z}_2 \in \mathbb{Z}_N\}, \tag{2.2}$$

equipped with the group structure inherited by $\mathbb{Z}_N$ and where the scalar product is defined accordingly. As basis vectors for the lattice[1], we will use $\mathrm{e}_1 = (1,0)^T$ and $\mathrm{e}_2 = (0,1)^T$. At each site z there is a classical spin-$\frac{1}{2}$ variable $\sigma_\mathrm{z} \in \mathbb{Z}_2$ which we conventionally represent by $\{-1, +1\}$. We define the range in between two sites $r(\mathrm{z}, \mathrm{z}')$ as the index of the ordered euclidean distance in between two sites $d(\mathrm{z}, \mathrm{z}') = ||\mathrm{z} - \mathrm{z}'||$. Given a site z, its neighbours at ranges $r(\mathrm{z}, \mathrm{z}') = 1$, $r(\mathrm{z}, \mathrm{z}') = 2$ and $r(\mathrm{z}, \mathrm{z}') = 3$ are respectively found at Euclidean distances $d(\mathrm{z}, \mathrm{z}') = 1$, $d(\mathrm{z}, \mathrm{z}') = \sqrt{2}$ ans $d(\mathrm{z}, \mathrm{z}') = 2$.

With these definitions the Hamiltonian of interest takes the form

$$H = -J_1 \sum_{r(\mathrm{z},\mathrm{z}')=1} \sigma_\mathrm{z}\sigma_{\mathrm{z}'} - J_2 \sum_{r(\mathrm{z},\mathrm{z}')=2} \sigma_\mathrm{z}\sigma_{\mathrm{z}'} - J_3 \sum_{r(\mathrm{z},\mathrm{z}')=3} \sigma_\mathrm{z}\sigma_{\mathrm{z}'}, \tag{2.3}$$

[1] If not differently specified, when we will refer to a lattice, we will equivalently imply either the infinite square lattice L or the square lattice in PBC L_N.

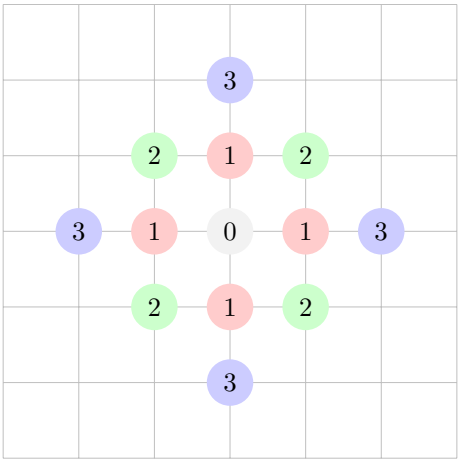

FIGURE 2.1: Distance neighbourhoods with respect to a general site z as defined in Eq.2.4. In red the first range neighbours, in green the second range neighbours and in blue the third range neighbours.

where J_1, J_2 and J_3 are the intensity of the couplings in between the three respective distance ranges. The minus follows the convention introduced in Sec.1, so that alignment of spins is favoured for positive values of the coupling parameters. For further notational convenience, we introduce the three distance neighbourhoods, shown in Fig.2.1

$$\begin{aligned} \mathrm{N}_1 &= \{\mathrm{e}_1, -\mathrm{e}_1, \mathrm{e}_2, -\mathrm{e}_2\}, \\ \mathrm{N}_2 &= \{\mathrm{e}_1 + \mathrm{e}_2, -\mathrm{e}_1 - \mathrm{e}_2, \mathrm{e}_1 - \mathrm{e}_2, -\mathrm{e}_1 + \mathrm{e}_2\}, \\ \mathrm{N}_3 &= \{2\mathrm{e}_1, -2\mathrm{e}_1, 2\mathrm{e}_2, -2\mathrm{e}_2\}. \end{aligned} \tag{2.4}$$

The neighbourhoods allows to emphasize the site energy contribution to the Hamiltonian

$$H(\sigma_{\mathrm{L}}) = \sum_{\mathrm{z}\in\mathrm{L}} \mathcal{E}(\sigma_{\mathrm{z}}), \tag{2.5}$$

where $\mathcal{E}(\sigma_{\mathrm{z}})$ is the energy contribution of a single spin

$$\mathcal{E}(\sigma_{\mathrm{z}}) = -\frac{1}{2}\sigma_{\mathrm{z}}\Big[J_1 \sum_{\mathrm{n}_1\in\mathrm{N}_1} \sigma_{\mathrm{z}+\mathrm{n}_1} + J_2 \sum_{\mathrm{n}_2\in\mathrm{N}_2} \sigma_{\mathrm{z}+\mathrm{n}_2} + J_3 \sum_{\mathrm{n}_3\in\mathrm{N}_3} \sigma_{\mathrm{z}+\mathrm{n}_3}\Big], \tag{2.6}$$

and the $\frac{1}{2}$ prefactor accounts for double counting of bonds.

2.2 Symmetries

The introduction of competing anti-ferromagnetic range-3 couplings does not only break the spin flip symmetry[2] of the Hamiltonian, it also affects the point group symmetry of the possible modulated spin configurations. This symmetry concurs in a non trivial way to phases of the model and is an essential feature to account for.

[2]The symmetry broken on the nearest neighbour Ising model on the square lattice is the simple $\mathbb{Z}_2$ symmetry.

The square lattice point group symmetry is the dihedral group of order four $\mathfrak{D}_4$. The usual two dimensional matrix representation consists of eight elements:, four rotations, among which we include the identity

$$e = \begin{pmatrix} 1 & 0 \\ 0 & 1 \end{pmatrix}, \quad r = \begin{pmatrix} 0 & 1 \\ -1 & 0 \end{pmatrix}, \quad r^2 = \begin{pmatrix} -1 & 0 \\ 0 & -1 \end{pmatrix}, \quad r^3 = \begin{pmatrix} 0 & -1 \\ 1 & 0 \end{pmatrix},$$

and four mirror symmetries, two with respect to the diagonals, two with respect to the vertical and horizontal axes

$$s = \begin{pmatrix} 1 & 0 \\ 0 & -1 \end{pmatrix}, \quad sr = \begin{pmatrix} 0 & 1 \\ 1 & 0 \end{pmatrix}, \quad sr^2 = \begin{pmatrix} -1 & 0 \\ 0 & 1 \end{pmatrix}, \quad sr^3 = \begin{pmatrix} 0 & -1 \\ -1 & 0 \end{pmatrix}.$$

The dihedral group has a major role in the understanding of the phases. However, the nature of symmetry breaking cannot be understood in terms of this group only as the translational and color symmetries should have a role. While this is out of the scope of the present work, it has to be kept in mind, as some sparse comments in this direction may be made.

2.3 Phases

Postponing the statistical characterization of the model to Ch.4, we will here present the key notion of periodic pattern, the ordered phases in this model, and the order parameter that allows to discriminate among the phases.

2.3.1 Periodic Patterns on $\mathbb{Z}^2$

The emerging order in the system can be studied through the single site spin probabilities $\mathrm{P_z}(\sigma_\mathrm{z})$. For the moment it suffices to note that it defines the site magnetization

$$m_\mathrm{z} \equiv \langle \sigma_\mathrm{z} \rangle = \sum_{\sigma_\mathrm{z} \in \{-1,+1\}} \sigma_\mathrm{z} \mathrm{P_z}(\sigma_\mathrm{z}), \tag{2.7}$$

where with the angular bracket we denote the ensemble average. The emerging modulated phases are characterized by periodic magnetization patterns defined by the average spin orientation at each site. A periodic magnetization pattern m_z on the infinite square lattice is (non uniquely) characterized by any two linearly independent non zero integer vectors p_1 and p_2 such that $m_\mathrm{z} = m_{\mathrm{z}+\mathrm{k}\cdot\mathrm{p}_1+\mathrm{k}\cdot\mathrm{p}_2}$ for all k and z in the lattice. For further convenience we collect the two vectors in a matrix

$$\mathrm{P} = \begin{pmatrix} \mathrm{p}_1^1 & \mathrm{p}_2^1 \\ \mathrm{p}_1^2 & \mathrm{p}_2^2 \end{pmatrix}, \tag{2.8}$$

which we will refer to as *periodicity*. The two vectors span a parallelogram whose area (number of lattice points) is given by the determinant of the periodicity $\det(\mathrm{P}) = \mathrm{p}_1^1\mathrm{p}_2^2 - \mathrm{p}_2^1\mathrm{p}_1^2 \equiv N$, which we will refer to as *index* or *size* of the periodicity. Without loss of generality, we consider periodicities with positive entries only. As we show in

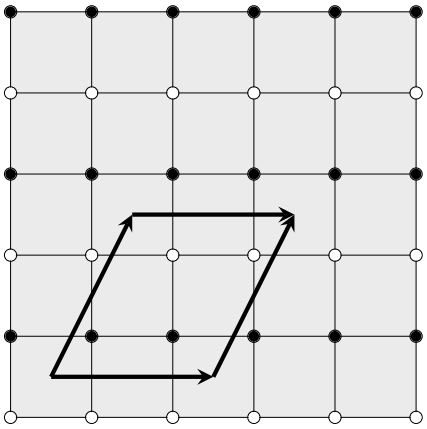

FIGURE 2.2: Unit cell of basis vectors $p_1 = (2, 0)$, $p_2 = (1, 2)$ with size $N = 4$. The underlying configuration is the compatible horixontal striped pattern.

Fig.2.2, this allows to uniquely introduce a unit cell $\mathcal{U}_{\mathrm{P}}$, as the set of all elements of $\mathbb{Z}^2$ compatible with the periodicity P

$$\mathcal{U}_{\mathrm{P}} = \left\{ \mathrm{z} \in \mathbb{Z}^2 \,\middle|\, \begin{array}{l} 0 \leq \langle \mathrm{z}, \mathrm{p}_1 \rangle \langle \mathrm{p}_2, \mathrm{p}_2 \rangle - \langle \mathrm{z}, \mathrm{p}_2 \rangle \langle \mathrm{p}_1, \mathrm{p}_2 \rangle < N^2 \\ 0 \leq \langle \mathrm{z}, \mathrm{p}_2 \rangle \langle \mathrm{p}_1, \mathrm{p}_1 \rangle - \langle \mathrm{z}, \mathrm{p}_1 \rangle \langle \mathrm{p}_1, \mathrm{p}_2 \rangle < N^2 \end{array} \right\}. \tag{2.9}$$

Given a unit cell, its dual is defined as the row vectors q which leave the Fourier transform invariant under integer translations, i.e. those vectors that for all integers $l = (l_1, l_2) \in \mathbb{Z}^2$ satisfy

$$\exp(i\langle \mathrm{q}, \mathrm{z} \rangle) = \exp(i\langle \mathrm{q}, \mathrm{z} + \mathrm{P} \cdot l \rangle), \tag{2.10}$$

or equivalently the solutions of

$$\mathrm{q} = 2\pi \mathrm{P}^{-1} \mathrm{k}, \tag{2.11}$$

which are by definition translationally invariant. The canonical basis in the dual space is given by $\hat{\mathrm{p}}_1$ and $\hat{\mathrm{p}}_2$ defined as $\mathrm{P}^{-1} \cdot \hat{\mathrm{p}}_j = \mathrm{e}_j$. Using that $\det(\mathrm{P}^{-1}) = \det(\mathrm{P})$ we can define the dual unit cell

$$\widehat{\mathcal{U}}_{\mathrm{P}} = \left\{ \mathrm{q} = 2\pi \mathrm{P}^{-1} \mathrm{k} \,\middle|\, \mathrm{k} \in \mathbb{Z}^2, \; \begin{array}{l} 0 \leq \langle \mathrm{k}, \hat{\mathrm{p}}_1 \rangle \langle \hat{\mathrm{p}}_2, \hat{\mathrm{p}}_2 \rangle - \langle \mathrm{k}, \hat{\mathrm{p}}_2 \rangle \langle \hat{\mathrm{p}}_1, \hat{\mathrm{p}}_2 \rangle < N^2 \\ 0 \leq \langle \mathrm{k}, \hat{\mathrm{p}}_2 \rangle \langle \hat{\mathrm{p}}_1, \hat{\mathrm{p}}_1 \rangle - \langle \mathrm{k}, \hat{\mathrm{p}}_1 \rangle \langle \hat{\mathrm{p}}_1, \hat{\mathrm{p}}_2 \rangle < N^2 \end{array} \right\}, \tag{2.12}$$

which shows that a unit cell defined by a periodicity with index N is compatible with exactly $|\widehat{\mathcal{U}}_{\mathrm{P}}| = N$ periodic patterns. We notice that $\widehat{\mathcal{U}}_{\mathrm{P}} \subset \widehat{\mathcal{U}}_{\infty}$, the Brillouin Zone of the lattice. Thus each phase is an element of the Brillouin zone, amounting to infinite possible modulations. We will get back to this in Ch.3.

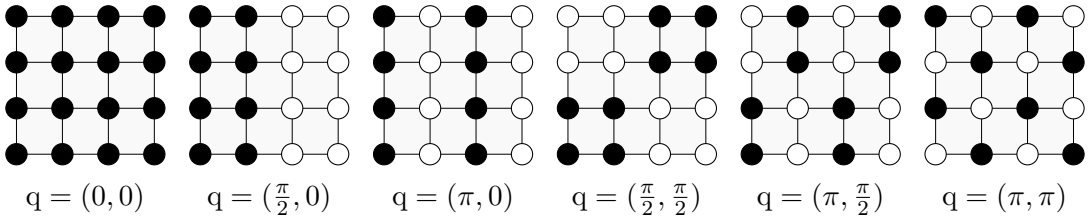

FIGURE 2.3: Phases on the square lattice and their corresponding wave vector.

2.3.2 Order Parameter

A natural way to tell phases apart are the coefficients m_{q} of the Fourier expansion of the site magnetization

$$m_{\mathrm{z}} = \sum_{\mathrm{q} \in \widehat{\mathcal{U}}_{\mathrm{P}}} m_{\mathrm{q}} e^{i\langle \mathrm{q},\mathrm{z}\rangle}. \tag{2.13}$$

A unique periodic magnetization pattern is then recognized by the dominant component, i.e. the anti-Fourier transform

$$m_{\mathrm{q}} = \frac{1}{N} \sum_{\mathrm{z} \in \mathcal{U}_{\mathrm{P}}} m_{\mathrm{z}} e^{-i\langle \mathrm{q},\mathrm{z}\rangle}, \tag{2.14}$$

it is however worth to be remarked that there might be higher harmonics contributing to the phase, thus contributing to the symmetry breaking. In this formalism the ferromagnetic phase has an infinite period over the two axes, with a corresponding wave vector $\mathrm{q} = (0, 0)$, accordingly Eq.2.14 reduces to the arithmetic mean over site magnetizations, the nearest neighbour ferromagnetic Ising order parameter. The Neel ordered phase, is the phase with the shortest possible period on both axes and is labelled by the mode $\mathrm{q} = (\pi, \pi)$. Also in this case, Eq.2.14 effectively reduces to the staggered magnetization, the order parameter for the anti-ferromagnetic Ising model on the square lattice. The striped phase is a mixture of the two, with a wave vector that can be equivalently expressed as $\mathrm{q} = (0, \pi)$ or $\mathrm{q} = (\pi, 0)$. In Fig.2.3 we show these and other phases, as previously found by Landau and Binder[59]. The crucial issue (which we will discuss in depth in the next chapter) is that while the patterns are effectively labeled by vectors in the Brillouin Zone, multiple patterns may give the same physics, the most simple example being the two possible orientations of the striped phase. To this end we want to make the anti-Fourier transform of Eq.2.14 both translational and dihedral invariant, such that it can serve as an order parameter.

The Fourier coefficients are complex numbers, their square norm $|m_{\mathrm{q}}|^2$ is maximal when the wave expansion matches the real space pattern. The phase of m_{q} does not provide any useful additional information: a phase shift e^{u} is equivalent to a translation T_{u} of the pattern

$$T_{\mathrm{u}} m_{\mathrm{q}} = \frac{1}{N} \sum_{\mathrm{n} \in \mathcal{U}_{\mathrm{P}}} m_{\mathrm{n}+\mathrm{u}} e^{-i\mathrm{q}\cdot\mathrm{n}} = \frac{1}{N} \sum_{\mathrm{n}' \in \mathcal{U}_{\mathrm{P}}} m_{\mathrm{n}'} e^{-i\mathrm{q}\cdot(\mathrm{n}'-\mathrm{u})} = e^{i\mathrm{q}\cdot\mathrm{u}} m_{\mathrm{q}}. \tag{2.15}$$

Thus, the square norm is translation invariant and a better tool to describe the underlying pattern. Nonetheless, different values of $|m_{\mathrm{q}}|^2 = m_{\mathrm{q}}^* m_{\mathrm{q}}$ might underpin the same phase. The simplest example being the striped phase: $|m_{(0,\pi)}|^2$ is maximal on the pattern $\mathrm{q} = (0, \pi)$ but minimal on $\mathrm{q} = (\pi, 0)$ and viceversa. We thus need to account for rotations or reflections of the pattern, i.e. the symmetry point group of the square lattice, introduced in Sec.2.2. For all elements $g \in \mathfrak{D}_4$

$$g m_{\mathrm{q}} = \frac{1}{N} \sum_{\mathrm{n} \in \mathcal{U}_{\mathrm{P}}} m_{g\mathrm{n}} e^{-i\mathrm{q}\cdot\mathrm{n}} = \frac{1}{N} \sum_{\mathrm{n}' \in \mathcal{U}_{\mathrm{P}}} m_{\mathrm{n}'} e^{-i\mathrm{q}\cdot g^{-1}\mathrm{n}'} = \frac{1}{N} \sum_{\mathrm{n}' \in \mathcal{U}_{\mathrm{P}}} m_{\mathrm{n}'} e^{-ig\mathrm{q}\cdot\mathrm{n}'} = m_{g\mathrm{q}}. \tag{2.16}$$

Consequently, we can simply take the average over the action of group elements

$$\mu_{\mathrm{q}} \equiv \frac{1}{|\mathfrak{D}_4|} \sum_{g \in \mathfrak{D}_4} m_{g\mathrm{q}}^* m_{g\mathrm{q}}, \tag{2.17}$$

which is invariant under both the translational and dihedral symmetries of the lattice and can be effectively used as an order parameter.

Chapter 3

Discrete Brillouin Zone

In the previous chapter we introduced ordered phases on the range-3 Ising model as periodic magnetization patterns. Each pattern is uniquely identified by a vector q of the dual lattice. Before delving into the statistical mechanics of the model, it is of great importance to understand the geometrical structure of the dual lattices. The dual lattice of the infinite square lattice is well known to be the first Brillouin Zone (BZ), the set of dual vectors $U_\infty \equiv \mathrm{q} \in [0, 2\pi) \times [0, 2\pi)$ satisfying

$$e^{i\mathrm{q}\cdot\mathrm{z}} = 1. \tag{3.1}$$

The dual lattice of L_N is less known. Constraining the square lattice with Periodic Boundary Conditions also constrains the BZ to a subset of the infinite possible periodic patterns. We will refer to the dual of the lattice L_N as *Discrete Brillouin Zone* which strictly depends on the divisors of the size N itself. Intuitively, the period of a magnetization pattern has to be commensurate with the size of the unit cell considered. To this end, we will here investigate the geometrical structure of the Discrete Brillouin Zone varying the size N of the underlying lattice. We begin constructing it from the definition of periodic pattern given in the previous chapter and provide an interesting connection to number theory which directly reflects on the geometrical structure of the paramagnetic region of stability. Ultimately, we consider once again the point group symmetry of the lattice, which yields a one to one relation in between phases and periodic patterns. Nonetheless, we remind that not all patterns might emerge as a phase, this concept will be clarified in Ch.5.

3.1 Discrete Brillouin Zone

We will now constructively show that the Brillouin zone of the square lattice in Periodic Boundary Conditions with size N is

$$\widehat{\mathcal{U}}_N \equiv \bigcup_{\{\mathrm{P}|\,\det(\mathrm{P})=N\}} \widehat{\mathcal{U}}_{\mathrm{P}}, \tag{3.2}$$

where $\widehat{\mathcal{U}}_{\mathrm{P}}$ is defined in Eq.2.12. The intuition behind our proof is that the size N of the lattice needs to be a multiple of the index of a periodicity for this to be compatible with the lattice.

The first step is to classify the set of periodicities with index N, a problem equivalent to the enumeration of subgroups of $\mathbb{Z}^2$ with index N. This is performed

leveraging on a classic theorem due to Hermite[60] from 1851, which classifies integer matrices in equivalence classes, labelled by the divisors of the determinant. That is, for any matrix $\mathrm{P} \in GL_2(\mathbb{N})$, there exist a unimodular (determinant preserving up to sign) matrix $J \in GL_2(\mathbb{N})$ such that $\mathrm{P}^* = J \cdot \mathrm{P}$, with

$$\mathrm{P}^* = \begin{pmatrix} d & 0 \\ 0 \leq s < \mathrm{d} & N/d \end{pmatrix}, \tag{3.3}$$

where d is a divisor of N, which will be denoted with $d|N$ and s an integer. A straightforward consequence is that there exist exactly $\sum_{d|N} d$ inequivalent possible periodic patterns of size N, which can be easily enumerated.

As an example, the number of inequivalent periodicities of size $N = 4$ is $\sum_{d|N} d = 4 + 2 + 1 = 7$. Explicitly, the periodicity matrices are:

$$\begin{pmatrix} 1 & 0 \\ 0 & 4 \end{pmatrix}, \quad \begin{pmatrix} 2 & 0 \\ 0 & 2 \end{pmatrix}, \quad \begin{pmatrix} 2 & 0 \\ 1 & 2 \end{pmatrix}, \quad \begin{pmatrix} 4 & 0 \\ 0 & 1 \end{pmatrix}, \quad \begin{pmatrix} 4 & 0 \\ 1 & 1 \end{pmatrix}, \quad \begin{pmatrix} 4 & 0 \\ 2 & 1 \end{pmatrix}, \quad \begin{pmatrix} 4 & 0 \\ 3 & 1 \end{pmatrix}.$$

In principle Hermite theorem already gives a route to the enumeration all the possible patterns compatible with the lattice L_N: after enumerating all the P matrices of a given index N, as we did in the example above, one can compute the respective unit cells $\widehat{\mathcal{U}}_{\mathrm{P}}$. This procedure leads to the exhaustive set of patterns. Nonetheless, the enumeration can be further simplified as we will now show.

The modes compatible with a unit cell P of index d are also compatible with the PBC square lattice L_N whether $d|N$. If $d > N$ clearly a pattern could not be "complete". While if $d < N$ but not commensurate with it, then periodic boundary conditions would prevent the pattern to appear. Thus, the set of all modes compatible with L_N is exhaustively given by all the modes that arise in all possible periodicities of size N. This idea is formalized in the following Lemma.

Lemma Discrete Brillouin Zone
The set of wave vectors of length compatible with a given size N is

$$\widehat{\mathcal{U}}_N = \{\mathrm{q} = \frac{2\pi}{N}(l_1, l_2) \; s.t. \; l_1, l_2 \in \{0, \cdots, N-1\}\}, \tag{3.4}$$

moreover, its size is $|\widehat{\mathcal{U}}_N| = N^2$.

Proof. We introduce an auxiliary $N \times N$ periodicity Π with generators $\pi_1 = (0, N)$, $\pi_2 = (N, 0)$ and DBZ $\widehat{\mathcal{U}}_\Pi$. The proof is carried on within two steps. We separately prove that $\widehat{\mathcal{U}}_\Pi$ includes and is included by the set $\widehat{\mathcal{U}}_N$, hence that the two coincide.

- $\widehat{\mathcal{U}}_N \subset \widehat{\mathcal{U}}_\Pi$
  Using Hermite theorem, any periodicity of size N is given by $\mathrm{p}_1 = (d, 0)^T$, $\mathrm{p}_2 = (s, N/d)^T$. So that the Π generators can be written as $\pi_1 = \frac{N}{d}\mathrm{p}_1$ and

$\pi_2 = -s\mathrm{p}_1 + d\mathrm{p}_2$. Thus any P periodic pattern of size N is also Π periodic

$$\widehat{\mathcal{U}}_N = \bigcup_{\{P|\det(\mathrm{P})=N\}} \widehat{\mathcal{U}}_{\mathrm{P}} \subset \widehat{\mathcal{U}}_{\Pi}. \tag{3.5}$$

- $\widehat{\mathcal{U}}_{\Pi} \subset \widehat{\mathcal{U}}_N$
  To prove the converse inclusion it suffices to show that for any $\mathrm{q} = \frac{2\pi}{N}(l_1, l_2) \in \widehat{\mathcal{U}}_{\Pi}$, there exists a periodicity P with size N such that $\mathrm{q} \in \widehat{\mathcal{U}}_{\mathrm{P}}$. The dual basis is defined by $\mathrm{P}^{-1} \cdot \hat{\mathrm{p}}_j = \mathrm{e}_j$. In Hermite normal form $\hat{\mathrm{p}}_1 = (d, s)$, $\hat{\mathrm{p}}_2 = (0, \frac{N}{d})$. Thus, any
  $$\mathrm{q} = 2\pi\left(\frac{l_1}{N}\hat{\mathrm{p}}_1 + \frac{l_2}{N}\hat{\mathrm{p}}_2\right) = 2\pi\left(\frac{l_1 d}{N}, \frac{l_1 s}{N} + \frac{l_2 N}{d}\right) \tag{3.6}$$
  belongs to a certain periodicity P with size N, if $d|N$ and it exists $0 \leq s < d$ such that the congruences
  $$l_1 d \equiv 0 \bmod N, \tag{3.7}$$
  $$l_1 s + l_2 \frac{N}{d} \equiv 0 \bmod N, \tag{3.8}$$
  hold. We can now take into account the two possible scenarios stemming from the above equations.
  - If $l_1 \nmid N$ the first relation is only solved by $d_1 = N$, hence the second one reduces to $l_1 s + l_2 \equiv \bmod N$. Next, we notice that the Great Common Denominator is $GCD(l_1, N) = 1$, thus by [61] a solution is always guaranteed.
  - If $l_1 \mid N$, then from the first equality $l_1 = \frac{N}{d}$ and the second one reduces to $\frac{N}{d}(s + l_2) = 0 \bmod N$ or equivalently $s + l_2 = 0 \bmod d$. This implies that l_2 is any multiple of d increased by a value $0 \leq \tilde{s} < d$, $l_2 = nd + \tilde{s}$. Finally, it exists a $0 \leq s < d$, $s = d - \tilde{s}$, which satisfies the second congruence relation.

  Thus, we have proved that $\widehat{\mathcal{U}}_{\Pi} \subset \widehat{\mathcal{U}}_N$.

Which finally implies

$$\widehat{\mathcal{U}}_{\Pi} = \widehat{\mathcal{U}}_N. \tag{3.9}$$

Furthermore, the size of the discrete Brillouin Zone is $|\widehat{\mathcal{U}}_N| = \det(\Pi) = N^2$.

□

The above lemma is crucial. We will make extensive use of it throughout the rest of the work. It directly provides an easy way to systematically enumerate all the periodic patterns compatible with a certain size N of the lattice L_N. Furthermore, it formalizes that a pattern may emerge on unit cells whether its period is commensurate with the size of the system. The first consequence is that the ferromagnetic phase, which is the only phase on the trivial 1×1 lattice, appears on any unit cell considered, as 1 trivially divides any possible index N. On a 2×2 lattice, we find only two possible patterns (other than the ferromagnetic pattern) labeled by the vectors $\mathrm{q} = (\pi, \pi)$ and $\mathrm{q} = (\pi, 0)$. The above lemma guarantees that these will be only shared by lattices with an even index.

As previously mentioned in Sec.2.3.2, the relation between patterns and phases is not bijective. Different patterns may correspond to the same phase, the simplest example is the striped phase that can have two possible orientations. This holds for more complex patterns and is the topic of the next section, where we recover a bijective relation accounting for the dihedral symmetry of the square lattice. Before, we provide a brief digression on a connection to elementary number theory, which further explores the relation with divisors and modes.

3.1.1 Complexity of a Pattern

As previously remarked, some patterns are compatible with different lattice sizes N. For example $\mathrm{q} = (0, 0)$ appears on any lattice of any size, while the mode $\mathrm{q} = (0, \pi)$ appears for even N only. As a direct consequence of Hermite theorem, two lattices share a periodic pattern if their sizes share a divisor, i.e. are commensurate. A mode q can always be expressed in the form

$$\mathrm{q} = 2\pi \left(\frac{j_1}{n_1}, \frac{j_2}{n_2} \right), \tag{3.10}$$

with j_i and n_i coprime natural integers. We define the *complexity* of a periodic pattern the minimum size for which it appears

$$C(\mathrm{q}) = \begin{cases} 0 & \mathrm{q}_1 = 0, \mathrm{q}_2 = 0 \\ n_1 & \mathrm{q}_1 \neq 0, \mathrm{q}_2 = 0 \\ n_2 & \mathrm{q}_1 = 0, \mathrm{q}_2 \neq 0 \\ \max(n_1, n_2) & \mathrm{q}_1 \neq 0, \mathrm{q}_2 \neq 0 \end{cases} . \tag{3.11}$$

To help the intuition, in Fig3.1 we show the dual lattice $\widehat{\mathcal{U}}_6$, colored according to the complexity of the modes. We say that a mode $\mathrm{q} \in \widehat{\mathcal{U}}_N$ is of full complexity if $C(\mathrm{q}) = N$. Introducing the Great Common Denominator (GCD) among three numbers, the set of modes with maximum complexity, for fixed size N, is

$$\widehat{\mathcal{U}}_N^{\dagger} \equiv \{\mathrm{q} = \frac{2\pi}{N}(l_1, l_2), (l_1, l_2) \in \mathbb{Z}_N^2 | \mathrm{GCD}(l_1, l_2, N) = 1\} = \widehat{\mathcal{U}}_N \setminus \bigcup_{n<N} \widehat{\mathcal{U}}_n, \tag{3.12}$$

i.e. the set of all periodicities q uniquely generated by cells of period N and its integer multiples. Which also allows to rewrite the Discrete Brillouin Zone as a disjoint union over these sets

$$\widehat{\mathcal{U}}_N = \bigcup_{d|N} \widehat{\mathcal{U}}_d^{\dagger}. \tag{3.13}$$

The set $\widehat{\mathcal{U}}_N^{\dagger}$is known[62](Theorem 7) to be a representation of the cyclic subgroups of $\mathbb{Z}_N^2$ of order 2. This identification gives the advantage to use known literature. Given two integers N and k, *Jordan totient functions*[1] $J_k(N)$ quantifies the number of k-tuples of integers less or equal than N that form a coprime $(k+1)$-tuple together with N. We will only be interested in studying the case $k = 2$.

[1]The Jordan totient is the series Empirically it has been verified up to $N = 50$ that the number of new periodicities added by each N and generated by constructing the P matrices coincides with the sequence given in http://oeis.org/A007434.

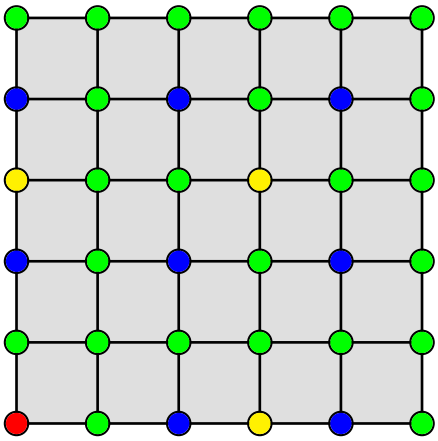

FIGURE 3.1: Dual lattice $\widehat{\mathcal{U}}_6$. each mode is colored according to its complexity C(q. The mode q $= (0, 0)$ (in red) is the only one with a complexity of 1; there are three modes (in yellow) with a complexity 2; eight modes (in blue) with a complexity 3 and twentyfour modes (in green) with a complexity of 6.

Analytical expressions for Jordan totient functions can be proved[63] to be both:

$$J_2(N) = N^2 \prod_{d|N} (1 - \frac{1}{d^2}), \tag{3.14}$$

and

$$J_2(N) = \sum_{d|N} \mu(d)(\frac{N}{d})^2 = \sum_{d|N} \mu(\frac{N}{d})d^2, \tag{3.15}$$

where $\mu(d)$ is the arithmetic function known as *Möbius inversion* which formalizes the inclusion-exclusion principle: we want to subtract from the total number of modes N^2 those which may appear among their divisors, however, some of them may share a divisor and we want to subtract it only once.

As a proof of principle, the Möbius inversion in the analytical expression of Eq.3.15, can be inverted yielding the so called Gaussian Decomposition[64] which retrieves the size of the set $\widehat{\mathcal{U}}_\mathrm{N}$

$$|\widehat{\mathcal{U}}_\mathrm{N}| = \sum_{d|N} J_2(d) = N^2, \tag{3.16}$$

decomposed on its divisors.

The example in Fig.3.1 should now be clearly interpretable: we show the decomposition for $N = 6$, the total amount of modes is 36, we have to subtract the total amount of its divisors 3^2, 2^2 and 1^2. However the divisor 1, other than itself, is shared by both 3 and 2, so that we want to subtract it only once. Explicitly

$$|\widehat{\mathcal{U}}_6^\dagger| = J_2(6) = \sum_{d|6} \mu(\frac{6}{d})d^2 = 36 - (9 - 1) - (4 - 1) - 1 = 24. \tag{3.17}$$

3.2 Symmetry Reduced Brillouin Zones

So far we showed that the exhaustive set of patterns that may emerge on the lattices L_N and L are respectively the Discrete Brillouin Zone $\widehat{\mathcal{U}}_N$ and the infinite Brillouin Zone $\widehat{\mathcal{U}}_\infty$. Furthermore, we characterized the former in terms of its divisors. Nonetheless, as we already pointed out, the underlying physics should be invariant under rotations or reflections of a pattern, i.e. under the action of elements $g \in \mathfrak{D}_4$. The one to one correspondence of orbits and inequalities does not only give a tighter upper bound on the number of phases compatible with L_N, it allows to introduce beforehand key notions that will be of use in Ch.5.

Formally, we define the *Symmetry Reduced Brillouin Zone* (SBRZ) as the quotient set[2] of the Discrete Brillouin Zone with respect to the action of $\mathfrak{D}_4$

$$\widehat{\mathfrak{U}}_N \equiv \mathbb{Z}_N^2/\mathfrak{D}_4 = \{\mathfrak{D}_4 \mathrm{q} \mid \mathrm{q} \in \widehat{\mathcal{U}}_N\}, \tag{3.18}$$

where in the following we will use the $\mathfrak{fraktur}$ font to refer to quantities related to SRBZ.

To further investigate the partition of the set $\widehat{\mathcal{U}}_N$ under the action of the dihedral group $\mathfrak{D}_4$ we need to remember the fundamental theory of group actions[3]:

Theorem Let G be a finite group acting on a set X. If X is finite then there exist disjoint orbits $O_{x_1}, ..., O_{x_k}$ such that $|X| = |O_{x1}| + ... + |O_{xk}|$. Furthermore, the size of an orbit is such that divides the size of G, $|O_i| \,|G|$.

The group $\mathfrak{D}_4$ has size 8 and consequently admits 4 different orbit sizes. In Fig. 3.2 we show the Brillouin Zone $\widehat{\mathcal{U}}_\infty$ and 4 modes, each representing one of the 4 possible orbit sizes. For each of the 4 modes we show the other equivalent elements under the action of $\mathfrak{D}_4$. [These are color coded to stress how the orbit size depends on the position on $\widehat{\mathcal{U}}_\infty$.] The orbit size of a mode strictly depend on the position on $\widehat{\mathcal{U}}_\infty$. The mode $\mathrm{q} = (0, 0)$ and $\mathrm{q} = (\pi, \pi)$ are the only one with an orbit size of 1. Intuitively, the action of $\mathfrak{D}_4$ on a mode is a reflection or a rotation with respect to the "center" $\mathrm{q} = (\pi, \pi)$, and from this we can infer the size. Without surprise, the only mode with an orbit size of 2 is $\mathrm{q} = (0, \pi)$, the striped pattern. While, with an orbit size of 4 we find all the modes that lie either on a diagonal, vertical or horizontal symmetry axes or on the border of $\widehat{\mathcal{U}}_\infty$. All the other modes have an orbit size of 8.

As representative for the whole equivalence class we will conventionally take the vectors in the lower left triangle, the shaded region of Fig.3.2

$$\widehat{\mathfrak{U}}_N = \{\mathfrak{q} = (\mathfrak{q}_1, \mathfrak{q}_2) \mid \mathfrak{q}_1 > \mathfrak{q}_2, \mathfrak{q}_1, \mathfrak{q}_2 \leq \pi\}, \tag{3.19}$$

it is enclosed by the vertices $\mathfrak{q} = (0, 0)$, $\mathfrak{q} = (0, \pi)$, $\mathfrak{q} = (\pi, \pi)$, the only three modes with an orbit size of 1 or 2. Its three borders are parametrized by $\mathfrak{q} = (0, \alpha)$, $\mathfrak{q} = (\alpha, \pi)$ and $\mathfrak{q} = (\alpha, \alpha)$ with $\alpha \in [0, \pi]$.

[2] This definition matches the definition of orbifold given by John Conway[65], which might be of use to generalize the present work to more complicated lattice geometries.

[3] The fundamental theorem of group actions consists on a multiple characterization of the set of orbits. Here we will only state those of interest for our purposes.

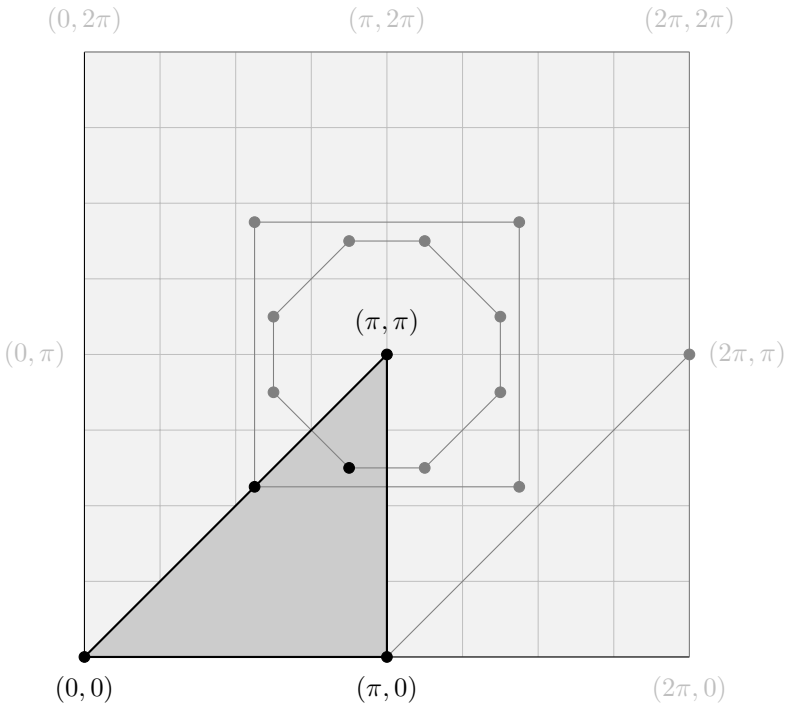

FIGURE 3.2: Graphical representation of the set $\widehat{\mathcal{U}}_\infty$ (light grey), overlapped by the set $\widehat{\mathfrak{U}}_\infty$ (heavier grey). For each of the four possible orbit sizes we show an element with its orbit. The modes $\mathfrak{q} = (0, 0)$ and $\mathfrak{q} = (\pi, \pi)$, with orbit size 1 stand in the center and in the bottom left corner. The mode $\mathfrak{q} = (\pi, 0)$, with an orbit size of 2 has only one equivalent pattern. The mode lying on the hypotenuse has four equivalent patterns represented by the four corners of the opaque square. Finally, the mode lying in the bulk of the triangle has an orbit size of 8 and is equivalent to each of the eight vertex of the octagon.

Also the number of modes in the SRBZ can simply be enumerated, as shown in the following lemma.

Lemma Symmetry Reduced Brillouin Zone
The Symmetry Reduced Brillouin Zone has size

$$|\widehat{\mathfrak{U}}_N| = \frac{1}{2}\left\lfloor \frac{N+2}{2} \right\rfloor \left(\left\lfloor \frac{N+2}{2} \right\rfloor + 1\right). \tag{3.20}$$

Proof. By the fundamental theorem of group actions, the Discrete Brillouin Zone $\widehat{\mathcal{U}}_{\mathrm{N}}$ can be disjointly decomposed as the union of its orbits. As a straightforward consequence also the size is decomposed

$$|\widehat{\mathcal{U}}_{\mathrm{N}}| = 1|O_1(N)| + 2|O_2(N)| + 4|O_4(N)| + 8|O_8(N)| \tag{3.21}$$

where $O_j(N)$ is the set of elements whose orbit has size j. Thus, the number of elements in the Symmetry Reduced Brillouin Zones is given by

$$|\widehat{\mathfrak{U}}_{\mathrm{N}}| = |O_1(N)| + |O_2(N)| + |O_4(N)| + |O_8(N)|, \tag{3.22}$$

and the enumeration problem is reduced to separately count the elements in each orbit size. To this end, we suggest to take a look at Figs.3.3a and 3.3b, that showsa clear difference in between even and odd sizes N is needed: the right green column never appears for odd N.

There are two patterns of orbit size 1: $\mathfrak{q} = (0,0)$ is shared by both even and odd N, while $\mathfrak{q} = (\pi,\pi)$ only appears for even N. The same holds for the unique mode with an orbit size 2, $\mathfrak{q} = (\pi,0)$. The modes with an orbit size of 4 appear on the three sides of $\mathfrak{U}_\infty$. Also in this case, we need to make a distinction between even and odd sizes N. The number of modes on each side of the triangle is

$$N_s = \begin{cases} \frac{N-1}{2} & N \text{ odd} \\ \frac{N-2}{2} & N \text{ even} \end{cases}, \tag{3.23}$$

For even N there are three sides and $3N_s$ modes. For odd N, the sides are only two, for a total of $2N_s$ modes. Finally, the modes with an orbit size of 8 can be computed as

$$\sum_{n=1}^{N_s-1} n = \frac{1}{2}N_s(N_s+1), \tag{3.24}$$

both for even and odd N.

The above consideration yields the following brief summary

$$\begin{aligned} |O_1| &= \begin{cases} 1 & N \text{ odd} \\ 2 & N \text{ even} \end{cases}, & |O_2| &= \begin{cases} 0 & N \text{ odd} \\ 1 & N \text{ even} \end{cases}, \\ |O_4| &= \begin{cases} N-1 & N \text{ odd} \\ 3\frac{N-2}{2} & N \text{ even} \end{cases}, & |O_8| &= \begin{cases} \frac{1}{8}(N-1)(N-3) & N \text{ odd} \\ \frac{1}{8}(N-2)(N-4) & N \text{ even} \end{cases}. \end{aligned} \tag{3.25}$$

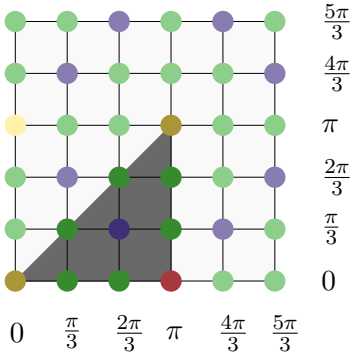

(A) DBZ $\widehat{\mathcal{U}}_6$ and SRBZ $\widehat{\mathfrak{U}}_6$ of the lattice L_6. The three edges of the SRBZ have an orbit size 4.

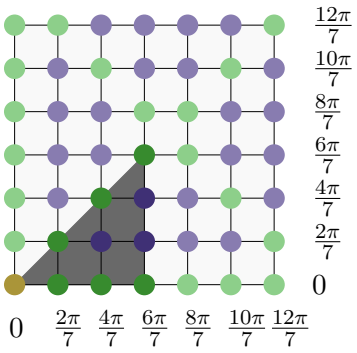

(B) DBZ $\widehat{\mathcal{U}}_7$ and SRBZ $\widehat{\mathfrak{U}}_7$ of the lattice L_6. Only the horizontal cathetus and the hypotenuse of the SRBZ have an orbit size 4. The vertical cathetus has an orbit size 8.

FIGURE 3.3: Comparison of the DBZ and the SRBZ of an even sized and an odd sized lattice. Both have the same number of modes, yet their orbit size is distribution is different.

Plugging the above decomposition in Eq.3.21, we recover, as a proof of principle, the size of $\widehat{\mathcal{U}}_N$

$$|\widehat{\mathcal{U}}_N| = \begin{cases} 11 + 4(N-1) + 8\frac{1}{8}(N-1)(N-3) & \text{odd } N \\ 12 + 21 + 4\,3\frac{N-2}{2} + 8\frac{1}{8}(N-2)(N-4) & \text{even } N \end{cases} = N^2. \tag{3.26}$$

Finally, inserting the orbit sizes in Eq.3.22, the total number of unique patterns (up to rotations and reflections) is given by:

$$|\widehat{\mathfrak{U}}_N| = \begin{cases} \frac{1}{8}(N+1)(N+3) & \text{odd}N \\ \frac{1}{8}(N+2)(N+4) & \text{even}N \end{cases}, \tag{3.27}$$

which can be compactly rewritten as:

$$|\widehat{\mathfrak{U}}_N| = \sum_{n=1}^{\lfloor \frac{N}{2}+1 \rfloor} n = \frac{1}{2}\left\lfloor \frac{N+2}{2} \right\rfloor \left(\left\lfloor \frac{N+2}{2} \right\rfloor + 1\right), \tag{3.28}$$

which proves the above claim. □

As a concrete example we compare the Symmetry Reduced Brillouin Zones $\widehat{\mathfrak{U}}_6$ and $\widehat{\mathfrak{U}}_7$ of the lattices L_6 and L_7 respectively, shown in Fig.3.3. The colors represent the orbit size, and will be used throughout the rest of the present work. Their importance should not be underestimated and will become clear in Ch.5. Yellow is used for the two modes with an orbit size of 1 and red for the unique mode with orbit size 2. The symmetry axes, as well as the lower and left borders are colored in green to signal an orbit size of 4, while all the others, with an orbit size of 8 are colored in blue. Using

the above lemma, clearly both $\widehat{\mathfrak{U}}_6$ and $\widehat{\mathfrak{U}}_7$ have a total of

$$\sum_{n=1}^{4} n = 10, \tag{3.29}$$

different modes. The main difference, and this is important, is the absence of the vertical and horizontal symmetry axes on $\widehat{\mathcal{U}}_7$. The consequence is that odd sizes will not be compatible with two out of the three corners of $\widehat{\mathfrak{U}}_\infty$.

3.2.1 Patterns and Phases

It has to be remarked that while we have enumerated all patterns, these do not necessarily all correspond to actual phases. Thus, Eq.3.28 is only an upper bound on the number of phases in the system. Some patterns will contribute in a pathological way, as will become clear in Sec.5.4.2. We anticipate here that these patterns are labelled by a q vector that lies on the anti-diagonal (using the proposed representation of Fig.3.2) going from $\mathfrak{q} = (0, \pi)$ to $\mathfrak{q} = (\frac{\pi}{2}, \frac{\pi}{2})$ and only appear for even N. Among the modes on the anti-diagonal, those who contribute with a phase are always the two extremes: the bottom right extreme is always $(0, \pi)$; the top left extreme is $(\pi/2, \pi/2)$ if N is a multiple of 4, and varies for all other N. Thus, Eq.3.28 gives the correct number of phases only for odd N. For N even we have to introduce a correction of $\lceil \frac{N}{4} \rceil - 1$. So that, the correct number of phases compatible compatible with the lattice L_N, is given for all N by

$$|\widehat{\mathfrak{U}}_N| = \frac{1}{2} \left\lfloor \frac{N+2}{2} \right\rfloor \left(\left\lfloor \frac{N+2}{2} \right\rfloor + 1 \right) - \frac{1 + (-1)^N}{2} \left(\left\lceil \frac{N}{4} \right\rceil - 1 \right). \tag{3.30}$$

3.3 Discussion

In this section we provided a formal way to enumerate all the patterns that may emerge on a lattice. We have further shown how, accounting for the symmetry point group of a lattice, gives a bijective relation between elements of the DBZ and phases compatible with the respective lattice. The notion of Symmetry Reduced Brillouin Zone and its triangular representation is essential to define the disorder region of stability of the model under investigation.

Chapter 4

Derivation of the Disordered Region

Under the assumptions of Mean Field Theory (MFT), the order-disorder region of transition takes the form of a polyhedron in parameter space, or for the infinite lattice, a convex body. Following traditional arguments, it is possible to minimize the free energy to find an infinite set of self-consistency equations for the magnetization patterns m_z. The solutions in Fourier space define planes parametrized by the coupling constants. Per each element in the Symmetry Reduced Brillouin Zone of the underlying lattice we find a unique plane, each representing the bifurcation surface to the phase defined by the corresponding pattern. The intersection of all planes yields the region of stability of the paramagnetic phase as a bounded polyhedron, the main object of investigation of the present work.

4.1 Mean Field Approximation

The whole of thermodynamics in a system at fixed temperature can in principle be calculated[1] under the fundamental assumption of statistical mechanics

$$P(\sigma_{\mathrm{L}}) = \frac{e^{-\beta H(\sigma_{\mathrm{L}})}}{Z}, \tag{4.1}$$

where the normalization $Z = \sum_{\sigma_{\mathrm{L}}} e^{-\beta H(\sigma_{\mathrm{L}})}$ takes the name of partition function and $\beta = \frac{1}{k_b T}$ is the inverse temperature, with k_b the Boltzmann constant that will be set to 1. The above probability can be formally obtained optimizing the entropy functional

$$S[P] = \sum P(\sigma_{\mathrm{L}}) \log P(\sigma_{\mathrm{L}}), \tag{4.2}$$

at fixed energy or equivalently the free energy functional

$$\Phi[P] \equiv \log Z = \beta \langle H \rangle - S[P], \tag{4.3}$$

[1] As any good book in statistical mechanics points out. For the present analysis we mostly referred to the books by Parisi[66], Huang[67] and Pathria[68].

where with square brackets we denote functionals and with angular brackets the average of an observable

$$\langle O \rangle \equiv \sum_{\sigma_{\mathrm{L}}} O(\sigma_{\mathrm{L}}) \mathrm{P}[\sigma_{\mathrm{L}}]. \tag{4.4}$$

Under these premises, the average value of any observable of interest can be computed as derivatives of the partition function alone.

Only few models have been exactly solved[69], as the exact partition function is often uncomputable and one has to rely on the approximation best suited to describe the phenomenon of interest. Different degrees of approximation retain different phenomena. The simplest approximation available takes the name of Mean Field Theory. Its origin can be traced back to a paper by Weiss[70] in 1907, and still remains an invaluable compromise in between usability and guidance to insights on the physics of toy models. Heuristically, it consists in considering the spins as independent, ignoring further correlations, such that the average spin orientation on the lattice acts as an effective external mean field. Mean field theory fails, or is less accurate, in the presence of high correlations, which appear both at criticality and in low dimensions. In one dimension it yields the wrong result of a finite temperature phase transition. While in 2 dimensions it correctly predicts a phase transition but at a rather wrong critical temperature[2].

Comparison with previous usage and results makes Mean Field Theory well suited for the present purpose: we are not interested in a quantitatively correct approach to study the physics at criticality, but rather at the emergence of phases triggered by the dihedral symmetry of the model, a universal feature retained by the mean field approximation. Nonetheless, the dimensionality of our model and the occurrence (as we will see) of subsequent phase transitions will require a thorough discussion on the validity of our results, which will be discussed[3] together with the numerical simulations in Ch.6.

Mathematically speaking, mean field theory relies on the assumption that the spin probabilities factorize

$$P_{MF}[\sigma_{\mathrm{L}}] = \prod_{\mathrm{z} \in \mathrm{L}} P(\sigma_{\mathrm{z}}). \tag{4.5}$$

The main implication, using the linearity of the average, is that spin correlations, and of any function g of the spins thereon, decomposes as

$$\langle g(\sigma_{\mathrm{z}}) g(\sigma_{\mathrm{z}'}) \rangle = \langle g(\sigma_{\mathrm{z}}) \rangle \langle g(\sigma_{\mathrm{z}'}) \rangle, \tag{4.6}$$

which stresses how Mean Field Theory systematically neglects all covariance in between variables.

[2] Charachteristically Onsager[22] solution shows a critical temperature of $T_c = \frac{2}{\log \sqrt{2}+1} \sim 2.269$, to be compared with the mean field prediction of $T_c^{MF} = 4$.

[3] In Ch.6 we confirm the existence of a transition systematically underestimating (as expected) the critical temperature. In the present chapter we will discuss the outcome without prejudice on its validity.

4.2 Self-Consistency Equations

The emerging modulated phases are charachterized by a magnetization pattern defined by the average spin orientation at each site

$$m_{\mathrm{z}} = \sum_{\sigma_{\mathrm{z}} \in \{-1,+1\}} \sigma_{\mathrm{z}} \mathrm{P}_{\mathrm{z}}(\sigma_{\mathrm{z}}). \tag{4.7}$$

Under the assumptions of Mean Field Theory the free energy functional of Eq.4.3, can be explicitely computed and minimized to yield an equation for the magnetization patterns. Using Eq.4.6 and the Hamiltonian of Eq.2.5, the average energy contribution to the free energy reads

$$\langle H \rangle_{MF} = \frac{1}{2} \sum_{\mathrm{z} \in \mathrm{L}} m_{\mathrm{z}} \left[J_1 \sum_{\mathrm{n}_1 \in \mathrm{N}_1} m\left(\mathrm{z}+\mathrm{n}_1\right) + J_2 \sum_{\mathrm{n}_2 \in \mathrm{N}_2} m\left(\mathrm{z}+\mathrm{n}_2\right) + J_3 \sum_{\mathrm{n}_3 \in \mathrm{N}_3} m\left(\mathrm{z}+\mathrm{n}_3\right) \right], \tag{4.8}$$

and the entropy

$$\begin{aligned} S[P_{MF}] = -\langle \log(P_{MF}[\sigma_{\mathrm{L}}]) \rangle = -\sum_{\mathrm{z} \in \mathrm{L}} \langle \log(P(\sigma_{\mathrm{z}})) \rangle = \\ = \sum_{\mathrm{z} \in \mathrm{L}} \frac{1+m_{\mathrm{z}}}{2} \log\left(\frac{1+m_{\mathrm{z}}}{2}\right) + \frac{1-m_{\mathrm{z}}}{2} \log\left(\frac{1-m_{\mathrm{z}}}{2}\right). \end{aligned} \tag{4.9}$$

Bringing the previous two equations together, the free energy reads

$$\begin{aligned} \Phi_{MF} = \beta \langle H \rangle_{MF} - S[P_{MF}] = \\ = \sum_{\mathrm{z} \in \mathrm{L}} \left[m_{\mathrm{z}} \left(\mathbf{K} \cdot \mathbf{M}(z, [m_{\mathrm{z}}]) \right) - \frac{1+m_{\mathrm{z}}}{2} \log\left(\frac{1+m_{\mathrm{z}}}{2}\right) + \frac{1-m_{\mathrm{z}}}{2} \log\left(\frac{1-m_{\mathrm{z}}}{2}\right) \right], \end{aligned} \tag{4.10}$$

where we have absorbed the inverse temperature in the coupling parameters

$$\mathbf{K} = (\beta J_1, \beta J_2, \beta J_3)^T \tag{4.11}$$

and introduced the shorthand notation for the neighbourhood magnetizations

$$\mathbf{M}(z, [m_{\mathrm{z}}]) = \left(\sum_{\mathrm{n}_1 \in \mathrm{N}_1} m_{\mathrm{z}+\mathrm{n}_1}, \sum_{\mathrm{n}_2 \in \mathrm{N}_2} m_{\mathrm{z}+\mathrm{n}_2}, \sum_{\mathrm{n}_3 \in \mathrm{N}_3} m_{\mathrm{z}+\mathrm{n}_3} \right)^T, \tag{4.12}$$

where the square bracket emphasize the functional dependence on the site magnetizations.

That is, the extreme point of the free energy $\frac{\partial \Phi}{\partial m_{\mathrm{z}}} = 0$ gives, through direct derivation

$$\begin{aligned} \mathbf{K} \cdot \mathbf{M}(z, [m_{\mathrm{z}}]) = \frac{1}{2} \log \frac{1+m_{\mathrm{z}}}{1-m_{\mathrm{z}}}, \\ m_{\mathrm{z}} = \tanh(\mathbf{K} \cdot \mathbf{M}(z, [m_{\mathrm{z}}])), \end{aligned} \tag{4.13}$$

an infinite set of self-consistency equations for the magnetizations whose solutions for fixed $\mathbf{K}$ are the phases of interest. Finally, we note that the solution $m_z = 0$ solves the above equation in all the parameter domain and for all values of β.

4.3 Bifurcation Surfaces

The three dimensional phase space of the model is spanned by the three $\mathbf{K}$ coordinates. Temperature is constant on spherical surfaces centered in the origin. The infinite temperature point is found in the origin, accordingly, the only solution of Eq.4.13 is the disordered phase, $m_z = 0$ for all z. The self-consistency equations define a surface in phase space where other solutions bifurcates from the disordered one. Moving away from the origin in any direction the site magnetization remains zero everywhere until it reaches a critical bifurcation surface, where the whole system undergoes a phase transition. The surfaces are explicitly found in two steps. First, Taylor expanding Eq.4.13 on the internal side of the surfaces

$$m_z = \mathbf{K} \cdot \mathbf{M}(z, [m_z]). \tag{4.14}$$

Then, restricting our attention to periodic solutions, taking the Fourier transform of the LHS and RHS of the above equation

$$\begin{aligned} m_z &= \sum_{q \in L} m_q e^{\langle q,z \rangle} \\ &= \sum_{q \in L} \left(K_1 \sum_{n \in N_1} m_q e^{\langle q,z+n \rangle} + K_2 \sum_{n \in N_2} m_q e^{\langle q,z+n \rangle} + K_3 \sum_{n \in N_3} m_q e^{\langle q,z+n \rangle} \right) \\ &= \sum_{q \in L} \left(K_1 \sum_{n \in N_1} e^{\langle q,n \rangle} + K_2 \sum_{n \in N_2} e^{\langle q,n \rangle} + K_3 \sum_{n \in N_3} e^{\langle q,n \rangle} \right) m_q e^{\langle q,z \rangle} \\ &= \sum_{q \in L} \mathbf{K} \cdot \mathbf{F}(q) m_q e^{\langle q,z \rangle}, \end{aligned} \tag{4.15}$$

where in the last step we factored out $e^{\langle q,z \rangle} = \cos(\langle q, n \rangle) + i \sin(\langle q, n \rangle)$, and grouped it in the vector

$$\mathbf{F}(q) = \begin{pmatrix} 2\cos(q_1) + 2\cos(q_2) \\ 2\cos(q_1 + q_2) + 2\cos(q_1 - q_2) \\ 2\cos(2q_1) + 2\cos(2q_2) \end{pmatrix}, \tag{4.16}$$

where we see that each neighbour contributes with a cosine term per each linear independent term and the imaginary part vanishes. A term by term comparison of the first and last line of Eq.4.15 yields

$$m_q = m_q \mathbf{K} \cdot \mathbf{F}(q). \tag{4.17}$$

The above equation defines the bifurcation surface of the solution m_q from the disorder solution. Explicitly

$$1 - K_1 F_1(q) - K_2 F_2(q) - K_3 F_3(q) = 0, \tag{4.18}$$

is the equation of a plane in $\mathbf{K}-$space, the coefficients only depends on Eq.4.16, the Fourier transform of the neighbourhoods, with respect to the bifurcating mode q.

It is meaningful to show how the same result can be obtained as the region of divergence of the spin-spin correlation function, or susceptibility. Mean Field Theory explicitly implies that the susceptibility decomposes as $\chi_{\mathrm{z,z'}} \equiv \langle \sigma_{\mathrm{z}} \sigma_{\mathrm{z'}} \rangle = \langle \sigma_{\mathrm{z}} \rangle \langle \sigma_{\mathrm{z'}} \rangle$, hence, in the disordered phase it is zero everywhere. We can work around this apparent contradiction using linear response theory: we let an arbitrary small and site dependent external field h_{z} act on the system, compute the response of the free energy and later set the external field to zero

$$\chi_{\mathrm{z,z'}} = \langle \sigma_{\mathrm{z}} \sigma_{\mathrm{z'}} \rangle = \frac{1}{\beta^2} \frac{\partial}{\partial h_{\mathrm{z}}} \frac{\partial}{\partial h_{\mathrm{z'}}} \Phi[h_{\mathrm{z}}] \mid_{h_{\mathrm{z}}=0} = \frac{\partial m_{\mathrm{z}}}{\partial h_{\mathrm{z'}}} \mid_{h_{\mathrm{z}}=0} . \tag{4.19}$$

The external, site dependent field, consists in an additional additive term in the Hamiltonian of Eq.2.3 that becomes

$$\beta H = -K_1 \sum_{r(\mathrm{z,z'})=1} \sigma_{\mathrm{z}} \sigma_{\mathrm{z'}} - K_2 \sum_{r(\mathrm{z,z'})=2} \sigma_{\mathrm{z}} \sigma_{\mathrm{z'}} - K_3 \sum_{r(\mathrm{z,z'})=3} \sigma_{\mathrm{z}} \sigma_{\mathrm{z'}} - \sum_{\mathrm{z} \in \mathrm{L}} \kappa_{\mathrm{z}}, \tag{4.20}$$

where, for notational convenience we defined $\kappa_{\mathrm{z}} = \beta h_{\mathrm{z}}$.

Thus, the susceptibility can be directly computed as a derivative of the magnetization. Repeating the calculation that lead to Eq.4.13 with the external field, simply introduces an additional term in the Mean Field self-consistency equations

$$m_{\mathrm{z}} = \tanh(\mathbf{K} \cdot \mathbf{M}(z, [m_{\mathrm{z}}]) + \sum_{\mathrm{z}} \kappa_{\mathrm{z}}). \tag{4.21}$$

Straightforward derivation yields

$$\begin{aligned} \chi_{\mathrm{z,z'}} =& \frac{1}{\cosh^2 \left(\mathbf{K} \cdot \mathbf{M}(z, [m_{\mathrm{z}}]) + \kappa_{\mathrm{z'}} \right)} \left(\delta_{\mathrm{z,z'}} + \mathbf{K} \cdot \frac{\partial \mathbf{M}(z, [m_{\mathrm{z}}])}{\partial \kappa_{\mathrm{z'}}} \right) \Big|_{h_{\mathrm{z'}}=0} \\ =& \frac{\delta_{\mathrm{z,z'}}}{\cosh^2 \left(\mathbf{K} \cdot \mathbf{M}(z, [m_{\mathrm{z}}]) \right)} \left(1 + \mathbf{K} \cdot \mathbf{X}(z, [m_{\mathrm{z}}]) \right) , \end{aligned} \tag{4.22}$$

where analogously as the magnetization vector, the susceptibility vector reads

$$\mathbf{X}(z, [m_{\mathrm{z}}]) = (\sum_{\mathrm{n} \in \mathrm{N}_1} \chi_{\mathrm{z+n}}, \sum_{\mathrm{n} \in \mathrm{N}_2} \chi_{\mathrm{z+n}}, \sum_{\mathrm{n} \in \mathrm{N}_3} \chi_{\mathrm{z+n}})^T. \tag{4.23}$$

Approaching the bifurcation surface from the disordered region, $T \to T_c$, we can Taylor expand the denominator

$$\chi_{\mathrm{z,z'}} = \delta_{\mathrm{z,z'}} (1 + \mathbf{K} \cdot \mathbf{X}(z, [m_{\mathrm{z}}])). \tag{4.24}$$

Finally, we drop the $\mathrm{z'}$ index and take the Fourier transform, mirroring the procedure that lead to Eq.4.17 above

$$\begin{aligned}\chi_{\mathrm{z}} &= \sum_{\mathrm{q}\in\mathrm{L}} \chi_{\mathrm{q}} e^{\langle \mathrm{q},\mathrm{z}\rangle} \\ &= \sum_{\mathrm{q}\in\mathrm{L}} \left(e^{\langle \mathrm{q},\mathrm{z}\rangle} + K_1 \sum_{\mathrm{n}\in\mathrm{N}_1} \chi_{\mathrm{q}} e^{\langle \mathrm{q},\mathrm{z}+\mathrm{n}\rangle} + K_2 \sum_{\mathrm{n}\in\mathrm{N}_2} \chi_{\mathrm{q}} e^{\langle \mathrm{q},\mathrm{z}+\mathrm{n}\rangle} + K_3 \sum_{\mathrm{n}\in\mathrm{N}_3} \chi_{\mathrm{q}} e^{\langle \mathrm{q},\mathrm{z}+\mathrm{n}\rangle} \right) \\ &= \sum_{\mathrm{q}\in\mathrm{L}} (1 + \chi_{\mathrm{q}} \mathbf{K}\cdot\mathbf{F}(\mathrm{q}) e^{\langle \mathrm{q},\mathrm{z}\rangle},\end{aligned} \tag{4.25}$$

where $\mathbf{F}(\mathrm{q})$ is the same defined in Eq.4.16. Comparing the Fourier transform coefficients and inverting

$$\chi_{\mathrm{q}} = \frac{1}{1 - \mathbf{K}\cdot\mathbf{F}(\mathrm{q})}, \tag{4.26}$$

which diverges at $1 - \mathbf{K}\cdot\mathbf{F}(\mathrm{q}) = 0$ and stresses the occurence of a phase transition at the critical plane.

That is, the region of stability of the paramagnetic phase with respect to a phase labelled by a pattern q is

$$H_{\mathrm{q}} \equiv \{\mathbf{K} | \mathbf{K}\cdot\mathbf{F}(\mathrm{q}) \leq 1\}, \tag{4.27}$$

a halfspace bounded by the bifurcation surface

$$L_{\mathrm{q}} \equiv \{\mathbf{K} | \mathbf{K}\cdot\mathbf{F}(\mathrm{q}) = 1\}. \tag{4.28}$$

The above definitions also stresses the role of $\mathbf{F}(\mathrm{q})$ as the vector orthogonal to L_{q}, that will become of fundamental importance in a later chapter. The region of stability with respect to all the dual vectors of the lattice L_N, i.e. the Symmetry Reduced Brillouin Zone $\widehat{\mathfrak{U}}_N$, defines the region of stability of the disordered phase

$$D_N = \bigcup_{\mathfrak{q}\in\widehat{\mathfrak{U}}_N} H_{\mathfrak{q}}, \tag{4.29}$$

a convex polyhedron containing the origin embedded in the space of coupling parameters. D_1 is basically a half-space, D_2 and D_3 are bounded by three planes only and are infinite polyhedra. While, we will see in Ch.5, that the more interesting polyhedra that arise for $N \geq 4$ are bounded, accordingly we will equivalently refer to them as *polytopes*[71]. Analogously, on the infinite square lattice, the envelope of all the planes in $\mathfrak{U}_\infty$ defines the convex body

$$D_\infty = \bigcup_{\mathfrak{q}\in\widehat{\mathfrak{U}}_\infty} H_{\mathfrak{q}}, \tag{4.30}$$

where, in agreement with the treatment of Ch.3, we reintroduced the fraktur notation for the equivalence class of modes.

The rest of the present work aims at studying the geometry of the polytopes varying the size N of the periodic patterns considered. We will investigate the relation of the geometry of the Symmetry Reduced Brillouin Zone and the polytopes D_N. For finite N we rely on the theory of convex polyhedra, their half-spaces and vertex

representations, and the conversion among the two. While for infinite N we will use a convex body reconstruction based on the vector $\mathbf{F}(\mathfrak{q})$.

Anticipating the results of the simulations, we mention that the region of stability of the paramagnetic phase defined above, as expected, overestimates the critical temperature but well retains the direction of each phase. Nonetheless, it overlooks and oversimplifies the physics beyond the bifurcation surfaces. It correctly predicts the dominant mode just right beyond the bifurcation surface, however it does not account neither for subsequent phase transitions, neither for secondary modes that could also be stable and concur with the dominant mode in the definition of a phase. We will hint at what could happen in the outlook.

Finally, a remark is in order. The definitions of Eqs.4.29 and 4.30 only depend on the Fourier transform of the neighbourhood indicator functions $\mathbf{F}(\mathrm{q})$. They are not at all limited to the range-3 Ising model on the square lattice but can be easily extended to any other lattice Hamiltonian with long range couplings. Where the dimensionality of the polytopes only depends on the range considered, the number of inequalities only depends on the size of the Symmetry Reduced Brillouin Zone and the orientation of the planes depends on the Fourier transform of the neighbourhood.

Chapter 5

The Disordered Region and its Boundaries

In the previous chapter, we derived the geometry of the disorder region of the lattice L_N as a bounded polytope

$$D_N = \bigcap_{\mathfrak{q}\in\mathfrak{U}_N} H_{\mathfrak{q}}, \qquad H_{\mathfrak{q}} = \mathbf{K}\cdot\mathbf{F}(\mathfrak{q}) \leq 1, \qquad \mathbf{F}(\mathfrak{q}) = \begin{pmatrix} 2\cos(\mathfrak{q}_1) + 2\cos(\mathfrak{q}_2) \\ 2\cos(\mathfrak{q}_1+\mathfrak{q}_2) + 2\cos(\mathfrak{q}_1-\mathfrak{q}_2) \\ 2\cos(2\mathfrak{q}_1) + 2\cos(2\mathfrak{q}_2) \end{pmatrix}. \quad (5.1)$$

The function $\mathbf{F}(\mathfrak{q})$ is the normal vector to the plane bounding the half space $H_{\mathfrak{q}}$, thereby, it encodes all the information on the geometry of D_N. We can thus regard the function $\mathbf{F}(\mathfrak{q})$ as a map from the Symmetry Reduced Brillouin Zone to the polytope itself. To infer the final shape of D_N, we will leverage on two different techniques: for finite N we rely on an numerical procedure to find the coordinate of the vertices of the polytopes; when N is infinite, we will use a convex body reconstruction. In the following, for the sake of notational simplicity, we directly refer to an inequality, or equivalently a face, with the coefficients $\mathbf{F}(\mathfrak{q})$. Moreover, we will abuse the vocabulary and use the words face, phase or mode interchangeably.

In order to abandon the abstract definition of polyhedron and start building a more concrete intuition, we suggest to examine Fig.5.1, where we show the polytopes from $N = 4$ (the lower N for which the polytope is bounded) up to $N = 18$. The color code of the faces is the same previously introduced and discriminates different orbit sizes. Whether two polytopes shares a set of faces depends on the shared divisors. In the first section of this chapter we address how the inclusion relations among SRBZ for different N, studied in Ch.3, reflect on the polytopes. Regardless the divisors, the larger N, the more the polyhedra converge to similar shapes. As a gentle introduction to the interpretation of the order-disorder diagram[1], we begin by describing D_4 in Sec.5.3. Next, in Sec.5.4, we phenomenologically compare D_8 and D_9, addressing the alternation of colors of the wider face, that clearly depends the parity of N. Even polytopes are more regular and in the rest of the chapter we will focus on them, with only sparse comments on odd polytopes. The position of a mode in $\widehat{\mathfrak{U}}_N$ depends on its orbit size. The corners have an orbit size of 1 or 2, the borders have an orbit size of 4 and the bulk has orbit size of 8. The most astonishing feature is the relation between

[1] We will show with simulations that subsequent phase transition occurs, so that the polyhedra are not phase diagrams.

the orbit size and the position of the faces[2]. To manifestly see this link we need to increase N up to 16. In Sec.5.5 we will show that the corners of $\widehat{\mathfrak{U}}_N$ always define the top of the polytopes. As it should already be clear, in the region $K_3 > 0$ each polytope is always bounded by three prominent modes only (the third one is always hidden from the proposed point of view). All the other faces appear for negative K_3. The modes on the border of $\widehat{\mathfrak{U}}_N$ create regular structures in the form of *fans*, as shown in Fig.5.1. These structures are the topic of Sec.5.6. The mapping of the bulk of the SRBZ is less simple to interpret and we will focus on a single characteristic of the distribution of the faces: they all cluster around a specific line. To fully understand the region of clustering, we will take a short digression, in Sec.5.7, to investigate the mathematical structure of $\mathbf{F}(\mathfrak{q})$ in terms of a natural coordinate frame that stresses that the domain of $\mathbf{F}(\mathfrak{q})$ is a two dimensional surface embedded in $\mathbb{R}^3$. This new frame of reference gives central importance to the empirical observations of the distribution of the faces, which we will describe in Sec.5.8. Furthermore, it provides a formal setting to represent the dual polyhedron, a graph retaining the adjacency relation of the polyhedron. The physical intuition is that the orientation of $\mathbf{F}(\mathfrak{q})$ depends on the underlying mode $\mathfrak{q}$, neighbouring modes on $\widehat{\mathfrak{U}}_N$ represent "similar" patterns. Thus, we physically expect that the bifurcation planes, with respect to neighbouring modes, to be only slightly tilted with respect to each other. Eventually, in Sec.5.9, we address the convex body reconstruction of D_∞, based on the value of $\mathbf{F}(\mathfrak{q})$ on any point in the SRBZ $\widehat{\mathfrak{U}}_\infty$.

5.1 Intersection Algebra and Carving of polyhedra

Before moving to the decription of the polytopes themselves, it is relevant to understand how the relations among Brillouin Zones $\widehat{\mathfrak{U}}_N$ manifest themselves on the polytopes D_N. The result presented in Sec.3.2, that for all $d|N$, $\widehat{\mathfrak{U}}_d \subset U_N$, together with the tautology $H_\mathfrak{q} \cap H_\mathfrak{q} = H_\mathfrak{q}$, implies that for all $d|N$, $D_d \supset D_N$. The mapping from $\widehat{\mathfrak{U}}_N$ to the polyhedra D_N, inverts the inclusion relation, or equivalently, the union of Brillouin Zones corresponds to the intersection of polyhedra

$$D_{\widehat{\mathfrak{U}}_N \cup \widehat{\mathfrak{U}}_M} = D_{\widehat{\mathfrak{U}}_N} \cap D_{\widehat{\mathfrak{U}}_M}. \tag{5.2}$$

To further stress that the faces of a polyhedron are completely characterized by the divisors of its index N, we will make use of the cyclic group decomposition introduced in Sec.3.1.1. Given a set of vectors of complexity $C(\mathrm{q})$ (see Sec.3.1.1) we define

$$D_C^\dagger \equiv \bigcap_{\mathfrak{q} \in U_C^\dagger} H_\mathfrak{q}. \tag{5.3}$$

It clearly is an unphysical object, but allows to emphasize the contribution to the polyhedron of all periodicities of size N. Using the disjoint decomposition of Eq.3.13 and the above definition, it follows

$$D_N = \bigcap_{\mathfrak{q} \in \widehat{\mathfrak{U}}_N} H_\mathfrak{q} = \bigcap_{d|N} \left(\bigcap_{\mathfrak{q} \in U_d^\dagger} H_\mathfrak{q} \right) = \bigcap_{d|N} D_d^\dagger, \tag{5.4}$$

[2]For odd N the same holds but only partially relates to the orbit size.

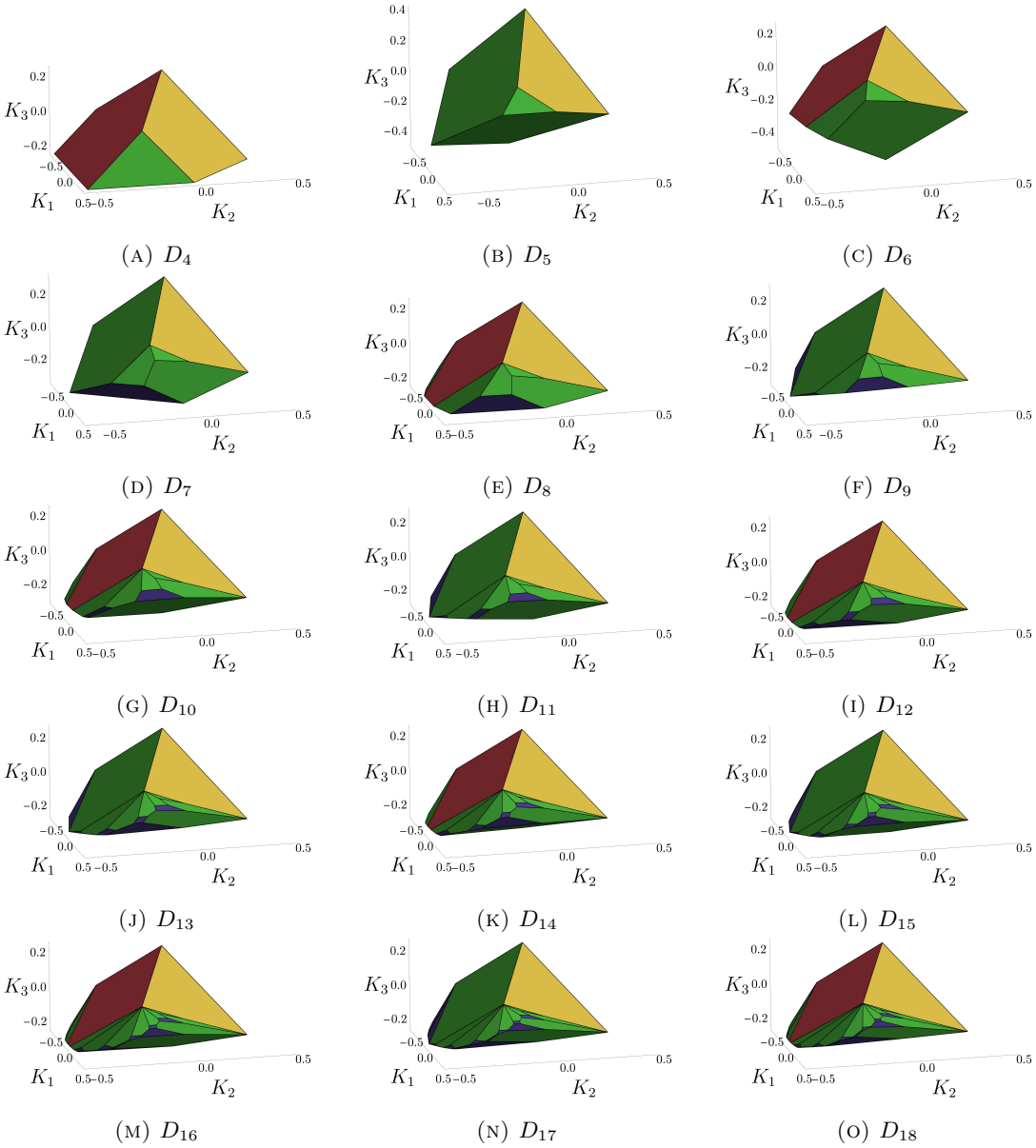

(A) D_4 (B) D_5 (C) D_6

(D) D_7 (E) D_8 (F) D_9

(G) D_{10} (H) D_{11} (I) D_{12}

(J) D_{13} (K) D_{14} (L) D_{15}

(M) D_{16} (N) D_{17} (O) D_{18}

FIGURE 5.1: Polytopes representation for all $N \in \{4, \ldots, 18\}$. The color code of the faces reflects the orbit size of the underlying mode. Yellow is used for orbit size 1, red for orbit size 2, green for orbit size 4 and blue for orbit size 8. The shape of the polytopes varies for low N, but quickly converges to a regular shape for higher N. The color alternation of the prominent wide face reflects the parity of N.

which stresses that for all $d \mid N$, $D_d \supset D_N$. The same holds in the $N \to \infty$ limit, being $\widehat{\mathfrak{U}}_\infty$ the disjoint union over all modes of complexity N, it follows

$$D_\infty = \bigcap_{N \in \mathbb{N}} D_N^\dagger, \tag{5.5}$$

which clearly implies that $D_\infty \subset D_N$ for all $N \in \mathbb{N}$, and consequently that increasing N the polyhedra converge to the same shape from "above".

5.2 Vertex Enumeration

The definition of D_N given in Eq.4.29 is known as the *half-space representation* of a convex polytope, which in general can be concisely written as a system of inequalities

$$D = \{\mathbf{x} \in \mathbb{R}^N | A \cdot \mathbf{x} \geq \mathbf{c}\}, \tag{5.6}$$

where A is a $N \times N$ matrix, and $\mathbf{c}$ a vector of constants in $\mathbb{R}^N$. The above definition encodes all the relevant information on a generic polyhedron, but does not explicitly provide knowledge on the boundaries of the faces. However, a theorem due to Minkowski [71] always guarantees the existence of an equivalent definition, known as the *vertex representation*. Basically, the polytope is defined as the convex hull over a finite set of extreme points, the vertices. Converting one representation to other is a rather subtle task that increases in complexity with the number of faces and vertices of the polyhedron. Intriguingly, it is still unknown whether the complexity of the conversion problem is, in its full generality, P or NP. Nonetheless, D_N, is always bounded for $N \geq 4$. Under this assumption a conversion algorithm, polynomial both in time and memory, exists, as it has been proven in 2006 by Avis and Fukuda[57][56]. In App.A we review the foundational ideas on the underlying working principles and their implementation in the *lrs* library[55][72] they developed. In the present work, all the polytopes are converted to a vertex representation using the aforementioned library and then rendered using Mathematica[73]. However, we could not just naively use the algorithm as it intrinsically relies on rational numbers while the inequality defining coefficients of Eq.4.18 are intrinsically irrational. Extensive pre- and post-processing of the data was required and described in App.A.3.

5.3 D_4: the Complexity

To illustrate the structure of the polytopes we shall start with a gentle example. D_1 is basically a half-space bounded by the bifurcation surface to the ferromagnetic phase. D_2 and D_3 are defined by three inequalities only as a consequence cannot intrinsically be bounded. The smaller lattice whose corresponding polytope is bounded is L_4. The description of D_4 provides an introduction to the essential phenomenological features shared by all the polytopes of higher size. Furthermore, its phases match those previously found by Landau and Binder and are shown in Fig.2.3.

In Fig.5.2b we show the polyhedron D_4 from a positive K_1 point of view. On its left, in Fig.5.2a we show the corresponding Symmetry Reduced Brillouin Zone, $\widehat{\mathfrak{U}}_4$, consisting of six possible phases, each defining one of the six different faces of D_4. The edges drawn on the SRBZ represent the neighbouring relation of the faces of the

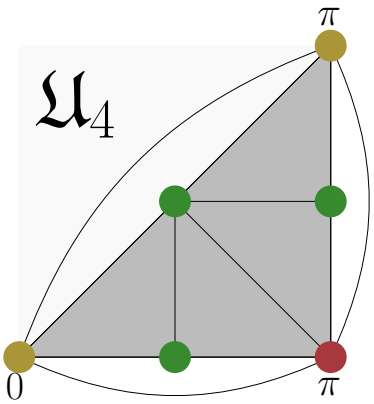

(A) Symmetry Reduced Brillouin Zone of the lattice L_4. The circles represent each of the 6 elements $\mathfrak{q} \in \widehat{\mathfrak{U}}_4$, the color code is the usual one. The drawn links show which faces are neighbours on the polytope and define the dual polytope.

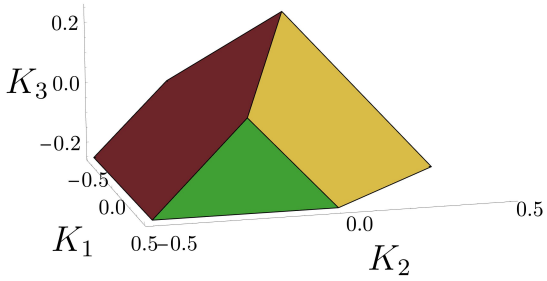

(B) D_4. From this perspective only three faces are visible. The yellow ferromagnetic face, the red striped face and the green, double striped face. Their intersection is the vertex $\mathbf{v}_R$

FIGURE 5.2: Polytope D_4 and its dual. The take home message is that all the modes with orbit size 4 emerges for negative K_3.

polyhedron. Thus, the graph they form defines the *dual polytope* of D_4. Both the polyhedron and its dual are colored respecting the convention introduced in Sec.3.1.1. Each color corresponds an orbit size, the larger N, the more relevant the color code turns out to be. Yellow is used for patterns with an orbit size of 1, red for size 2, green for size 4 and blue -here absent- for size 8.

For positive K_3 the polytope is bounded by three faces only. The yellow face, visible in the figure, has an orbit size of 1, is labelled by the mode $\mathfrak{q}_F = (0,0)$ and signals the ferromagnetic phase. It is defined by the vector $\mathbf{F}(0) = (4,4,4)^T$ which, as expected, points to all positive couplings and defines the region $K_1 > 0, K_2 > -1/3\sqrt{3}K_1$. Symmetric to it with respect to the K_1 axis, and thus hidden in the chosen point of view, lies the surface binding the region of stability of the anti-ferromagnetic phase $K_1 < 0, K_2 > 1/3\sqrt{3}K_1$. It also has an orbit size of 1 and is defined by $\mathfrak{q}_C = (\pi,\pi)$. Its orthogonal vector, $\mathbf{F}(\pi,\pi) = (-4,4,4)^T$ implies anti-ferromagnetic K_1. The third and last face found for positive K_3 is the wide red face, it indicates the bifurcation surface to the region of stability of the striped phase and is defined by $K_2 < -1/3\sqrt{3}K_1, \cap K_2 < 1/3\sqrt{3}K_1$. It has an orbit size of 2 and is defined by the mode $\mathfrak{q}_S = (\pi,0)$. Its orthogonal vector, $\mathbf{F}(0,\pi) = (0,-4,4)^T$, in agreement with the findings on the range 2 model presented in the introduction, is insensitive on the sign on K_1, but strictly points to negative values of K_2.

The other three phases, compatible with the lattice L_4, all have an orbit size of 4 and all are strictly contained in the negative K_3 region. The floor of the polytope is identified by the orthogonal vector $\mathbf{F}(\pi/2,\pi/2) = (0,0,-4)^T$, parallel to the K_3 axis. The corresponding ground state is the *double checkerboard* (see Fig.2.3). The other two phases are the so called *staggered dimer* phase and the *double striped* phase. Their defining vectors, respectively $\mathbf{F}(\pi,\pi/2) = (-2,0,0)^T$ and $\mathbf{F}(\pi/2,0) = (2,0,0)^T$, are parallel to the K_1 axis and point in opposite directions. The green triangle of Fig.5.2b is the double stripe phase, while the staggered dimer is symmetric to it but

hidden from our view.

We will now shift our attention to the dual polytope of Fig.5.2a, a better representation to understand the distribution of the vertices and their role in the phenomenology of the model. We define the *multiplicity* of a vertex to be the number of faces that it belongs to. In the dual polytope each vertex is represented by a face, thus the multiplicity can be inferred simply counting the number of edges that surround each face. The dual polytope is intuitively constructed rotating the edges by an angle of $\frac{\pi}{2}$, and, as the polytopes would be embedded in a three dimensional space. To represent it as a planar graph implies that one should stretch one vertex(face) to infinity, such that it lies "behind" the dual polytope. In the planar representation overlapping the SRBZ, this is always the vertex at the top $\mathbf{v}_T$, the meeting point of the three upper faces $\mathbf{v}_T = (0, 0, \frac{1}{4})^T$. There are other three vertices that stand out and that, not surprisingly, have a crucial role, namely those enclosed by the curved edges on the three borders of the SRBZ. These are always shared by pairs of upper faces, for reason that will become clear in Sec.5.6, we call these *multicritical vertices*. The ferromagnetic and anti-ferromagnetic faces meet in the vertex on the back $\mathbf{v}_B = (0, -\frac{1}{2}, -\frac{1}{4})^T$ and in our representation is enclosed in between the hypotenuse of the SRBZ and the curved edge. The striped face meet the other two faces respectively on the vertices $\mathbf{v}_R = (\frac{1}{2}, -\frac{1}{4}, 0)^T$ and $\mathbf{v}_L = (-\frac{1}{2}, -\frac{1}{4}, 0)^T$, enclosed between the other two curved edges and the horizontal and vertical catheti, respectively. In Fig.5.2b, $\mathbf{v}_R$ is visible and points in our direction at the intersection of the red, green and yellow faces. In the same figure, $\mathbf{v}_L$ is not visible and lies on the opposite side, symmetric with respect to the K_1 axis. All the other vertices are less interesting to describe and all have a multiplicity of three[3].

That is, the top of the polytope is bounded by the three modes only, the corners of the SRBZ. All the other faces, in this introductory example the three green phases with an orbit size of 4, appear in the anti-ferromagnetic K_3 region. These phases are in general more complex, in the sense defined in Sec.3.2. We could further comment other features, vertices and edges, however they would be related to D_4 only which is not our final goal.

5.4 D_8 and D_8: Even and Odd

In the previous paragraph we provided the basic notions on the interpretation of the order-disorder domain and its dual. To further investigate the structure of the polyhedra we need to increase N. We will here compare the polytopes D_8 and D_9 to highlight four major traits useful to classify all the polytopes. The first striking difference, also noticeable in the dual polytope, is symmetry. D_8 (as well as D_4) is symmetric with respect to the K_1 axis, while D_9 manifestly is not. The (a)symmetry is preserved on the dual polytopes of Figs.5.3a and 5.3c: the antidiagonal that links the modes $\mathfrak{q} = (\pi, 0)$ with $\mathfrak{q} = (\frac{\pi}{2}, \frac{\pi}{2})$ perfectly reflects the symmetry of the polytope. The second difference, is the number of faces, as of Eq.3.20, both polytopes are the intersection of 15 inequalities. In D_9 all the inequalities contribute with a face, as stressed in the SRBZ of Fig.5.3a (but hardly noticeble from the figure), while D_8 has

[3] Almost all vertices of all polytopes will have multiplicity of three, with one accidental exception as we will see in Sec.5.8.

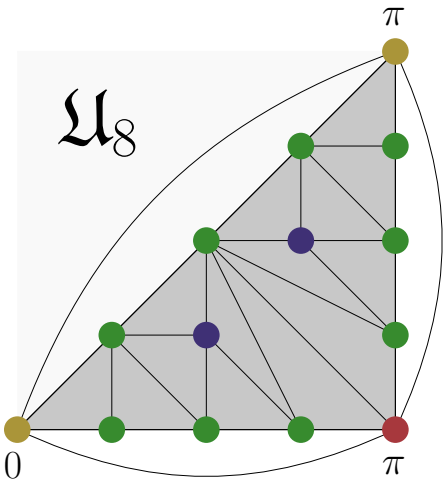

(A) Dual polyhedron of D_8. The mode $\mathfrak{q} = (\frac{3\pi}{4}, \frac{\pi}{4})$ is not plot on purpose.

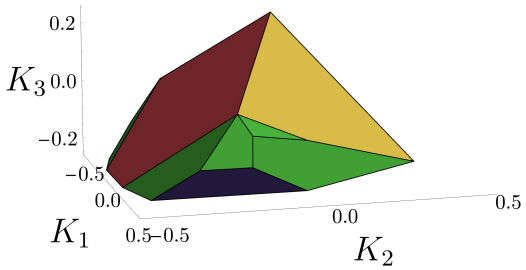

(B) Polyhedron D_8. With respect to D_4, we see that the green faces is carved by other faces, all intersecting the vertex $\mathbf{v}_R$. Moreover, we first see a blue face appearing in the lower part.

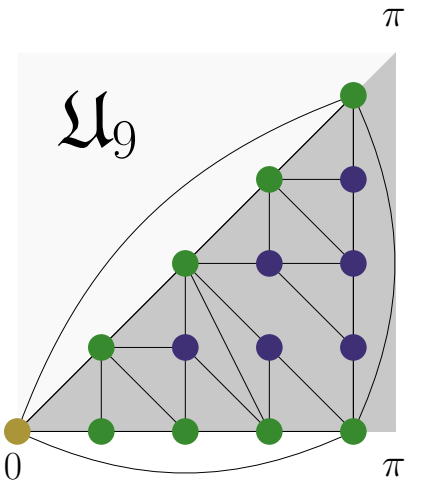

(C) Dual polytope of D_9. The shaded area in the back, $\widehat{\mathfrak{U}}_\infty$, should stress the lack of symmetry with respect to the segment running from $\mathfrak{q} = (0,0)$ to $\mathfrak{q} = (\frac{\pi}{2}, \frac{\pi}{2})$.

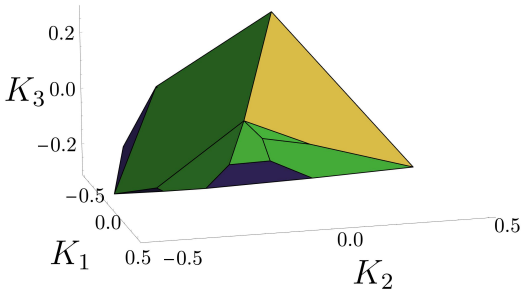

(D) Polyhedron D_9, it is less regular than D_8, shown above.

FIGURE 5.3: Comparison of an odd (D_9) and an even (D_8) polytope. Some differences are clearly noticeable: D_8 is symmetric and D_9 is not; D_8 is bounded in the front by a red face and D_9 is not; on top of $\widehat{\mathfrak{U}}_9$ we drew 15 dots, while we drew only 14 on $\widehat{\mathfrak{U}}_8$.

only 14 faces. The plane defined by $\mathfrak{q} = (\frac{3\pi}{4}, \frac{\pi}{4})$ is only tangent to the polytope on the common edge shared by the faces $\mathfrak{q} = (\frac{\pi}{2}, \frac{\pi}{2})$ and $\mathfrak{q} = (\pi, 0)$. This is relevant, we refer to this edge as the *front edge*, and its mid point as the *front vertex*[4], with coordinates $\mathbf{v}_F = (0, -\frac{1}{2}, -\frac{1}{4})^T$. Third, we compare the top of the two polytopes. As in D_4, this region is bounded by the three corner modes. The top of D_8 exactly matches the top of D_4 as the common corner modes are in $\widehat{\mathfrak{U}}_2$. The top of D_9 only shares the $\mathfrak{q} = (0, 0)$ mode, the other two corner modes, that bind the polytope in the $K_3 > 0$ region, in this case are $\mathfrak{q} = (\frac{8\pi}{9}, \frac{8\pi}{9})$ and $\mathfrak{q} = (\frac{8\pi}{9}, 0)$. The final difference regards the three multicritical vertices introduced above, whose name is now explained. Both in D_8 and D_9 each of the three multicritical vertices has multiplicity 5. D_8, shares its multicritical vertices with D_4: $\mathbf{v}_R$, $\mathbf{v}_B$ and $\mathbf{v}_L$. Furthermore, all the other vertices of D_8 are threefold. However, D_9 only shares $\mathbf{v}_L$ and $\mathbf{v}_B$, while the right multicritical vertex is slightly shifted outward.

The comparison of D_8 and D_9 served the grounds to introduce important concepts. All the differences are manifestation of the same underlying cause: eight is even and nine is odd. The physical and intuitive reason being that even patterns, for positive K_3, are always lower in energy when they can fill the checkerboard, but cannot arise on odd lattices. The deeper reason is formally rooted in function $\mathbf{F}(q)$, on which we will now leverage to formalize on general and quantitative grounds the features described above.

5.4.1 Mirror Symmetry

Symmetry is the most striking difference. D_8 is symmetric with respect to the K_1 axis, while D_9 is not. This difference is more general and reflects the symmetry of $\widehat{\mathfrak{U}}_N$ with respect to the antidiagonal segment running from $\mathfrak{q} = (0, 0)$ to $\mathfrak{q} = (\frac{\pi}{2}, \frac{\pi}{2})$ and parametrized by $\mathfrak{q}(\alpha) = (\pi - \alpha, \alpha)$ with $\alpha \in [0, \frac{\pi}{2})$. We want to show that even polytopes are always mirror symmetric, while odd polytopes are not.

The symmetry is quantitatively rooted in the parity of the cosines of $\mathbf{F}(\mathfrak{q})$. We denote with $\hat{r}$ the reflection operator on $\widehat{\mathfrak{U}}_N$, such that $\hat{r}\mathfrak{q} = (\hat{r}\mathfrak{q}_1, \hat{r}\mathfrak{q}_2) = (\pi - \mathfrak{q}_1, \pi - \mathfrak{q}_2)$. The plane defined by $\hat{r}\mathfrak{q}$ has coefficients

$$\mathbf{F}(\hat{r}\mathfrak{q}) = (F_1(\hat{r}\mathfrak{q}), F_2(\hat{r}\mathfrak{q}), F_3(\hat{r}\mathfrak{q}))^T = (-F_1(\mathfrak{q}), F_2(\mathfrak{q}), F_3(\mathfrak{q}))^T, \tag{5.7}$$

where the change of sign in $F_1(\mathfrak{q})$ is due to the parity of the cosine, while the components $F_2(\mathfrak{q})$ and $F_3(\mathfrak{q})$ are not affected by the mirror operator. In $F_2(\mathfrak{q})$ the double shift by π vanishes and the sign does not affect the cosines, in $F_3(\mathfrak{q})$ the reflection operator shifts the arguments of the cosines by on overall factor of 2π, leaving the function unchanged. That is, the bifurcation surface $K_1F_1(\hat{r}\mathfrak{q}) + K_2F_2(\hat{r}\mathfrak{q}) + K_3F_3(\hat{r}\mathfrak{q}) = -K_1F_1(\mathfrak{q}) + K_2F_2(\mathfrak{q}) + K_3F_3(\mathfrak{q}) = 1$ is mirror symmetric to $\mathbf{K} \cdot \mathbf{F}(\mathfrak{q}) = 1$, with respect to the K_1 axis.

To conclude, we only need to show that $\mathfrak{q} \in \widehat{\mathfrak{U}}_N$ implies $\hat{r}\mathfrak{q} \in \widehat{\mathfrak{U}}_N$ if and only if N is even. By theorem 3.1 a mode can in general be written as $\mathfrak{q} = (\frac{2\pi i}{N}, \frac{2\pi j}{N}) \in \mathfrak{U}_N$ with $0 \leq i \leq j < N$, the mode $\hat{r}\mathfrak{q} = (\pi - \frac{2\pi i}{N}, \pi - \frac{2\pi j}{N}) = (\frac{2\pi(N/2-i)}{N}, \frac{2\pi(N/2-j)}{N}) \in \widehat{\mathfrak{U}}_N$

[4]Clearly it is not a vertex. Nonetheless in the limit $N \to \infty$ it will become an important one ans we should already use this vocabulary.

if and only if $N/2 - i$ is an integer[5], which is clearly true if and only if N is even. The above arguments prove our prior statement that the polytopes D_N are mirror symmetric with respect to the K_1 axis if and only if N is even. Furthermore, odd polytopes systematically have more faces on the right hand side, than on the left hand side.

A straightforward consequences of the above proof, also using the definition given in Eq.5.5, is that D_∞ is mirror symmetric and that the faces defined on the antidiagonal, defined by $\mathbf{F}(\mathfrak{q}(\alpha))$ must be mirror symmetric themselves. This result paves the way to the next section.

5.4.2 Tangent Faces

We empirically observed above that in D_8 the inequality defined by $\mathfrak{q} = (\frac{3\pi}{4}, \frac{\pi}{4})$ does not emerge as a face. This is more general: among all the modes on the antidiagonal, parametrized by $\mathfrak{q}(\alpha) = (\pi - \alpha, \alpha)$ with $\alpha \in [0, \frac{\pi}{2}]$, only the two extremes emerge as a face. Explicitly substituting the parametrization in $\mathbf{F}(\mathfrak{q})$ yields

$$\mathbf{F}(\mathfrak{q}(\alpha)) = \begin{pmatrix} 2\cos(\pi-\alpha) + 2\cos(\alpha) \\ 2\cos(\pi-2\alpha) + 2\cos(\pi) \\ 2\cos(2\pi-2\alpha) + 2\cos(2\alpha) \end{pmatrix} = \begin{pmatrix} 0 \\ -2\cos(2\alpha) - 2 \\ 4\cos(2\alpha) \end{pmatrix}, \tag{5.8}$$

where, coherently with the previous section, the vector $\mathbf{F}(\mathfrak{q}(\alpha))$ has a null first component. Thus, the family of planes $\mathbf{K} \cdot \mathbf{F}(\mathfrak{q}(\alpha))$ shares the common *front edge*

$$(K_1, -\frac{1}{2}, -\frac{1}{4})^T, \tag{5.9}$$

represented in Fig.5.3b as the lowest left edge in D_8.

Clearly, the planes on the anti-diagonal only appear for even N. Among all planes whose defining mode is on the diagonal, only two contribute with a face on the polytope, those with an extreme value of α, all the others are only tangent to the polytope on the degenerate one-dimensional face lying on the common edge. Once again, the two extreme faces depend on the divisors. One of the two extremes is always the corner mode $\mathfrak{q} = (0, \pi)$ (for $\alpha = \pi$). The other extreme has a further dependence on N, we need to distinguish two cases: if $4 \mid N$ the other mode is $\mathfrak{q} = (\frac{\pi}{2}, \frac{\pi}{2})$, namely the horizontal plane which we said to be the floor of the polytope; if N is even but $4 \nmid N$, the floor is not horizontal, and it has an orbit size of 8. It can be parametrized by $\alpha = \frac{\pi(N-1)}{N}$ and in the limit of big N tends to $\alpha = \pi$.

Finally we remark that the above considerations also justifies the formula of Eq.3.30, for the number of faces of a polytope that we anticipated in Sec.3.2.1.

5.5 The Top of the Polytope, $K_3 > 0$

The position of a mode on the SRBZ relates to specific positions of the relative faces on the polytopes. Here, we begin showing the mapping of the simplest modes, the three corners of $\widehat{\mathfrak{U}}_N$, that define the pyramidal top. The top of D_4 and D_8, and of

[5] While in general always belongs to $\widehat{\mathfrak{U}}_{2N}$.

all even polytopes are defined by the modes of $\widehat{\mathfrak{U}}_2$; the top of D_9 and of the other odd polytopes only shares with them the mode $\mathfrak{q} = (0,0)$, the other two corners are different for each odd N. We can define

$$\mathfrak{q}_N = \left\lfloor \frac{N}{2} \right\rfloor \frac{2\pi}{N}, \tag{5.10}$$

to be the upper bound of $\widehat{\mathfrak{U}}_N$ on the two coordinate axis. So that, the set of modes that are mapped to the top of the polytope

$$\widehat{\mathfrak{V}}_N = \begin{cases} \{(0,0)\}, & N = 1 \\ \{(0,0),(0,\pi),(\pi,\pi)\}, & N \text{ even} \\ \{(0,0),(0,\mathfrak{q}_N),(\mathfrak{q}_N,\mathfrak{q}_N)\}, & N \text{ odd} \end{cases}. \tag{5.11}$$

For all even N, $\mathfrak{q}_N = \pi$ and $\widehat{\mathfrak{V}}_N \equiv \widehat{\mathfrak{U}}_2$. For odd N, the larger N the more its corners approach $\widehat{\mathfrak{U}}_2$ and accordingly $\lim_{N\to\infty} \mathfrak{q}_N = \pi = \mathfrak{q}_N \mid_{N \text{ even}}$. This implies that the three faces binding the pyramidal top of D_N, for odd N, are slightly tilted outward with respect to D_2: the larger N the more the top faces converge to to the even top. The intersection of the three planes defined by the three above vertices, for $N > 1$, is given by

$$\mathbf{v}_{top}(N) = \begin{cases} \mathbf{v}_T = (0,0,\frac{1}{4})^T & N \text{ even} \\ \left(\frac{1}{4}\left(1 + \frac{1}{1+2\cos(\pi\frac{N-1}{N})}\right), 0, -\frac{1}{4}\frac{1}{1+2\cos(\pi\frac{N-1}{N})}\right) & N \text{ odd} \end{cases}, \tag{5.12}$$

coherently for even N, the first line of the above equation matches $\mathbf{v}_T$ and, also in this case, for odd N $\lim_{N\to\infty} \mathbf{v}_{top}(N) = \mathbf{v}_T$.

The top of the polytope is defined in the sector $H^+ = \{\mathbf{K} | K_3 \geq 0\}$, so that for convenience we define $D_N^+ = D_N \cap H^+$. We will now show that for all N, $D_2^+ \cap D_N^+ = D_2^+$, while, using similar arguments one could show that for all odd N and M, with $N > M$, $D_N^+ \cap D_M^+ = D_N^+$. Such that, in general

$$D_N^+ = \bigcup_{\mathrm{q} \in \widehat{\mathfrak{V}}_N} H_{\mathrm{q}}. \tag{5.13}$$

The proof for even N requires to introduce the parametrization of the two right corners as $\mathfrak{q}_h(\alpha) = (\pi - \alpha, \pi - \alpha)$, which lies on the hypotenuse and $\mathfrak{q}_c(\alpha) = (\pi - \alpha, 0)$, on the vertical cathetus, both with $\alpha \in [0, \pi]$. For completeness, we remember that the third corner is always $\mathfrak{q} = (0,0)$. We now show our claim in two steps: first, we explicit the edges on the top of the polyhedron; second, we show that the even edges are always tilted inwards with respect to all the others. We identify the lines where the edges lie with the edges themselves, these are given by the three pairwise intersections

$$\begin{array}{ll} \mathbf{F}(0,0)\cdot\mathbf{K} = \mathbf{F}(0,\pi)\cdot\mathbf{K} = 1, & E_{0,1} = \{K_1 = -2K_2, K_3 - K_2 = \frac{1}{4}\}; \\ \mathbf{F}(0,0)\cdot\mathbf{K} = \mathbf{F}(\pi,\pi)\cdot\mathbf{K} = 1, & E_{0,2} = \{K_1 = 0, K_3 + K_2 = \frac{1}{4}\}; \\ \mathbf{F}(0,\pi)\cdot\mathbf{K} = \mathbf{F}(\pi,\pi)\cdot\mathbf{K} = 1, & E_{1,2} = \{K_1 = 2K_2, K_3 - K_2 = \frac{1}{4}\}; \end{array} \tag{5.14}$$

where the subscripts 0, 1 and 2 of the edges relate to the modes $\mathfrak{q} = (0,0)$, $\mathfrak{q} = (\pi,0)$ and $\mathfrak{q} = (\pi,\pi)$, respectively. Trivially, the three modes of $\widehat{\mathfrak{U}}_2$ satisfy the equality $\mathbf{F}(\mathfrak{q})\cdot E_{i,j} = 1$, for all edges $E_{i,j}$. To show our claim, that the corner modes for even

N are always more internal, our task reduces to show that for all N and for all $E_{i,j}$, $\mathbf{F}(\mathfrak{q})\cdot E_{i,j} \leq 1$, for both $\mathfrak{q}_h(\alpha)$ and $\mathfrak{q}_c(\alpha)$. More specifically, the proven symmetry allows to focus on the two edges $E_{0,1}$ and $E_{0,2}$ only. Inserting the above parametrization in Eq.4.16 yields

$$\mathbf{F}\left(\mathfrak{q}_F\right)\cdot E_{0,1} = -8K_2 + 4K_2 + 1 + 4K_2 = 1, \tag{5.15}$$

$$\begin{aligned}\mathbf{F}\left(\mathfrak{q}_c\left(\alpha\right)\right)\cdot E_{0,1} &= -2\left(2-2\cos\alpha\right)K_2 - 4\cos\alpha K_2 + \left(2+2\cos 2\alpha\right)\left(\frac{1}{4}+K_2\right)\\ &= \left(2\cos 2\alpha - 2\right)K_2 + \frac{1}{2}\left(1+\cos 2\alpha\right) \leq 1,\end{aligned} \tag{5.16}$$

$$\begin{aligned}\mathbf{F}\left(\mathfrak{q}_h\left(\alpha\right)\right)\cdot E_{0,1} &= 8\left(\cos\alpha\right)K_2 + \left(2+2\cos 2\alpha\right)K_2 + 4\cos 2\alpha\left(\frac{1}{4}+K_2\right)\\ &= \left(2+8\cos\alpha+6\cos 2\alpha\right)K_2 + \cos\alpha \leq 1, \alpha \leq \frac{\pi}{2},\end{aligned} \tag{5.17}$$

where the first equality trivially holds and represent the intuitive fact that the ferromagnetic phase pertains to any lattice. The second inequality holds for any α, while the last inequality has the special requirement that $\alpha \leq \frac{\pi}{2}$. However, this is always the case for the modes in $\hat{\mathfrak{V}}_N$, as the extremes of both $\mathfrak{q}_c(\alpha)$ and $\mathfrak{q}_h(\alpha)$ are decreasing functions of α with upper bound of $\alpha \leq 1/6\pi$ for $N = 3$. Similarly, with respect to the second edge,

$$\mathbf{F}\left(\mathfrak{q}_F\right)\cdot E_{0,2} = 4K_2 + 4\left(\frac{1}{4}-K_2\right) = 1, \tag{5.18}$$

$$\begin{aligned}\mathbf{F}\left(\mathfrak{q}_c\left(\alpha\right)\right)\cdot E_{0,2} &= -4\left(\cos\alpha\right)K_2 + \left(2+2\cos 2\alpha\right)\left(\frac{1}{4}-K_2\right)\\ &= \frac{1}{2}\left(1+\cos 2\alpha\right) - \left(2+4\cos\alpha+2\cos\alpha\right)K_2 \leq \cos\alpha \leq 1,\end{aligned} \tag{5.19}$$

$$\begin{aligned}\mathbf{F}\left(\mathfrak{q}_h\left(\alpha\right)\right)\cdot E_{0,2} &= \left(2+2\cos 2\alpha\right)K_2 + 4\cos 2\alpha\left(\frac{1}{4}-K_2\right)\\ &= \cos 2\alpha + \left(2-2\cos 2\alpha\right)K_2 \leq \frac{1}{2}\left(1+\cos 2\alpha\right) \leq 1,\end{aligned} \tag{5.20}$$

where, once again, the first equality shows the ferromagnetic phase, while, the two inequalities signal a face beyond the edge considered.

Thus, we formalized the intuition that for any even polyhedron, and consequently for the infinite polyhedron, the region of positive K_3 is bounded by the three corner modes only. The straightforward consequence, is that all the other faces bound the anti-ferromagnetic K_3 domain of D_N. Similar relations also holds for odd polyhedra that can be shown on a case by case basis, as we empirically observed.

5.6 D_{16}: the Fans

The top of the polytope has a simple structure. As we have just shown, it is always bounded by three faces only, the corner modes. All the other faces emerge in the negative K_3 sector. Here, we address to which phases the borders of $\widehat{\mathfrak{U}}_N$ are mapped. For even N, the borders correspond to all the modes with size 4, which hints an

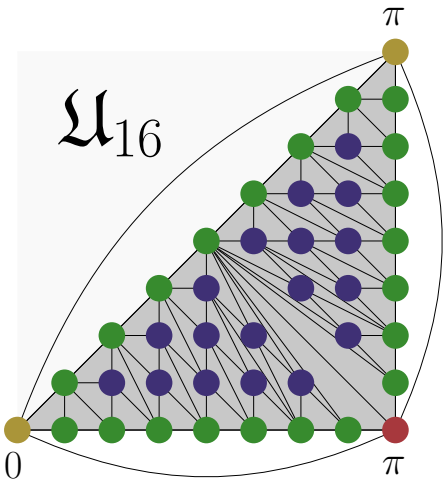

(A) Dual polytope of D_{16}.

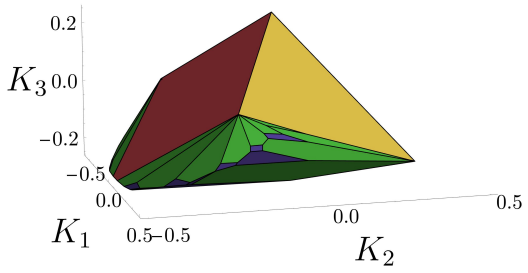

(B) D_{16}. We clearly see the right fan opening toward the proposed point of view. The underlying modes all lie on the horizontal cathetus. We further see half of the bottom fan, opening from $\mathbf{v}_B$. All the modes with an orbit size of 8 lie at the intersection of the two fans.

FIGURE 5.4: D_{16} and its dual.

intriguing relation[6] among the orbit size and the position of the face on the dual polytope. To illustrate this feature, we describe here D_{16}, shown in Fig.5.4b. The simplest polytope that clearly manifests this feature in all its regularity.

Leveraging on the tools provided, we already have some insights, 16 is even and hence the polytope is symmetric. This also implies that out of the 45 defining inequalities, only 42 faces appear, as the three modes on the anti-diagonal are only tangent to the front edge lying on the line $\mathbf{K} = (K_1, -\frac{1}{2}, -\frac{1}{4})^T$. Its top is defined by the corners of $\mathfrak{U}_{16}$: $\mathfrak{q} = (0,0)$, $\mathfrak{q} = (\pi, 0)$ and $\mathfrak{q} = (\pi, \pi)$, are the sole faces emerging in the $K_3 > 0$ domain. All the other modes have an orbit size of 4 or 8 and are all constrained in the $K_3 < 0$ region.

On the set $\widehat{\mathfrak{U}}_N$ (for even N), the faces with an orbit size of 4 appear on three sides of the triangle. Each side shares a unique vertex which we named multicritical point. More specifically, on D_{16}, such multicritical points are the intersection of 9 faces, two of these faces are corner modes while the other 7 are organized in a green fan, as clearly observed in Fig.5.4b; we see the fan opening from $\mathbf{v}_R$, accordingly, we name it *right fan*. Symmetric to it, but hidden from our perspective, there is the *left fan*. Furthermore, in the same figure, we see only half of the *bottom fan*, that opens from the vertex $\mathbf{v}_B$.

The faces opening on the right fan are parametrized by $\mathfrak{q} = (\alpha, 0)$, $\alpha \in (0, \pi)$. Acccordingly, the vertex $\mathbf{v}_R = (\frac{1}{2}, -\frac{1}{4}, 0)^T$ is a common point of all the planes

$$\mathbf{v}_R \cdot \mathbf{F}(\mathfrak{q}(\alpha)) = \frac{1}{2}(2 + 2\cos(\alpha)) - \frac{1}{4}4\cos(\alpha) + 0 \cdot (2\cos(2\alpha) + 2) = 1. \tag{5.21}$$

[6]The same does not hold for odd N. The vertical border has an orbit size of 8. However, this property holds for $N \to \infty$ and is relevant to stress.

The real space patterns corresponding to the right fan are stripes modulated by the wave vector, $\mathfrak{q}_1$. The fan opens toward negative K_3 spanning all the phases commensurate with the given size from the ferromagnetic phase (infinite period) to the striped phase (minimal period). The vertical cathetus is parametrized by $\mathfrak{q} = (\pi, \alpha)$, $\alpha \in (0, \pi)$. Accordingly, the vertex $\mathbf{v}_L = (-\frac{1}{2}, -\frac{1}{4}, 0)^T$ is a common point and $\mathbf{v}_L \cdot \mathbf{F}(\mathfrak{q}(\alpha)) = 1$. The corresponding patterns are modulated on one direction with the vector π, a pure anti-ferromagnetic alternation of up and down spins. In the other direction the modulation varies from a 0 modulation (simple striped pattern) up to a π modulation (pure anti-ferromagnetic pattern). We refer to the underlying patterns as *staggered n-mers*. Lastly, we parametrize the hypotenuse with $\mathfrak{q} = (\alpha, \alpha)$. As before, all the planes pass through $\mathbf{v}_B = (0, \frac{1}{2}, -\frac{1}{4})^T$

$$\mathbf{v}_B \cdot \mathbf{F}(\mathfrak{q}(\alpha)) = \frac{1}{2}(2 + 2\cos(2\alpha)) - \frac{1}{4}4\cos(2\alpha) = 1. \tag{5.22}$$

Beyond them, we find *chessboard-like* patterns, with a modulated square size. The fan opens from the ferromagnetic (squares with infinite periods) to the minimal square of the Neel ordered phase. In the final part of this chapter we will see how the fan converges to cones when we let $N \to \infty$. Reflecting the symmetry of the polytope, the left and right fans are confined respectively in the negative and the positive K_1 region. The bottom fan widely spans the whole K_1 axis, going from $\mathbf{v}_L$ up to $\mathbf{v}_B$. The adjacency relations of all the faces are rather simple. As shown in the dual polytope, shown in Fig.5.4a. Within the individual fans, the faces are linearly ordered and only meet all together in the common vertex. There are only two inter-fan adjacency relations, found right next to the left and right vertices. All the other adjacency relations are prohibited by the blue faces, the bulk of $\widehat{\mathfrak{U}}_{16}$, all with an orbit size of 8, that arise at the intersection of the three cones. In Sec.5.8, we will address their complicated distribution only empirically. It is essential to notice a final important detail: all the blue faces intersect the common plane $S = \{\mathbf{K} \mid K_2 = 2K_3\}$, which we call the *seam plane*. The fundamental importance of this will be clarified in the next paragraph.

5.7 The Natural Coordinate Frame

The Fourier transform of the lattice, as previously remarked, encodes all the information on the polytope. It is a function $\mathbf{F} : \mathbb{R}^2 \to \mathbb{R}^3$, that maps the Symmetry Reduced Brillouin Zone to a surface embedded in $\mathbb{R}^3$. This hints to a dependence between the three components of $\mathbf{F}$. By highlighting this natural relation we both underline the importance of the seam plane $K_2 = 2K_3$ and introduce two practical advantages. On the one hand, it simplifies the calculation of the surface reconstruction of D_∞ that we will provide in Sec.5.9. On the other hand, it yields a more robust representation of the dual polyhedra, as we will subsequently see. Such a relation is nothing else than a rotation of the reference frame. We remark, that the proposed frame is a mathematical construction and physical insights are better understood in the $(K_1, K_2, K_3)^T$ reference frame. Accordingly, all the proposed results will be brought back to the original frame.

Expanding $\mathbf{F}(\mathfrak{q}_1, \mathfrak{q}_2)$ in terms of $\cos(\mathfrak{q}_1)$ and $\cos(\mathfrak{q}_2)$ only

$$\mathbf{F}(\mathfrak{q}_1, \mathfrak{q}_2) = \begin{pmatrix} 2\cos(\mathfrak{q}_1) + 2\cos(\mathfrak{q}_2) \\ 2\cos(\mathfrak{q}_1 - \mathfrak{q}_2) + 2\cos(\mathfrak{q}_1 + \mathfrak{q}_2) \\ 2\cos(2\mathfrak{q}_1) + 2\cos(2\mathfrak{q}_2) \end{pmatrix} = \begin{pmatrix} 2\cos(\mathfrak{q}_1) + 2\cos(\mathfrak{q}_2) \\ 4\cos(\mathfrak{q}_1)\cos(\mathfrak{q}_2) \\ 4(-1 + \cos^2(\mathfrak{q}_1) + \cos^2(\mathfrak{q}_2)) \end{pmatrix}, \tag{5.23}$$

explicitly hints at the relation of interest

$$\begin{aligned} F_1^2(\mathfrak{q}) &= (2\cos(\mathfrak{q}_1) + 2\cos(\mathfrak{q}_2))^2 \\ &= 4(-1 + \cos^2(\mathfrak{q}_1) + \cos^2(\mathfrak{q}_2)) + 8\cos(\mathfrak{q}_1)\cos(\mathfrak{q}_2) + 4 = F_3(\mathfrak{q}) + 2F_2(\mathfrak{q}) + 4. \end{aligned} \tag{5.24}$$

which introduces the "natural" parametrization of $\mathbf{F}(\mathfrak{q})$

$$\begin{aligned} \mathbf{F}(\mathfrak{q}_1, \mathfrak{q}_2) &= F_1(\mathfrak{q}_1, \mathfrak{q}_2)\hat{\mathbf{e}}_1 + F_2(\mathfrak{q}_1, \mathfrak{q}_2)\hat{\mathbf{e}}_2 + F_3(\mathfrak{q}_1, \mathfrak{q}_2)\hat{\mathbf{e}}_3 \\ &= F_1(\mathfrak{q}_1, \mathfrak{q}_2)\hat{\mathbf{n}}_1 + (F_2(\mathfrak{q}_1, \mathfrak{q}_2) - 2F_3(\mathfrak{q}_1, \mathfrak{q}_2))\hat{\mathbf{n}}_2 + (2F_2(\mathfrak{q}_1, \mathfrak{q}_2) + F_3(\mathfrak{q}_1, \mathfrak{q}_2))\hat{\mathbf{n}}_3, \end{aligned} \tag{5.25}$$

where

$$\begin{aligned} \hat{\mathbf{n}}_1 &= (1, 0, 0)^T, \\ \hat{\mathbf{n}}_2 &= (0, \tfrac{1}{\sqrt{5}}, -\tfrac{2}{\sqrt{5}})^T, \\ \hat{\mathbf{n}}_3 &= (0, \tfrac{2}{\sqrt{5}}, \tfrac{1}{\sqrt{5}})^T, \end{aligned} \tag{5.26}$$

is the orthonormal basis that decouples the relation of Eq.5.24. So that we can introduce the coordinates $\varphi_j \equiv \mathbf{F}(\mathfrak{q}) \cdot \hat{\mathbf{n}}_j$. Explicitly

$$\begin{aligned} \varphi_1 &= 2\cos(\mathfrak{q}_1) + 2\cos(\mathfrak{q}_2), \\ \varphi_2 &= 4\cos(\mathfrak{q}_1)\cos(\mathfrak{q}_2) - 8(-1 + \cos^2(\mathfrak{q}_1) + \cos^2(\mathfrak{q}_2)), \\ \varphi_3 &= \varphi_1^2 - 4, \end{aligned} \tag{5.27}$$

finally, in this basis the vector defining the polytope reads

$$\mathbf{F}(\varphi_1, \varphi_2) = \varphi_1\hat{\mathbf{n}}_1 + \varphi_2\hat{\mathbf{n}}_2 + \frac{1}{\sqrt{5}}(\varphi_1^2 - 4)\hat{\mathbf{n}}_3. \tag{5.28}$$

In $\mathbf{K}$ space, the transformation induced by Eq.5.24 is a counterclockwise rotation around the K_1 axes by an angle of $\theta = \arctan(2)$. The transformation has the impressive consequence that tilts vertically the plane $K_2 = 2K_3$, where all the faces of orbit size 8 tend to converge.

We could also regard the transformation as a mapping from the vectors $\mathfrak{q} = (\mathfrak{q}_1, \mathfrak{q}_2) \in \mathfrak{U}_\infty$ to the vectors $\varphi = (\varphi_1, \varphi_2) \in \Phi_\infty$. Of which we now investigate the boundaries. The $\mathfrak{q}$ vectors are separately constrained as $0 \leq \mathfrak{q}_1 \leq \pi$ and $0 \leq \mathfrak{q}_2 \leq \pi$, which clearly yields $\varphi_1 \in [-4, 4]$. What remains to determine is the relation between φ_1 and φ_2, which is encoded in the first two lines of Eq.5.27. Inverting, we find

$$\varphi_2 = -2\frac{10\cos^2(\mathfrak{q}_1) - \varphi_1\cos(\mathfrak{q}_1) + \varphi_1^2 - 4}{\sqrt{5}}. \tag{5.29}$$

We recall that our interest is in the value at the border of $\widehat{\mathfrak{U}}_\infty$. The constrains of the

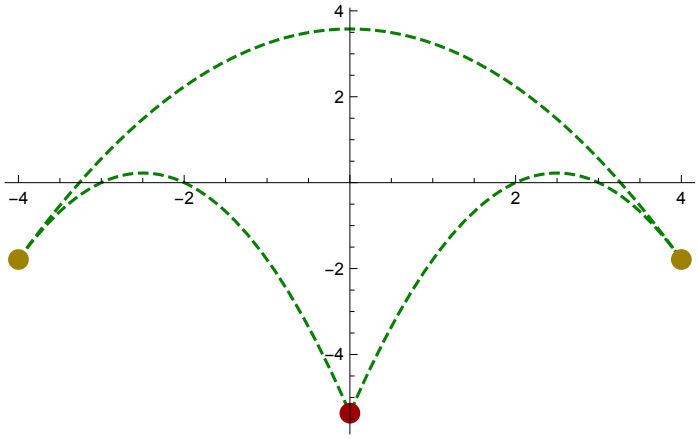

FIGURE 5.5: Domain boundaries of Φ_∞. The right and left yellow circles are the points $\mathfrak{q} = (0, 0)$ and $\mathfrak{q} = (\pi, \pi)$, the red circle is the point $\mathfrak{q} = (0, \pi)$, while the green lines, given by Eq.5.30 are the hypothenuse on top and the two catheti the lower bound. Basically the change of coordinates rotates the the set $\widehat{\mathfrak{U}}_\infty$ and than bends the two tips externally.

hypotenuse and the two catheti yields the boundary $\cos(\mathfrak{q}_1) \in [\max(-1, \frac{1}{2}\varphi_1 - 1), \frac{1}{4}\varphi_1]$. Plugging the boundaries in the above equation finally yields

$$\Phi_\infty = \{(\varphi_1, \varphi_2) \in \mathbb{R}^2 \mid -4 < \varphi_1 < 4, -\frac{2}{\sqrt{5}}(2 - |\varphi_1|)(3 - \varphi_1) < \varphi_2 < \frac{2}{\sqrt{5}}(4 - \frac{3}{8}\phi_2)\}, \tag{5.30}$$

which is graphically represented in Fig.5.5. The green boundaries are the two limiting curves given in the above equation, the three colored dots represent the three modes of $\widehat{\mathfrak{U}}_2$ and have the usual color coding for the orbit size. The rotated reference frame not only tilts the seam plane parallel to two of the axes it also induces the mapping of $\widehat{\mathfrak{U}}_\infty$ to Φ_∞, as we will see in the subsequent section, a better representation of the dual polytopes.

5.8 D_{32}: Dual Polytopes

So far we have explored the structure of D_N limiting our treatment to the corners and the borders of the SRBZ. Nonetheless, the vast majority of the modes, as N increases are in the bulk. Their adjacency relations are more complicated and we will address their distribution only empirically in the description of D_{32}. To this end, it is useful to first understand the advantage mentioned above in representing the dual polytopes introduced by the rotated coordinate frame.

The dual polyhedra are planar graphs and always[7] verify Euler's relation

$$V + E - F = 2, \tag{5.31}$$

where V is number of vertices, E the number of edges and F the number of faces (we recall that in the dual the role of faces and vertices is inverted). The graphs of D_4, D_8,

[7] It has been verified for all N up to 16, for all even N up to 32, for $N = 48$ and $N = 64$.

D_9 and D_{16}, presented above, are the result of an exact numerical processing of the vertices coordinates. For $N > 16$ the graphical representation of the dual polyhedra above $\widehat{\mathfrak{U}}_\infty$ may have overlapping straight edges. Moreover, any affine transformation of the set $\widehat{\mathfrak{U}}_N$ would map crossing edges to crossing edges and would not provide a planar representation. The issue is solved by the rotated reference frame, that systematically disentangles the dual graphs. In Fig.5.6 we show the dual polytopes drawn above Φ_∞, for all even N from $N = 4$ to $N = 32$.

The deeper reason of the disentanglement lies in the parametrization of $\varphi_1 = \cos(\mathfrak{q}_1) + \cos(\mathfrak{q}_2)$, which introduces a linear ordering of all the modes along the intersection with the seam plane. From right to left the plane intersects all the phases ordered according to the value of φ_1. And this explains why no edge crossing is observed up to $N = 16$: for all $N \leq 16$ it holds that if $\mathfrak{q}_1 > \mathfrak{q}_2$ then $\cos(\mathfrak{q}_1) > \cos(\mathfrak{q}_2)$. When this relation breaks down there is an overlap in between the edges.

For a more concrete picture of the linear ordering we suggest to look at Fig.5.7, where we depict[8] D_{32} and more specifically at Fig.5.7a, where we show a detail of it, the region where the right fan meets the bottom fan. The general structure of the polytope should now be clear and we will focus on the blue faces. First, we notice that all the blue faces are smaller than in the polytope D_{16} and even more clustered around the common plane. Second, that the seam plane effectively crosses all the faces. Lastly, that also the face with orbit size 8 appear to be regularly distributed. The dual polytope is the last plot of Fig.5.6, it encodes the adjacency relation. All the duals are plotted numerically but with the exact values, however these, could in principle be drawn following two simple rules, of which we here give a rudimental prescription. First, one connects all the modes on Φ_N with the broken line that follows from the linear ordering introduced above, connecting $\mathfrak{q} = (0, 0)$ to $\mathfrak{q} = (\pi, \pi)$. The second step is somewhat more complicated. all the other edges of the dual polytope respect the bifurcation process observed in the detail of D_{32} shown in Fig.5.7a, that we will now describe. From each pair of blades in the lower fan, we see elongated blue triangles regularly appearing at all intersections. More specifically, if we zoom in, as shown in Fig5.7a, we see that from each face of each fan, a bifurcation structure[9] of the blue faces appears. The regularity of this structure is consequently observed on the dual polytopes and breaks down when it reaches the seam. Where the distribution of the faces depends on the φ_1 ordering.

This further explains the observed vertex multiplicities. Other than the multicritical vertices, all other vertices are the intersection of three faces only, made exception, for those accidental cases where two modes have the same φ_1 value.

Finally, before moving to the description of D_∞ we propose in table a summary on the number of faces, phases, vertices and edges for all even N polyhedra up to $N = 48$.

[8] We remark that the one shown is still the original reference frame.

[9] A similar behavoiur has been previously observed both in the ANNNI model, but in temperature and by Grousson[39].

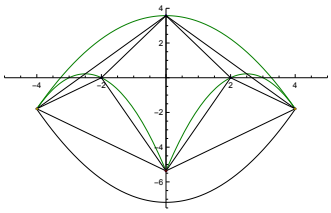

(A) D_4 adjacency graph.

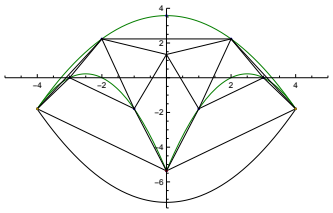

(B) D_6 adjacency graph.

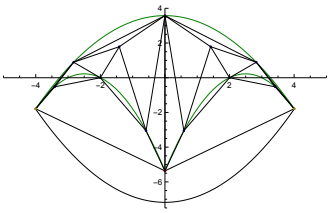

(C) D_8 adjacency graph.

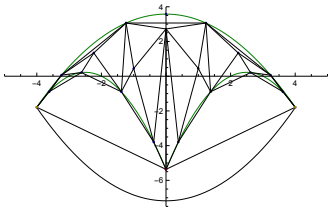

(D) D_{10} adjacency graph.

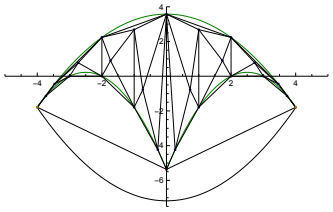

(E) D_{12} adjacency graph.

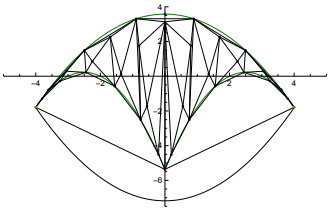

(F) D_{14} adjacency graph.

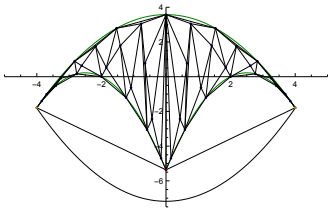

(G) D_{16} adjacency graph.

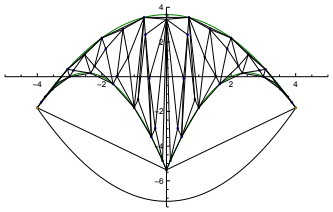

(H) D_{18} adjacency graph.

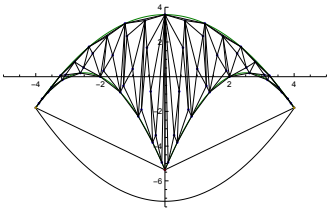

(I) D_{20} adjacency graph.

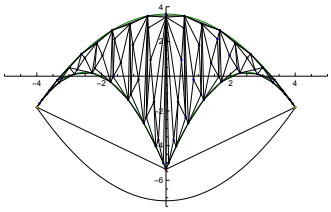

(J) D_{22} adjacency graph.

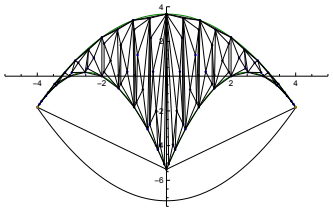

(K) D_{24} adjacency graph.

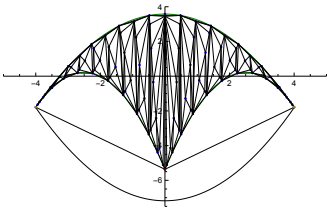

(L) D_{26} adjacency graph.

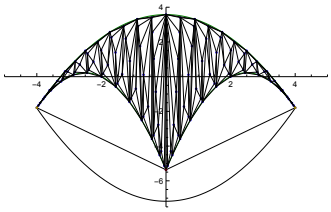

(M) D_{28} adjacency graph.

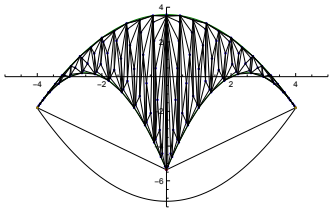

(N) D_{30} adjacency graph.

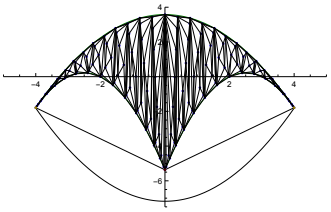

(O) D_{32} adjacency graph.

FIGURE 5.6: Adjacency graphs for the dual polyhedra in the preferred coordinate frame for all even N from 4 to 32. All the graphs are planar.

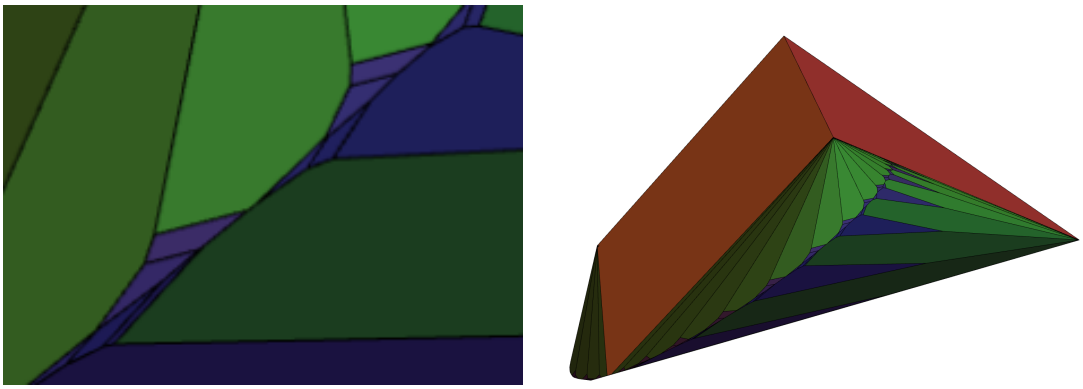

(A) Detail of D_{32}. We clearly observe the bifurcation structure of the adjacency relation of the bulk of the dual polytopes

(B) D_{32}. The fans are more pronounced, the faces with orbit size 8 smaller in surface and more clustered around the seam plane

FIGURE 5.7: D_{32} and a detail of it.

5.9 Construction of D_∞

The structure of D_N explored in the previous section is not only fascinating but also provides crucial ingredients in testing the framework with simulations. However, as it is common practice in physics we aim to construct D_∞, as the behaviour of the system is truthfully observed in the thermodynamic limit. The top of the polytope, as proved in Sec.5.5, should still coincide with D_2^+, while all the other infinite faces only bind the bottom. In the thermodynamic limit the three fans should converge to three smooth cones where each fan face squeeze to a single rule. The three cones should meet on a single one-dimensional line, the *seam*, parametrized by φ_1, where all the modes with orbit multiplicity 8 converge.

To construct the infinite polyhedron D_∞, we leverage on both the theory of convex bodies and of ruled surfaces. A convex manifold is in general completely determined by the normal vector at each point. Thus our starting point is $\mathbf{F}(\mathfrak{q}_1, \mathfrak{q}_2) : \widehat{\mathfrak{U}}_\infty \to D_\infty$. However, the calculation is tremendously simplified in the natural frame of coordinates previously presented. Thus, we will work in the Φ_∞ domain and eventually, we will rotate the final surface back to the original frame of reference.

N	4	6	8	10	12	14	16	18	20	22	24	26	28	30	32
F	6	10	14	20	26	34	42	52	62	74	86	100	114	130	146
V	8	13	18	27	36	49	62	77	94	117	134	163	188	215	246
E	12	21	30	45	60	81	102	127	154	189	218	261	300	343	390
V_4	0	0	0	0	0	0	2	2	0	4	0	0	2	0	0

TABLE 5.1: Polyhedra data for the first 14 sets. Where N is the maximum size of periodicity allowed; F the number of faces; V the number of vertices; E the number of edges; V_4 the number of pairs of spurious vertices that have to be controlled analytically.

5.9.1 The Seam

We will show that a set of solutions for

$$\mathbf{K} \cdot \mathbf{F}(\varphi_1, \varphi_2) = 1, \tag{5.32}$$

is a curve $S(\varphi_1)$, that does not depend on φ_2: we call this curve the *seam*. Convex body theory allows to decompose the solutions of the above equation as a linear combination of the normal unit vector and its derivatives, without imposing any previous knowledge we assume a general dependence on φ_2.

For further convenience, as it is common practice, we bring the function in normalized form

$$\mathbf{K} \cdot \hat{\mathbf{u}}(\varphi_1, \varphi_2) = \frac{1}{|\mathbf{F}(\varphi_1, \varphi_2)|} \equiv h(\varphi_1, \varphi_2), \tag{5.33}$$

where we introduced both the unit normal vector

$$\hat{\mathbf{u}}(\varphi_1, \varphi_2) = \frac{\mathbf{F}(\varphi_1, \varphi_2)}{|\mathbf{F}(\varphi_1, \varphi_2)|} = \frac{1}{\sqrt{\frac{1}{5}(16 - 3\varphi_1^2 + \varphi_1^4) + \varphi_2^2}} \begin{pmatrix} \varphi_1 \\ \varphi_2 \\ \varphi_1^2 - 4 \end{pmatrix}, \tag{5.34}$$

and the support function

$$h = \frac{1}{\sqrt{\frac{1}{5}(16 - 3\varphi_1^2 + \varphi_1^4) + \varphi_2^2}}, \tag{5.35}$$

basically the normalization constant.

The partial derivatives of the normal vector $\hat{\mathbf{u}}$

$$\begin{aligned} \partial_1 \hat{\mathbf{u}} &= \tfrac{1}{(\varphi_1^4 - 3\varphi_1^2 + 5\varphi_2^2 + 16)^{3/2}} \begin{pmatrix} \sqrt{5}\left(-\varphi_1^4 + 5\varphi_2^2 + 16\right) \\ \sqrt{5}\varphi_1\left(3 - 2\varphi_1^2\right)\varphi_2 \\ 5\varphi_1\left(\varphi_1^2 + 2\varphi_2^2 + 4\right) \end{pmatrix}, \\ \partial_2 \hat{\mathbf{u}} &= \tfrac{1}{(\varphi_1^4 - 3\varphi_1^2 + 5\varphi_2^2 + 16)^{3/2}} \begin{pmatrix} \varphi_1\varphi_2 \\ \sqrt{5}\left(\varphi_1^4 - 3\varphi_1^2 + 16\right) \\ 5\left(\varphi_1^2 - 4\right)\varphi_2 \end{pmatrix}, \end{aligned} \tag{5.36}$$

span the tangent plane to the surface $S(\varphi_1, \varphi_2)$ and by definition the above derivatives are orthogonal to $\hat{\mathbf{u}}$. Thus, the triple $\{\hat{\mathbf{u}}, \partial_1\hat{\mathbf{u}}, \partial_2\hat{\mathbf{u}}\}$ form an orthogonal basis on every point of the surface. This implies that any decomposition of $S(\varphi_1, \varphi_2)$ of the form

$$\mathbf{S}(\varphi_1, \varphi_2) = h(\varphi_1, \varphi_2)\hat{\mathbf{u}}(\varphi_1, \varphi_2) + \gamma_1(\varphi_1, \varphi_2)\partial_1\hat{\mathbf{u}}(\varphi_1, \varphi_2) + \gamma_2(\varphi_1, \varphi_2)\partial_2\hat{\mathbf{u}}(\varphi_1, \varphi_2), \tag{5.37}$$

satisfies Eq.5.32, where we introduced the simplified the notation $\frac{\partial}{\partial q_i} \equiv \partial_i$.

An equation for the coefficients $\boldsymbol{\gamma} = (\gamma_1, \gamma_2)^T$ can be found deriving the support function

$$\begin{aligned} \partial_i h(\varphi_1, \varphi_2) &= (\partial_i \hat{\mathbf{u}}(\varphi_1, \varphi_2))\mathbf{S}(\varphi_1, \varphi_2) + \hat{\mathbf{u}}(\varphi_1, \varphi_2)(\partial_i \mathbf{S}(\varphi_1, \varphi_2)) \\ &= (\partial_i \hat{\mathbf{u}}(\varphi_1, \varphi_2))\mathbf{S}(\varphi_1, \varphi_2), \end{aligned} \tag{5.38}$$

where the second term vanishes because the derivatives of $\partial_i \mathbf{S}(\varphi_1, \varphi_2)$ is trivially orthogonal to $\hat{\mathbf{u}}(\varphi_1, \varphi_2)$. Introducing the ansatz of Eq.5.37 in the above derivative, sets an equation for the coefficients γ_1 and γ_2

$$(\partial_1 \hat{\mathbf{u}}) \cdot \mathbf{S} = \gamma_1 \partial_1 \hat{\mathbf{u}} \cdot \partial_1 \hat{\mathbf{u}} + \gamma_2 \partial_1 \hat{\mathbf{u}} \cdot \partial_2 \hat{\mathbf{u}} = \partial_1 h, \tag{5.39}$$

$$(\partial_2 \hat{\mathbf{u}}) \cdot \mathbf{S} = \gamma_1 \partial_2 \hat{\mathbf{u}} \cdot \partial_1 \hat{\mathbf{u}} + \gamma_2 \partial_2 \hat{\mathbf{u}} \cdot \partial_2 \hat{\mathbf{u}} = \partial_2 h, \tag{5.40}$$

which in matricial form is

$$\begin{pmatrix} \partial_2 \hat{\mathbf{u}} \cdot \partial_2 \hat{\mathbf{u}} & -\partial_1 \hat{\mathbf{u}} \cdot \partial_2 \hat{\mathbf{u}} \\ -\partial_2 \hat{\mathbf{u}} \cdot \partial_1 \hat{\mathbf{u}} & \partial_1 \hat{\mathbf{u}} \cdot \partial_1 \hat{\mathbf{u}} \end{pmatrix} \begin{pmatrix} \gamma_1 \\ \gamma_2 \end{pmatrix} = \begin{pmatrix} \partial_1 h \\ \partial_2 h \end{pmatrix}. \tag{5.41}$$

By inverting the above equation, we find

$$\begin{pmatrix} \gamma_1 \\ \gamma_2 \end{pmatrix} = \frac{1}{\Delta(\hat{\mathbf{u}})} \begin{pmatrix} \partial_2 \hat{\mathbf{u}} \cdot \partial_2 \hat{\mathbf{u}} & -\partial_1 \hat{\mathbf{u}} \cdot \partial_2 \hat{\mathbf{u}} \\ -\partial_2 \hat{\mathbf{u}} \cdot \partial_1 \hat{\mathbf{u}} & \partial_1 \hat{\mathbf{u}} \cdot \partial_1 \hat{\mathbf{u}} \end{pmatrix} \begin{pmatrix} \partial_1 h \\ \partial_2 h \end{pmatrix}, \tag{5.42}$$

where $\Delta(\hat{\mathbf{u}})$ is the determinant of the Jacobian of $\mathbf{u}(\varphi_1, \varphi_2)$. The explicit calculation yields

$$\gamma_1 = \frac{\varphi_1 \left(3 - 2\varphi_1^2\right) \sqrt{\varphi_2^2 + \frac{1}{5}\left(\varphi_1^4 - 3\varphi_1^2 + 16\right)}}{\left(\varphi_1^2 + 4\right)^2}, \tag{5.43}$$

$$\gamma_2, = -\frac{\left(4\varphi_1^2 + 5\right) \varphi_2 \sqrt{\varphi_2^2 + \frac{1}{5}\left(\varphi_1^4 - 3\varphi_1^2 + 16\right)}}{\left(\varphi_1^2 + 4\right)^2}. \tag{5.44}$$

Finally we plug the above result in the ansatz of Eq.5.37, and the seam finally reads

$$S(\varphi_1) = \begin{pmatrix} \frac{2\varphi_1}{4+\varphi_1^2} \\ 0 \\ -\frac{\sqrt{5}}{4+\varphi_1^2} \end{pmatrix}, \tag{5.45}$$

independently on φ_2, or equivalently in the original frame

$$S(\mathfrak{q}) = \begin{pmatrix} \frac{2(2\cos(\mathfrak{q}_1)+2\cos(\mathfrak{q}_2))}{4+(2\cos(\mathfrak{q}_1)+2\cos(\mathfrak{q}_2))^2} \\ -\frac{2}{4+(2\cos(\mathfrak{q}_1)+2\cos(\mathfrak{q}_2))^2} \\ -\frac{1}{4+(2\cos(\mathfrak{q}_1)+2\cos(\mathfrak{q}_2))^2} \end{pmatrix}. \tag{5.46}$$

This result formalizes both our previous claim of a linear ordering of the modes, and that all the modes with an orbit size 8 shrink to a single point. In a certain sense, the seam can be interpreted as a manifestation of the devil's staircase modulated by a parameter rather than temperature.

5.9.2 Ruled Surfaces

In Sec.5.6 we showed that the modes with orbit size 4 bifurcates from the disorder region on faces distributed as fans opening from each of the three multicritical vertices $\mathbf{v}_L$, $\mathbf{v}_R$, $\mathbf{v}_B$. In the infinite limit each face shrinks to a single rule and the fans becomes skewed cones which we name $\mathbf{C}_B$, $\mathbf{C}_L$ and $\mathbf{C}_R$. Mathematically, the cones are the

envelopes of a one parameter family of planes with vanishing gaussian curvature, thus can be described in the formalism of developable surfaces[74].

Without loss of generality, we parametrize the cones as ruled surfaces

$$\mathbf{C}_i(\varphi_1, t) = \mathbf{S}(\varphi_1) + t\mathbf{r}_i(\varphi_1), \tag{5.47}$$

where $\mathbf{S}$ is the seam, $\mathbf{r}_i$ are the director coefficients and t a real parameter. A ruled surface is developable[75] when the vectors $(\mathbf{r}_i, \frac{d\mathbf{r}_i}{d\varphi_1}, \frac{d\mathbf{S}}{d\varphi_1})$ are linearly dependent

$$\det(\mathbf{r}_i, \frac{d\mathbf{r}_i}{d\varphi_1}, \frac{d\mathbf{S}}{d\varphi_1}) = 0. \tag{5.48}$$

The above condition is met if we assume that the director of coefficents is of the form

$$\mathbf{r}_i = \mathbf{S} - \mathbf{v}_i, \tag{5.49}$$

where $\mathbf{v}_i$ are the coordinates of the three multicritical vertices, first mentioned in Sec.5.3. Thus, the task of finding a parametric equation for the cones reduces to verify that the normal vector to the cones evaluated at the seam ($t = 0$) matches the normal vector $\mathbf{F}(\varphi_1, \varphi_2)$. As before we compute the normal vector to the cone as the cross product of the partial derivatives

$$\mathbf{N}_i(\varphi_1, t) = \frac{\partial \mathbf{C}_i}{\partial \varphi_1} \times \frac{\partial \mathbf{C}_i}{\partial t} = \frac{d\mathbf{S}}{d\varphi_1} \times \mathbf{r}_i(\varphi_1) + t\frac{d\mathbf{r}_i}{d\varphi_1} \times \mathbf{r}_i(\varphi_1). \tag{5.50}$$

The two vectors, although supposedly parallel, are not equal in length and to effectively compare the two we need to find the scaling constant. Without loss of generality, the scaling constant is found taking the ratio $|\mathbf{F}(\varphi_1, \varphi_{2,\max})|/|\mathbf{N}_i(\varphi_1, 0)|$, which yields $\frac{1}{2}(\varphi_1^2+4)^2$ for the bottom cone and $-2(\varphi_1^2+4)^2$ for the left and right cones, where the minus indicates that the two vectors are anti-parallel. With this magnitude correction, we proceed verifying that the two cones satisfy the mentioned relation.

We begin with the bottom cone. The condition that we want to be verified is $\mathbf{N}_B(\varphi_1, 0) = \mathbf{F}(\varphi_1, \varphi_{2,\max})$. Explicitly,

$$\begin{cases} \sqrt{5}v_{B,2}\varphi_1 = \varphi_1 \\ -(\sqrt{5}(v_{B,1}\varphi_1 - 1) + v_{B,3}(\varphi_1^2 - 4)) = -\frac{2(\frac{3\varphi_1^2}{8} - 4)}{\sqrt{5}} \\ v_{B,2}(\varphi_1^2 - 4) = \frac{\varphi_1^2 - 4}{\sqrt{5}} \end{cases}, \tag{5.51}$$

where clearly from the first and last equations $v_{B,2} = \frac{1}{\sqrt{5}}$. Rearranging the second one

$$v_{B,3} = \frac{3}{4\sqrt{5}} - v_{B,1}\frac{20\varphi_1}{(-4 + \varphi_1^2)(4\sqrt{5})}, \tag{5.52}$$

we see that the only possibility is $v_{B,1} = 0$ as we assumed the vertices to be independent on φ_1. As expected, the vertex $\mathbf{v}_B = (0, \frac{1}{\sqrt{5}}, \frac{3}{4\sqrt{5}})^T$ and, when rotated back to the original coordinate frame, we recover the bottom vertex $\mathbf{v}_B = (0, \frac{1}{2}, -\frac{1}{4})^T$.

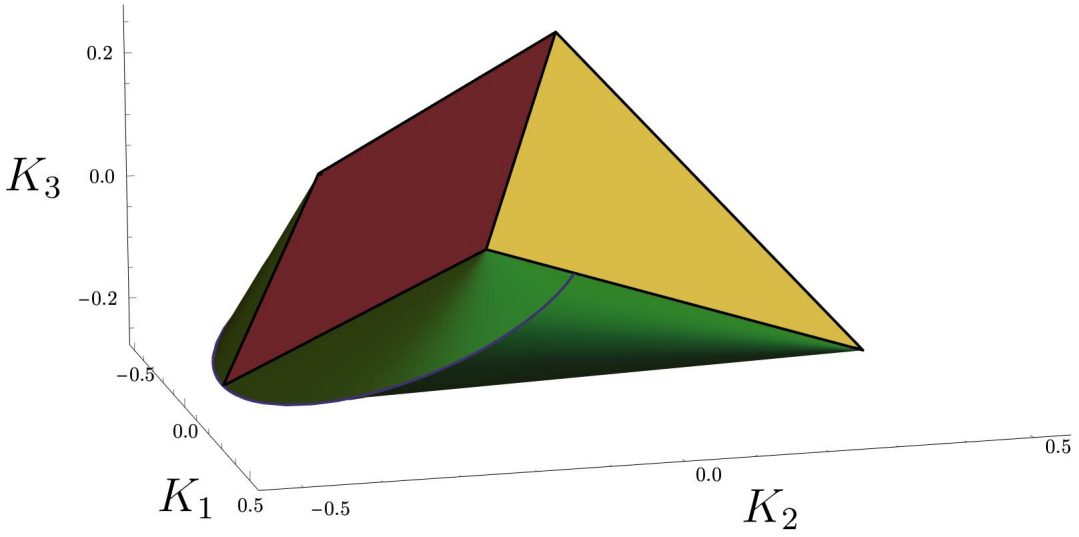

FIGURE 5.8: Graphical representation of D_∞. From this point of view for ferromagnetic K_3 we see the yellow and red faces, the bifurcation surface to the ferromagnetic phase and the striped phase respectively. Behind the polytope, symmetric the yellow face the bifurcation surface to the Neel ordered phase. At the intersection of the red and yellow faces at $K_3 = 0$ lies the vertex $\mathbf{v}_R$ from where the cone $\mathbf{C}_R$ opens. On the left of the figure we also see a glimpse of $\mathbf{C}_L$. The two cones meet at the central point of the seam $\mathbf{S}$, here colored in blue. Under the seam, also colored in green we finally see the cone $\mathbf{C}_B$, opening from $\mathbf{v}_B$.

We proceed similarly for the vertices $\mathbf{v}_L$ and $\mathbf{v}_R$. As before we set the equation $\mathbf{N}_{L,R}(\varphi_1, 0) = \mathbf{F}(\varphi_1, \varphi_{2_{\min}})$, explicitly

$$\begin{cases} \sqrt{5}v_{L,R,2}\varphi_1 = 4\sqrt{5}v_{L,R,2}\varphi_1 + \varphi_1 \\ -(\sqrt{5}(v_{L,R,2}\varphi_1 - 1) + v_{L,R,2}(\varphi_1^2 - 4)) = -4(\sqrt{5}(v_{L,R,2}\varphi_1 - 1) + v_{L,R,2}(\varphi_1^2 - 4)) - \frac{2(|\varphi_1|-3)(|\varphi_1|-2)}{\sqrt{5}} \\ v_{L,R,2}(\varphi_1^2 - 4) = 4v_{L,R,2}(\varphi_1^2 - 4) + \frac{\varphi_1^2-4}{\sqrt{5}} \end{cases}. \tag{5.53}$$

From the first and last equations we find $v_{L,2} = v_{R,2} = -\frac{1}{4\sqrt{5}}$. While we can rearrange the second one as

$$10v_1\varphi_1 = -5|\varphi_1| + (\varphi_1^2 - 4)(1 + 2\sqrt{5}v_{L,R,3}), \tag{5.54}$$

where the second term vanishes only for $v_{3,L} = v_{3,R} = -\frac{1}{2\sqrt{5}}$, so that the the first coordinate finally reads $v_{1,L} = v_{1,R} = -\frac{\text{sign}(\varphi_1)}{2}$. Rotating back to the physical frame the two vertices read $\mathbf{v}_L = (-\frac{1}{2}, -\frac{1}{4}, 0)^T$ and $\mathbf{v}_R = (\frac{1}{2}, -\frac{1}{4}, 0)^T$, which as before exactly recover the vertices, first introduced in Sec.5.3.

5.9.3 The Boundary in the Thermodynamic Limit

We can now give a full analytical characterization of the disorder region of stability, shown in Fig.5.8

$$\partial D_\infty = \begin{cases} \text{conv}\{\mathbf{v}_T, \mathbf{v}_R, \mathbf{v}_B\} \subset 4K_1 + 4K_2 + 4K_3 = 1 \\ \text{conv}\{\mathbf{v}_T, \mathbf{v}_L, \mathbf{v}_B\} \subset -4K_1 + 4K_2 + 4K_3 = 1 \\ \text{conv}\{\mathbf{v}_T, \mathbf{v}_R, \mathbf{v}_L, \mathbf{v}_F\} \subset -4K_2 + 4K_3 = 1 \\ \mathbf{K} = \mathbf{S}(\mathfrak{q}, \mathfrak{q}) + t(\mathbf{S}(\mathfrak{q}, \mathfrak{q}) - \mathbf{v}_B), & \mathfrak{q} \in [0, \pi], \quad t \in [0, 1] \\ \mathbf{K} = \mathbf{S}(\mathfrak{q}, 0) + t(\mathbf{S}(\mathfrak{q}, 0) - \mathbf{v}_R), & \mathfrak{q} \in [0, \pi], \quad t \in [0, 1] \\ \mathbf{K} = \mathbf{S}(\pi, \mathfrak{q}) + t(\mathbf{S}(\pi, \mathfrak{q}) - \mathbf{v}_L), & \mathfrak{q} \in [0, \pi], \quad t \in [0, 1] \end{cases}, \tag{5.55}$$

where by $\text{conv}\{\dots, \mathbf{v}_i, \dots\}$, we denote the convex polygon bounded by the vertices within the brackets.

It consists of six surfaces only, the first three terms are polygons binding the upper part, the last three terms are the three cones binding the lower part. For ferromagnetic K_3 we proved in Sec.5.5 that the disorder region is bounded by three planes only and exactly match D_2, whose tip $\mathbf{v}_T = (0, 0, \frac{1}{4})^T$ we introduced in Sec.5.3. For any even $N \geq 4$, the ferromagnetic and anti-ferromagnetic faces are quadrangolar, while the striped face is a pentagon. In the limit for $N \to \infty$ all three faces lose an edge in the region $K_3 < 0$: the two lower edges of the (anti-)ferromagnetic face align on the edge that connects the back vertex $\mathbf{v}_B = (0, \frac{1}{2}, -\frac{1}{4})^T$ to the right(left) vertex $\mathbf{v}_R = (\frac{1}{2}, -\frac{1}{4}, 0)^T (\mathbf{v}_L = (-\frac{1}{2}, -\frac{1}{4}, 0)^T)$; the front edge of the striped face (introduced in Sec.5.4.2), in this limit, converges to a single vertex $\mathbf{v}_F = (0, -\frac{1}{2}, -\frac{1}{4})^T$. In the previous section we derived the analytical equations of the three cones binding the bottom of the region. It suffices to remember that each of the three cones opens from one of the three pairwise intersections of the upper polygons and has the basis lying on the seam. The left cone apex is $\mathbf{v}_L$, its basis is the arc of the seam going from the point $S(0, 0)$, lying on the bottom edge of the ferromagnetic face, to $S(\pi, 0) \equiv \mathbf{v}_F$. Symmetric to it with respect to K_1, the right cone basis is the seam arc going from $\mathbf{v}_F$ to $S(\pi, \pi)$. While the bottom cone opens from the vertex $\mathbf{v}_B$ and its basis exactly matches the seam in its full width.

5.10 Summary

For finite N the polyhedra are bounded whenever $N \geq 4$. The relative position of a mode on the SRBZ plays an important role. The top of the polytope is always given by three modes only, those at the corner of $\widehat{\mathfrak{U}}_N$. The bottom of the polytopes is predominantly dominated by the modes on the border of the SRBZ that organizes in three fans opening from the three multicritical vertices. For even N the borders exactly matches the modes with an orbit size of 4. The bulk of the modes has orbit size 8 and always appear clustered in small facets all tangent to a single curve $S(\mathfrak{q})$. In the limit $N \to \infty$ the fans converge to cones and the multitude of small facets converge to single points lying exactly on the seam.

The rest of the thesis is dedicated to numerically assess the validity of the predictions for the possible order-disorder transitions that follow from the polytopes at fixed N.

Chapter 6

Simulations

We aim to numerically test the degree of accuracy of the physics encoded in the polytopes predicted by Mean Field Theory. Our major purpose is to inspect whether the dominant mode bifurcates from the disorder solution along the radial direction of the faces predicted by our theory. To meet our goal, the simple choice of a spin flip Metropolis algorithm, as we will argue, is well suited: we are not interested in low temperature or critical phenomena, rather in observing the onset of a phase.

We will also empirically address the physics beyond the (first) bifurcation surface. First, we test the precision of the predicted critical temperature. Our expectation is that mean field theory systematically overestimates (underestimates) the critical temperature (inverse temperature). Second, we look for mode coexistence: our theory only predicts what the dominant mode is, while a phase might be fully defined by the superposition of a set of concurring modulations. We further discuss this topic in the outlook (Sec.7.2). Finally, we hint at the presence of subsequent phase transitions beyond the predicted bifurcation surfaces. Long range lattice models, as argued in the introduction (Sec.1.1), may exploit multiple phase transitions up to the emergence of a full devil's staircase of infinite modulated phases, that has been observed e.g. in the ANNNI model. Considering only lattices constrained by PBC, we expect that only a subset of modulations compatible with the lattice structure may emerge. Thus, Periodic Boundary Conditions may also constrain the hypothetical devil's staircase to a finite number of phase transitions. To shed light on this subtle hierarchy of transitions we will compare simulations on the same dominant mode but on lattices of increasing commensurate sizes.

We stress that the interpretation of some results is ambiguous, in such cases, we will only describe what we see rather than provide explanations.

In Sec.6.1, we review the basic workings of the Metropolis algorithm and its specific usage in the present context. The observables of interest to fulfill the scopes described above are introduced in Sec.6.2. Finally, the results are presented in Sec.6.3.

6.1 Metropolis

A many body system is fully understood when the probability distribution of Eq.4.1 is known . The average of an observable at fixed temperature could then be computed as a sum over uniformly sampled configurations weighted by the probability. However,

on an Ising model with M sites, there are 2^M configurations and a full enumeration is generally unfeasible.

The Metropolis algorithm[76] circumvents the above issues considering only configurations according to their probability weight, technique called *importance sampling*. The idea of stochastic sampling dates back to early 19th century to an intuition by Laplace. However, without the development of computers, the method was impracticable. The turning point came in 1940 with America entering the second world war and the consequent funding to the development of the computer ENIAC to simulate neutron diffusion in nuclear bombs. Nonetheless, the project, supervised by the Greek physicist Nick Metropolis was not completed until 1947. The Metropolis algorithm is nowadays widely used and many instructive manuals are available[77]. Given an arbitrary initial configuration C_0, the essential idea is to generate a Markov Chain of configurations proposing a small change in the previous step that can be either accepted or rejected. The procedure is effective whenever the system is *ergodic* and the Markov Chain respects *detailed balance*. Ergodicity is the requirement that given any two configurations X and Y, there is a non zero transition probability $W(X \to Y)$ from one to the other. Detailed balance is the very core of the algorithm and gives the practical rule to accept or reject a move. The derivation is easy and brief to sketch. The starting point is the master equation of the Markov Chain

$$\frac{dP_X}{dt} = \sum_{X \neq Y} [P_Y(t)W(Y \to X) - P_X(t)W(X \to Y)], \tag{6.1}$$

where $P_X(t)$ is the probability of a configuration at time t, which we will assume to be time independent and to coincide with the Boltzmann weight. For a stationary process ($\frac{dP_X}{dt} = 0$) the master equation immediately reduces to the condition known as detailed balance

$$P_Y W(Y \to X) = P_X W(X \to Y), \tag{6.2}$$

where we dropped the time dependence. The above equation can be further decomposed factorizing the transition probability in a trial and an acceptance probability $W(X \to Y) = T(X \to Y)A(X \to Y)$, substituting above

$$P_Y T(X \to Y)A(X \to Y) = P_X T(Y \to X)A(Y \to X), \tag{6.3}$$

where, noticing that the probabilities are known (and are given by the Boltzmann weight of Eq.4.1) and that one of the two acceptance probability can be arbitrarily set to 1, all the effort is devoted in finding the appropriate trial move such that it can be mathematically modelled, as well as, well performs for the given purposes. For our current purposes, we will use a spin flip move, the trial probability is $T(X \to Y) = \frac{1}{M}$, with M the number of sites in the system. Inverting the equation above, the final acceptance (rejection) rule for the system under investigation becomes

$$A(X \to Y) = \min\{1, e^{-\beta(E_X - E_Y)}\}, \tag{6.4}$$

which can be easily implemented.

6.1.1 Usage

The most important quantity when dealing with Monte Carlo simulations is the *correlation time* among successive configurations. The use of a Markov Chain intrinsically generates subsequent correlated configurations, such that, the hypothesis of the central limit theorem are not verified. Thus, to take averages one has to wait for the configurations to decorrelate. To this end, one should in principle take one measurement every correlation time[1], heavily reducing the number of measurements. A common technique that circumvents the issue and yields more solid measurements is block averaging. Instead of taking one measurement per correlation time, one measures the observables at all steps and eventually divides the measurements in blocks of size greater than correlation times. The final results are then calculated as averages of block averages. This procedure is of further practical advantage. It allows to use only rough estimates of the correlation time without affecting the number of measurements taken.

The correlation time strictly depends on the temperature regime and the move implemented, our choice of the simple spin flip move yields low correlation times at high temperature and far from criticality. It is the perfect choice as we are not interested in low temperature physics, neither in accurate measurements at criticality.

The Metropolis algorithm consists in some infrastructure wrapped around the acceptance rule: first, one initialize the system and waits for it to equilibrate[2]; next, a double loop over the number of blocks and the number of Monte Carlo steps per block encloses the trial move and its acceptance/rejection rule. At each step the observables of interest are measured and are averaged at the end of each block. Finally, at the very end, one takes the final averages over the block averages.

Typically, the Metropolis algorithm usage consists in simulating the Hamiltonian at different temperatures in a desired interval. We are interested in assessing the emergence of a mode beyond a face of the polytopes. To this end, we ran Monte Carlo simulations along straight rays in reduced coupling parameter space (introduced in Sec.4.2), starting from the infinite temperature point, (the origin of parameter space) and running through the centroid of each predicted face. There is some freedom in fixing the scale of the coupling parameters. The natural choice is to take the values at the centroid of a face, thus using inverse temperature units, This choice has the advantage of a simpler comparison with the predicted critical temperature which is always $T_c = 1$, and the disadvantage that it does not allow to directly compare the critical temperature for different faces.

Finally, we make an important remark. Usually, finite size can dramatically affect results of the simulations, especially at criticality. Phase transitions are defined in the thermodynamic limit and the finite size simulations introduce systematic errors in the measurement of the observables which are hard to take into account, e.g., the smaller the size, the lower the "divergence" peak of the susceptibilities and the more slightly shifted to the left(right). The most simple way to circumvent the problem is to increase the system size to the limit of the computational resources available. On

[1] It is a rule of thumb: usually it is suggested to wait one or two correlation times.

[2] Starting with a random configuration, one typically waits two or three correlation times for the system to equilibrate.

the contrary, our interest lies in simulating systems at specific finite sizes. We are interested in testing whether we have the correct predictions on the finite lattices L_N in periodic boundary conditions, where only a limited number of phases emerges due to the arguments presented in Sec.2.3.1. Thus, finite size systems are advantageous for our scope: we focus in detecting the sole modes compatible with the underlying lattice structure, where finite size effects are intrinsically present.

6.2 Observables

For the purpose of detecting the dominant modes beyond a bifurcation surface, we are only going to take into account four observable quantities. We measured the energy, the order parameters and their susceptibilities. The simplest indicators of a phase transition are the average energy $E = \langle H \rangle$, measured directly form the definition of Hamiltonian of Eq.2.3 and its fluctuation, the specific heat

$$C_V \equiv \frac{\partial E}{\partial T} = \frac{\Delta E^2}{k_b T} = \frac{\langle E^2 \rangle - \langle E \rangle^2}{k_b T^2}, \tag{6.5}$$

which can be directly computed taking the square of the energy. The specific heat is expected to peak at a phase transition but does not directly provide information on the specific phase. To tell phases apart, we measured the order parameter of Eq.2.17

$$\mu_{\mathbf{q}} \equiv \frac{1}{|\mathfrak{D}_4|} \sum_{g \in \mathfrak{D}_4} m^*_{g\mathbf{q}} m_{g\mathbf{q}}, \tag{6.6}$$

where we remember that $\mathfrak{D}_4$ is the dihedral group of order four (Sec.2.2) and $g \in \mathfrak{D}_4$. Per each simulated lattice size there are a number of order parameters equal to the size of the respective SRBZ. The expectation is that, beyond each face of the polytope, only the dominant predicted mode emerges. A stronger[why] indication of the occurrence of a phase transition is given by the order parameter susceptibility per spin

$$\chi_q = \frac{\partial \mu_q}{\partial T} = \frac{\Delta \mu_q^2}{k_b T} = \frac{\langle \mu_q^2 \rangle - \langle \mu_q \rangle^2}{k_b T}. \tag{6.7}$$

For the practical purpose of evaluating the performance and the reliability of the algorithm, we measured the correlation time. Its estimate has been performed taking the suggestions of Barkema[77]: first, calculating the integral of the auto-correlation function $a(t)$ of an observable

$$a(t) \sim e^{-\frac{t}{\tau}}, \tag{6.8}$$

where τ is the correlation time; next, taking as estimate for τ the numerical integral of the above equation

$$\int_0^\infty \frac{a(t)}{a(0)} = \int_0^\infty e^{-\frac{t}{\tau}} = \tau. \tag{6.9}$$

The bottleneck of the calculation lies in the numerical measurement of $a(t)$. If we suppose to begin the measurement at $t = t'$ and to let it run for t_{max} steps, the

auto-correlation function $\xi_{\mathfrak{q}}$ for each of the order parameters is given by

$$\xi_{\mathfrak{q}} = \frac{1}{t_{max}-t}\sum_{t'=0}^{t_{max}-t}\mu_{\mathfrak{q}}(t')\mu_{\mathfrak{q}}(t+t') - \frac{1}{t_{max}-t}\sum_{t'=0}^{t_{max}-t}\mu_{\mathfrak{q}}(t')\left(\frac{1}{t_{max}-t}\sum_{t'=0}^{t_{max}-t}\mu_{\mathfrak{q}}(t+t')\right), \tag{6.10}$$

so that the integral of Eq.6.9 trivially follows as a sum of all the discrete values.

The above procedure is a computationally intensive measurement both in time and memory: it requires to store all the measurements and the computation time scales quadratically with the number of steps. Moreover, one does not know beforehand the correlation time.

6.3 Results

The code has been implemented in C++ and optimized with the aid of the time profiler available in the *Xcode* suite. The energy calculation has been optimized measuring the energy difference of the flipped spin neighbourhood only, to further speed up the calculation of the order parameters the cosines of the compatible modes have been tabulated. The bottleneck of the computation is the measurement of the order parameters, even with a full tabulation of the cosines involved. It requires a loop over the whole lattice per each compatible mode. Furthermore, it scales quadratically both with the linear size N of the lattice considered and the number of modes to account for.

The simulations were performed on the cluster *Hollandia* at Amolf. It consist of 40 *Intel Xeon E5-2697 v4 CPUs* where temperature sampling where run in parallel. The correlation time measurement makes exception, it is a linear and heavy calculation, more conveniently performed on the other available *Dual-Core Intel Core i5* processor.

We will begin presenting the simulations on L_4 as an introductory example to the trends and the visualization of the result. Increasing the size of the lattice we will subsequently show the simulations on L_6, where we first witness mode coexistence. The smallest lattice that clearly exhibits the phenomenon of subsequent phase transitions is L_8. Finally, to compare lattices with commensurate phases we will compare the simulations on L_4 and L_6 with those on L_{12}.

For the simulations on the lattices L_4, L_6 and L_8, we the took a uniform temperature sampling of 40 temperature points equi-spaced in the range from $T = 1$ to $T = 3$ and 45 temperature points equi-spaced in the range $T = 0.1$ to $T = 1$. While on L_{12}, we refined the precision to $\Delta T = 0.01$ in the interval $T = 0.1$ to $T = 0.5$. For each simulation we set a fixed number of blocks to $N_{\text{BLOCKS}} = 100$, and varied the number of steps per blocks according to the measured correlation time. Therefore, the total number of MC steps $N_{\text{BLOCKS}} = 100$ for each simulation is computed as $N_{\text{TOTAL}} = N_{\text{BLOCKS}} N_{\text{STEPS}}$. The correlation time with respect to which we set N_{STEPS}, has been taken as the maximum among the energy correlation time and the order parameter correlation time, one per each compatible mode. We systematically observed (and it stands to reason) that the highest correlation times are those of the emergent modes and the energy. On L_4 we measured a correlation time of 16000

steps at $T = 0.1$ that already decreases under 100 steps at $T = 0.4$. Similarly, on L_6 we measured a correlation time of 33000 steps at $T = 0.1$ that also goes under 100 at $T = 0.4$. The measurement of the correlation time on L_8 and L_{12} was not successful at low temperature: the minimum correlation time measurement on L_8 was of 33000 steps at $T = 0.12$, while at $T = 0.1$ we attempted the measurement up to 300000 steps, but without observing any decorrelation. A similar issue has been encountered on L_{12}, where we found as lower bound for the correlation time at $T = 0.11$ 500000 steps, while at $T = 0.12$ we measured a correlation time of 33000 steps as for L_8. As before, the correlation time on both L_8 and L_{12} decrease to few hundreds above $T = 0.4$. According to the correlation time measurement and to produce solid measurement we have almost always set a number of steps per blocks way above the canonical choice of three times the correlation time. For the simulations on L_4 and L_6 we set N_{STEPS} to 500000 up to $T = 0.2$, to 100000 up to $T = 0.4$ and to 10000 for higher temperatures. On L_8 and L_{12} we also set N_{STEPS} to 10000 for $T > 0.4$, while for lower temperatures we set N_{STEPS} to $2\ 10^5$ for $0.2 < T \leq 0.4$ and to 10^6 for $T \leq 0.2$. These include the above mentioned temperatures whose correlation time measurement was not successful.

Each size simulated consists of multiple plots, each providing interesting insights on the physics going on. Among the variety of the measurements performed, per each size simulated we will show all the order parameters per each bifurcation surface. To give an intuitive representation of the emergence of the predicted dominant mode, the plots are organized to mimic the geometry of the Symmetry Reduced Brillouin Zone. The greater the size, the more various the behaviour of the phases. To address this diversity we will further show the energy, specific heat and susceptibility of the phases that, case by case, are deemed more interesting. Moreover, to compare with the theoretical prediction, in all the plots a dashed pink line stresses the theoretical critical temperature. In the more interesting cases, the phase transition happens roughly around $T = 0.25$, thus, to emphasize the low temperature physics we show the plots in units of β, as it dilates the more interesting low temperature phenomena.

6.3.1 L_4

The SRBZ $\mathfrak{U}_4$ has six elements, the corresponding simulations are shown in Fig.6.1. Each of the six simulations on this lattice behave exactly as expected. Beyond the centroid of each face, only the predicted dominant mode emerges. All the other modes completely vanish beyond the phase transition. We remember that the corresponding ground states are known and have already been reported in Fig.2.3. The plots only differ in the steepness of the curves[3]. The three modes in the corners behave roughly similarly, while the double checkerboard phase begins arising for slightly lower β. This is true also for the staggered dimer and double striped phases, although their curves reach a steady value of the order parameter at a higher β. Furthermore, we notice a remarkable feature that we will also find on all the other lattices: the plots reflect the symmetry of the SRBZ with respect to the anti-diagonal, retaining the K_1 symmetry of the polytopes treated in Sec.5.4.1. More specifically, the plots of $\mathfrak{q} = (0, 0)$ and $\mathfrak{q} = (\pi, \pi)$ as well as the pair $\mathfrak{q} = (0, \frac{\pi}{2})$ and $\mathfrak{q} = (\pi, \frac{\pi}{2})$ are exactly equal, also in the vanishing trend of the other modes.

[3]This is emphasized by the susceptibility plots which we do not show here.

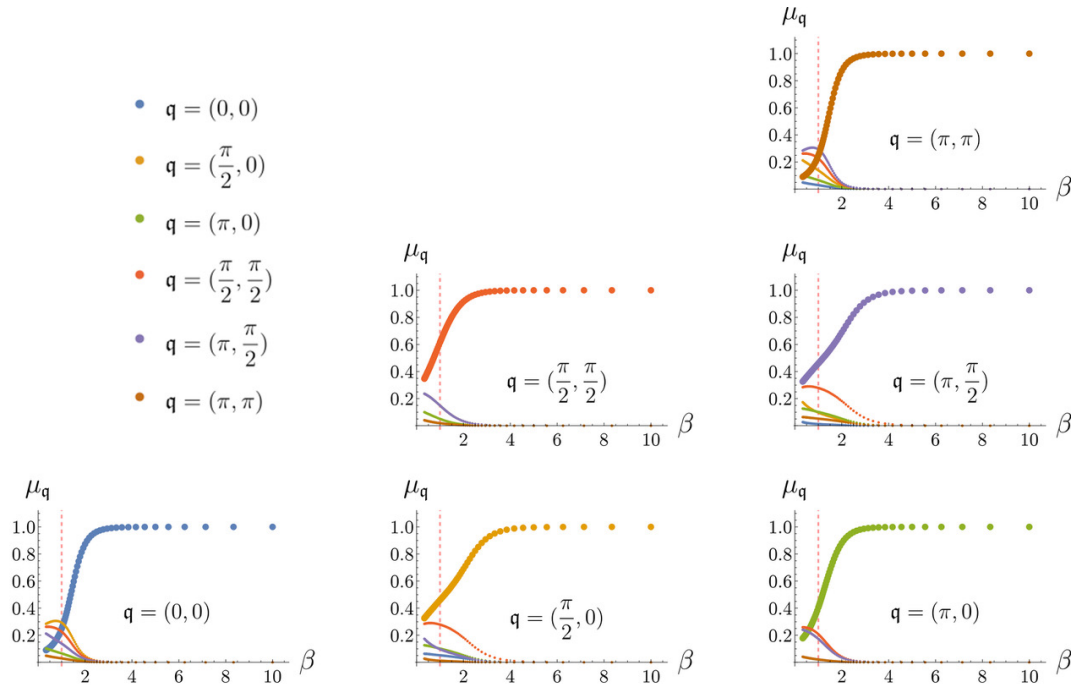

FIGURE 6.1: Order parameters of the six phases compatible with lattice L_4. The plots are organized to mirror the geometry of the SRBZ $\mathfrak{U}_4$. Beyond each bifurcation surface the sole mode emerging is the predicted mode.

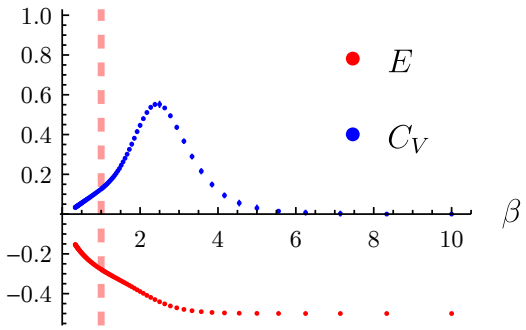

(A) Energy (red) and heat capacity (blue).

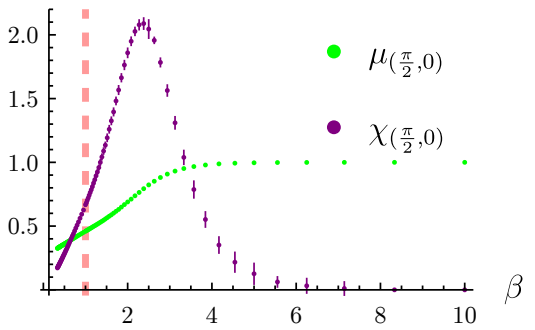

(B) Order parameter (green) and susceptibility (purple). The trend of the presented observables perfectly mimic the classic behaviour of a nearest neighbour Ising model.

FIGURE 6.2: Simulation details of the phase $\mathfrak{q} = (\pi, \frac{\pi}{2})$ on the lattice L_4.

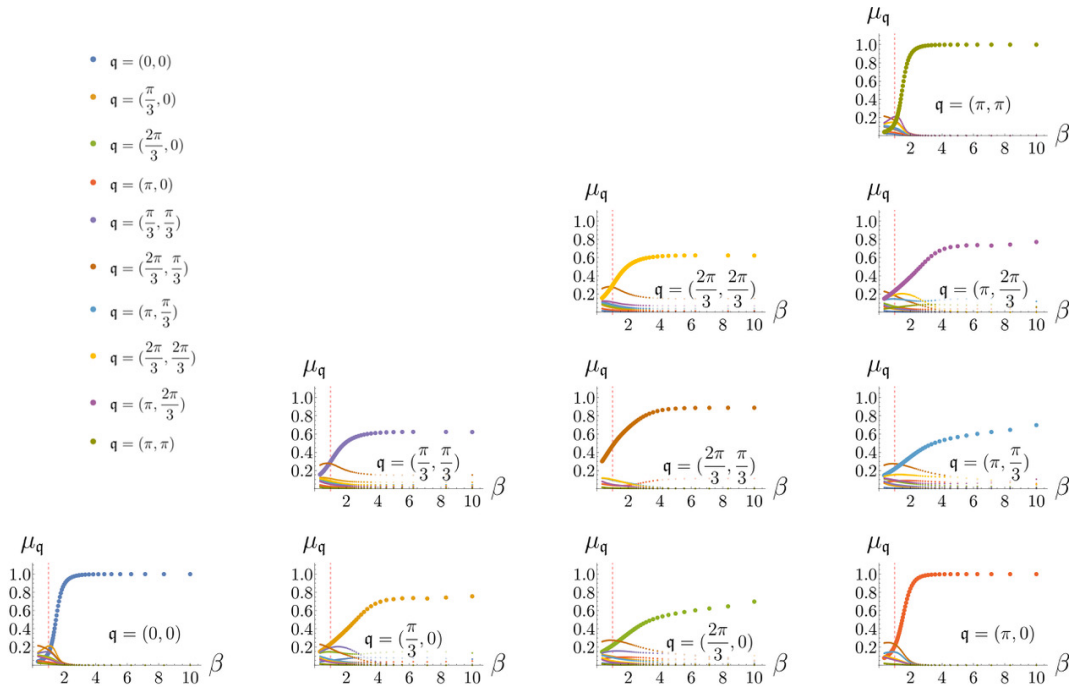

FIGURE 6.3: Order parameters of the ten phases compatible with lattice L_6. The plots are organized to mirror the geometry of the SRBZ $\mathfrak{U}_6$. Beyond each bifurcation surface we observe different behaviours. The corners are well behaved, while all other modes hint at coexistence.

Finally, in Fig.6.2 we show the details of the simulation of the staggered dimer phase. An uncommon but well behaved phase that we will use as a term of comparison for further simulations. All plots are shown with their standard deviation, the error bar is often smaller than the marker. On the left, in Fig.6.2a we show the energy E and the heat capacity C_V. On the right plot, in Fig.6.2b, we show the order parameter $\mu_{(\pi,\frac{\pi}{2})}$ and its susceptibility $\chi_{(\pi,\frac{\pi}{2})}$. The energy reaches a minimum value of 0.5. On both plots, the peaks of the correlation function signals a phase transition at roughly $\beta \sim 2$. The low height of the peaks is due to size effects on the very small 4×4 lattice.

6.3.2 L_6

More interesting behaviours are observed beyond the ten faces of D_6. In Fig.6.3 we show the plots of the order parameters, organized as the respective SRBZ. As before, it clearly stands out that the expected dominant mode emerges beyond each face.

The three corner modes, also shared by $\mathfrak{U}_4$, behave exactly as before: only the dominant mode arises, while all the other modes completely vanish. Beyond all the other seven faces we clearly see mode coexistence. The dominant mode takes over without reaching the value of 1, while a very small component of each of the other modes survives until low temperature but in a flat trend.

The symmetry of the plots with respect to the anti-diagonal implies that we can restrict our attention to four plots only. To this regard, we notice that the behaviour of a phase does not strictly depend on the parity of the complexity of a mode. The modes with complexity (we have defined the complexity in Sec.3.1.1) $C(\mathfrak{q}) = 3$, $\mathfrak{q} = (\frac{2\pi}{3}, \frac{2\pi}{3})$

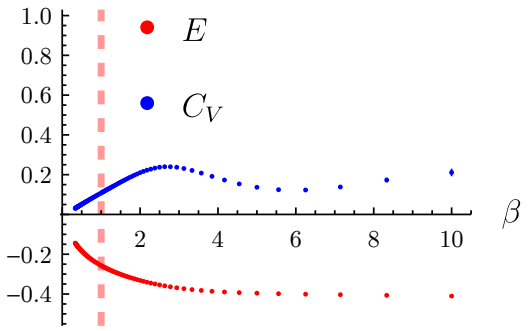

(A) Energy and specific heat. The specific heat weirdly grows at low temperature.

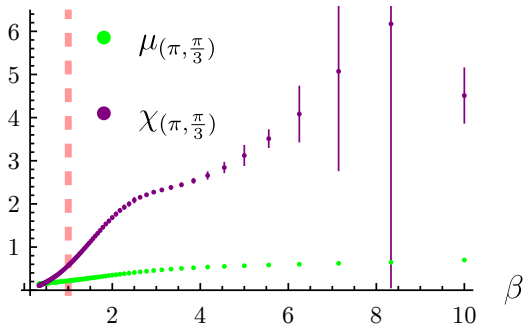

(B) Order parameter and susceptibility. The order parameter grows very slowly. The susceptibility has a double bump, the second one followed by high fluctuations.

FIGURE 6.4: Simulation details of the mode $\mathfrak{q} = (\pi, \frac{\pi}{3})$.

and $\mathfrak{q} = (\frac{2\pi}{3}, 0)$, are symmetric to modes with complexity $C(\mathfrak{q}) = 6$ but behave exactly in the same manner. Thus, parity is not a good indicator of the underlying physics.

To further understand the details of the mentioned behaviour, in Figs.6.4 and 6.5 we compare the transitions toward the phases $\mathfrak{q} = (\frac{2\pi}{3}, \frac{2\pi}{3})$ (equivalently $\mathfrak{q} = (\frac{\pi}{3}, \frac{\pi}{3})$) and $\mathfrak{q} = (\pi, \frac{\pi}{3})$ (equivalently $\mathfrak{q} = (\frac{2\pi}{3}, 0)$. The reason of this choice is that $\mathfrak{q} = (\frac{2\pi}{3}, \frac{\pi}{3})$ is rather well behaved, while $\mathfrak{q} = (\frac{\pi}{3}, 0)$ (and $\mathfrak{q} = (\pi, \frac{2\pi}{3})$) behave similarly[4] to $\mathfrak{q} = (\frac{2\pi}{3}, 0)$.

The mode $\mathfrak{q} = (\pi, \frac{\pi}{3})$ is symmetric to $\mathfrak{q} = (0, \frac{2\pi}{3})$. The energy and C_V are shown in Fig.6.4a. We notice two things, first and most important the C_V appears to slightly grow again beyond the first peak, which might be indicative of a subsequent phase transition. Second we notice that the energy, compared to Fig.6.2a, decreases very slowly and without any inflection points. A very similar thing occurs for, respectively, the susceptibility and the order parameter, shown in Fig.6.4b. The order parameter grows very slowly up to a maximum value lower than 1. While the susceptibility has an unexpected behaviour, coherently with the signal in the C_V, it also has a double bump. Furthermore, it also shows very wide low temperature fluctuations. This behaviour is compatible with frustration, where there is no long range order and both the specific heat and the susceptibility do not have a divergence point[29]. However, we cannot exclude a heavy influence of finite size effects.

The plots of Figs.6.5a and 6.5b are indicative of a phase transition toward $\mathfrak{q} = (\frac{2\pi}{3}, \frac{2\pi}{3})$ (equivalently $\mathfrak{q} = (\frac{\pi}{3}, \frac{\pi}{3})$). The energy has a behaviour similar to the previous one, however, the specific heat vanishes for high β without any hint to subsequent phase transitions. The order parameter slowly grows up to a maximum value lower than one. The surprising behaviour comes from the susceptibility, after the first peak it goes down to reach a maximum value higher than the first peak at $T = 0.1$, with respect to the suceptibility of $\mathfrak{q} = (\pi, \frac{\pi}{3})$, with a very low standard deviation. We will not further comment upon this unexpected behaviour, it is nonetheless worth to point out that it might be explained in terms of the ground states (compare to Sec.7.1).

[4] In Sec.7.1 we will make the first step toward the ground states, which hints at the reason of the similarity.

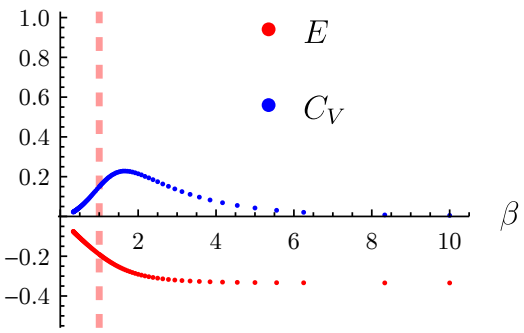

(A) Energy and specific heat. Other than then very low peak, the trend matches the expected behaviour.

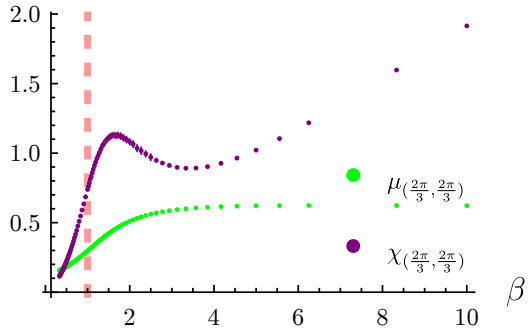

(B) Order parameter and susceptibility. The order parameter is well behaved, while the susceptibility appears to diverge at very high β.

FIGURE 6.5: Simulation details of the mode $\mathfrak{q} = (\frac{2\pi}{3}, \frac{2\pi}{3})$.

6.3.3 L_8

The behaviour of the simulations on L_8 are very diverse and reflect the more interesting features of $\mathfrak{U}_8$ with respect to the previous lattices. It is defined by 15 inequalities, with 9 new modes of complexity 8. Out of these 6 have an orbit size of 4 and three an orbit size 8, with the first appearance of a degenerate face.

In Fig.6.6 is shown the standard mosaic. Once again, our theory always predicted the correct first bifurcation mode, nonetheless the clear presence of subsequent phase transitions requires some more attention to notice. Once again, the modes shared by L_4 behave in exactly the same way. The two non-degenerate modes with an orbit size of 8, $\mathfrak{q} = (\frac{\pi}{2}, \frac{\pi}{4})$ and $\mathfrak{q} = (\frac{3\pi}{4}, \frac{\pi}{2})$, have a very simple behaviour that recalls the behaviour of the mode $\mathfrak{q} = (\frac{2\pi}{3}, \frac{2\pi}{3})$ on L_6, whose details have been previously discussed: the predicted dominant mode arises with only minor contributions from the others. Moreover, the physics beyond the vertex $\mathbf{v}_F$, shows an interesting transition toward a phase defined by three emerging modes. Among the other plots we manifestly recognize roughly two different behaviours: subsequent phase transitions, and mode coexistence.

Subsequent phase transitions are observed beyond all the faces with a complexity $C(\mathfrak{q}) = 8$ and an orbit size 4. We correctly predict the first emerging mode, while the system appears to systematically settle on the ground state of the corner mode next to it. There is a difference however in between the modes on the two catheti $\mathfrak{q} = (\frac{\pi}{4}, 0)$ and $\mathfrak{q} = (\frac{3\pi}{4}, 0)$, where the second phase transition is observed roughly at $\beta < 4$, and the mode on the hypotenuse $\mathfrak{q} = (\frac{\pi}{4}, \frac{\pi}{4})$, where the second phase transition is only hinted at very low temperatures[5].

In Fig.6.7 we investigate the details of the simulation beyond the face defined by $\mathfrak{q} = (\frac{3\pi}{4}, 0)$. The clear double transition observed in the order parameter plot, is only partially confirmed by the susceptibilities shown in Fig.6.7b: the susceptibilities of the modes $\mathfrak{q} = (\pi, 0)$ and $\mathfrak{q} = (\frac{3\pi}{4}, 0)$ appear to peak at the same inverse temperature

[5] As previously stated, the correlation time of the last two points might have been underestimated. However the trend of the corner mode emerging at low temperatures already begins at solid measurements.

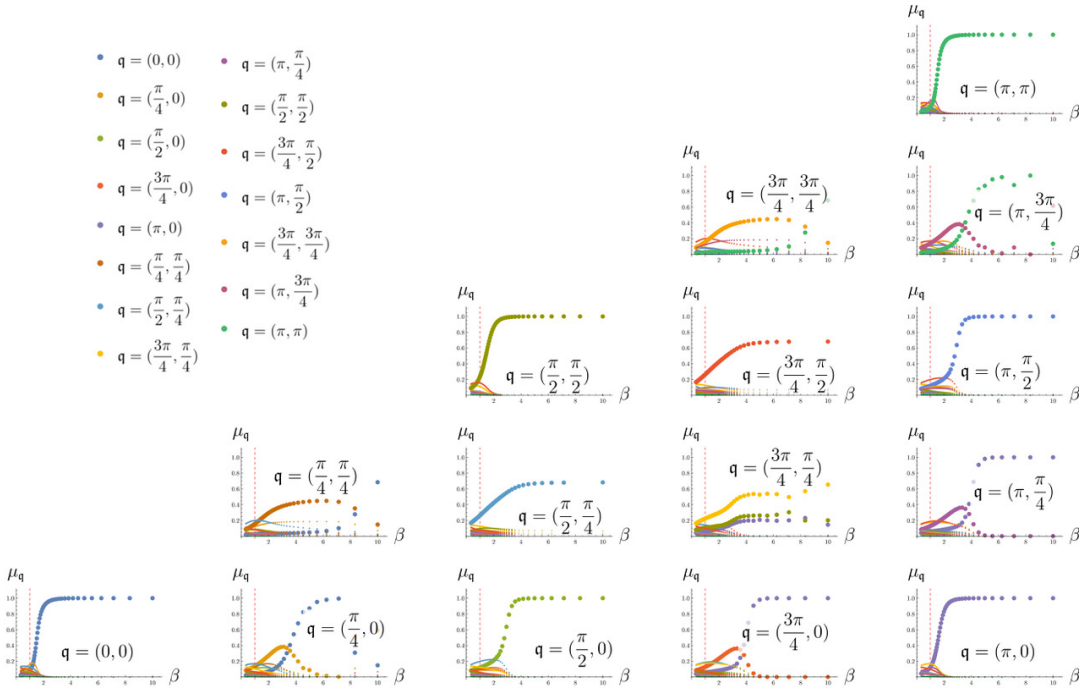

FIGURE 6.6: Order parameters of the fifteen phases compatible with lattice L_8. The plots are organized to mirror the geometry of the SRBZ $\mathfrak{U}_8$. We observe all the aforementioned behaviours beyond the faces: the corners are still well behaved; some modes on the borders clearly show subsequent phase transition; the simulation beyond the front edge shows a transition to a phase clearly defined by mode coexistence.

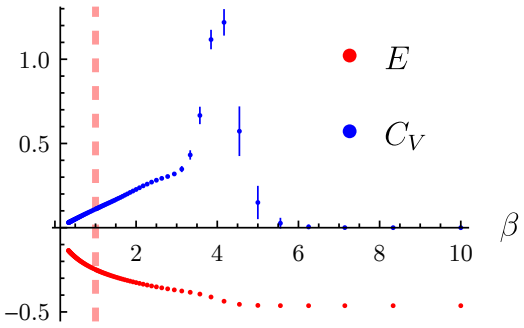

(A) Energy and specific heat. The specific heat clearly peaks around $\beta \sim 4$, nonetheless around $\beta \sim 3$, where the predicted order parameter peaks before vanishing, there is curious abrupt change in the slope. Accordingly, the energy also appear to change inflection around the same temperature.

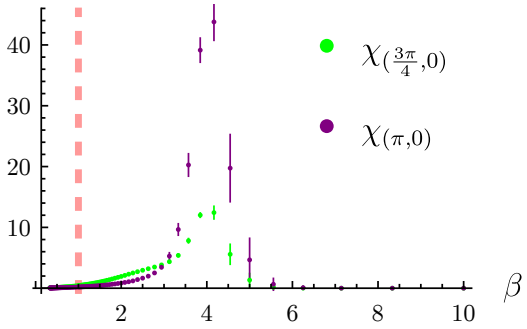

(B) Susceptibilities of the predicted mode $\mathfrak{q} = (\frac{3\pi}{4}, 0)$ and of the subsequent phase $\mathfrak{q} = (\pi, 0)$. Both peak at roughly $\beta = 4$.

FIGURE 6.7: Simulation details of the mode $\mathfrak{q} = (\frac{3\pi}{4}, 0)$.

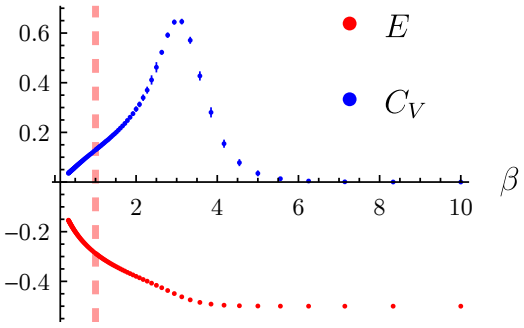

(A) Energy and specific heat of the system. The behaviour is rather clean, the specific heat has a single peak before vanishing.

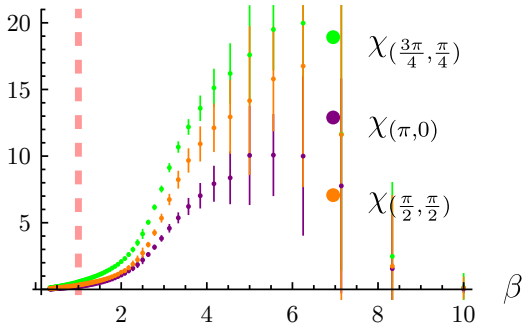

(B) Susceptibilities of the three arising modes: the predicted mode $\mathfrak{q} = (\frac{3\pi}{4}, \frac{\pi}{4})$ and the two other modes on the anti-diagonal, $\mathfrak{q} = (\frac{\pi}{2}, \frac{\pi}{2})$ and $\mathfrak{q} = (\pi, 0)$. All three have a wide and round peak.

FIGURE 6.8: Simulation details of the mode $\mathfrak{q} = (\frac{3\pi}{4}, \frac{\pi}{4})$.

$\beta \sim 4$, the only difference being height. Similarly also the specific heat, shown in Fig.6.7a exploit a single peak. However, the weird and abrupt change in its slope at roughly $\beta = 3$ might be indicative of a behaviour observed in the order parameter.

Finally, in Fig.6.8, we show the simulation observables across the midpoint of the front edge, $\mathbf{v}_F = (0, -\frac{1}{2}, -\frac{1}{4})^T$, where the inequality defined by $\mathfrak{q} = (\frac{3\pi}{4}, \frac{\pi}{2})$ is only tangent. In this case mode coexistence differs from that observed on the modes of L_6: rather than a minor background coexistence, in this situation we have three modes that prominently emerge, fully concurring to the overall phase. The order parameter of the predicted mode $\mathfrak{q} = (\frac{3\pi}{4}, \frac{\pi}{2})$ dominates, but closely followed by the two other modes on the anti-diagonal $\mathfrak{q} = (\frac{\pi}{2}, \frac{\pi}{2})$ and $\mathfrak{q} = (\pi, 0)$. Accordingly, the specific heat of Fig.6.8a exploits a single peak before vanishing, while the susceptibilities of the three coexisting modes, shown in Fig.6.8b, simultaneously peak in very wide and round fashion.

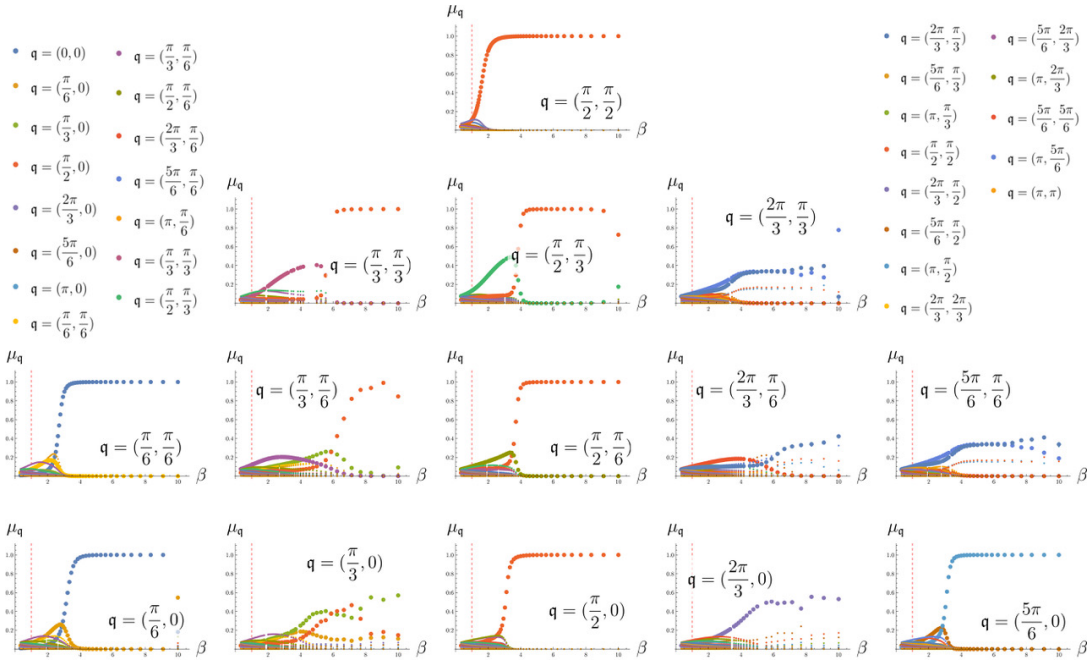

FIGURE 6.9: Order parameters of the 14 out of the 28 phases compatible with lattice L_{12}. We are omitting the upper triangular half of the SRBZ due to symmetry reason and the corner modes. The new most interesting behaviour is observed on $\mathfrak{q} = (\frac{\pi}{3}, \frac{\pi}{3})$ that now has a subsequent transition to a double checkerboard state. Furthermore, intricate and interesting behaviour is observed beyond the faces defined by $\mathfrak{q} = (\frac{\pi}{3}, \frac{\pi}{6})$ and $\mathfrak{q} = (\frac{\pi}{3}, 0)$.

6.3.4 L_{12}

Lastly, we investigate the phase transitions beyond the faces of D_{12}. The size of its SRBZ, $\widehat{\mathfrak{U}}_{12}$, that amounts to 28 modes, makes it prohibitive to show the plot of all the order parameters as we did for the previous lattices. Thus, accounting on the now established mirror symmetry, in Fig.6.9, we only show the lower half of the plots. To further improve the overall visualization, we chose to not show the corner modes $\mathfrak{q} = (0, 0)$ and $\mathfrak{q} = (\pi, 0)$, as once again, their behaviour resembles the one shown in the previous plots. Thus, out of all the 28 modes we show only 14.

The behaviour of the faces with complexity $C(\mathfrak{q}) = 4$ do not change with size; more interestingly, those shared with $\widehat{\mathfrak{U}}_6$ exploit an interesting twist, when compared to Fig.6.3: $\mathfrak{q} = (\frac{\pi}{3}, \frac{\pi}{3})$ now exhibit a subsequent phase transition to the phase $\mathfrak{q} = (\frac{\pi}{2}, \frac{\pi}{2})$ in the same spirit of the modes on the catheti of $\widehat{\mathfrak{U}}_8$. The other three modes shared with $\widehat{\mathfrak{U}}_6$, are also influenced by the presence of modulations of size four, that now contributes to the final phase, lowering the overall contribution of the dominant mode but always from the background.

Among the 9 new phases of complexity $C(\mathfrak{q}) = 12$ we recognize previous behaviours, the modes $\mathfrak{q} = (\frac{\pi}{6}, 0)$, $\mathfrak{q} = (\frac{5\pi}{6}, 0)$, $\mathfrak{q} = (\frac{\pi}{6}, \frac{\pi}{6})$, $\mathfrak{q} = (\frac{\pi}{2}, \frac{\pi}{6})$ and $\mathfrak{q} = (\frac{\pi}{3}, \frac{\pi}{3})$ are taken over by the closer modes of size four. The plots on the anti-diagonal, $\mathfrak{q} = (\frac{5\pi}{6}, \frac{\pi}{6})$ and $\mathfrak{q} = (\frac{2\pi}{3}, \frac{\pi}{3})$ are almost equal, except for some low temperature noise, probably

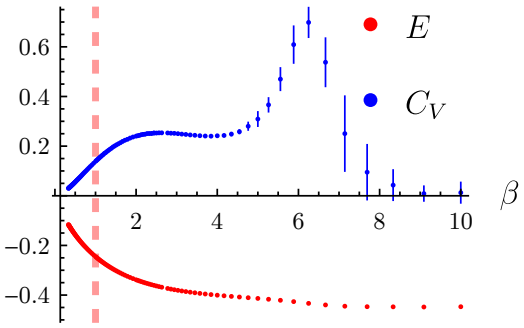

(A) Energy and specific heat. While the energy smoothly decreases, the specific heat exhibits a worth of two peaks.

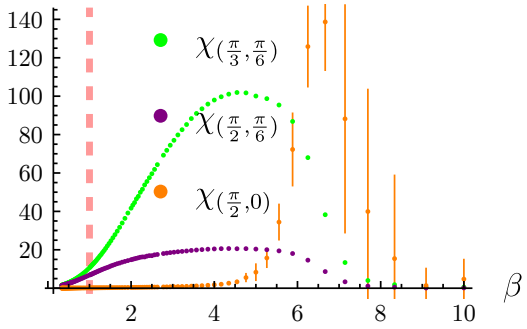

(B) Susceptibilities of the three arising order parameters. The suceptibilities of $\mathfrak{q} = (\frac{\pi}{3}, \frac{\pi}{6})$ and $\mathfrak{q} = (\frac{\pi}{2}, \frac{\pi}{6})$ are rescaled by a factor 25 and both peak roughly around $\beta \sim 4$. The susceptibility of $\mathfrak{q} = (\frac{\pi}{3}, 0)$ manifestly peaks at a different value.

FIGURE 6.10: Simulation details beyond the face defined by $\mathfrak{q} = (\frac{\pi}{3}, \frac{\pi}{6})$.

due to the aforementioned poor sampling. The behaviour beyond the transition resembles the trend observed for the mode $\mathfrak{q} = (\frac{3\pi}{4}, \frac{\pi}{4})$ on L_8, a superposition of the anti-diagonal harmonics dominated by the predicted one.

Thus, on L_{12} we recognise only two new interesting behaviours with respect to the previous lattices. The mode $(2\pi/3, \pi/6)$ has a subsequent phase transition to a phase defined by mode coexistence. The order parameters beyond the face defined by $\mathfrak{q} = (\frac{\pi}{3}, \frac{\pi}{6})$, have an intricate behaviour: the predicted mode is the first to emerge but with a very low and wide peak, its purple dots are hardly noticed. Next, two subsequent transitions take over, first to the mode $\mathfrak{q} = (\frac{\pi}{2}, \frac{\pi}{6})$ that vanishes when $\mathfrak{q} = (\frac{\pi}{2}, 0)$ finally arises. The above considerations are only partially confirmed by the susceptibilities and the specific heat, shown in Fig.6.10. In contrast to the order parameters shown in Fig.6.10b, we see three subsequent order parameters arising at three different temperatures, but the specific heat only has a double peak; this is still remarkable, as it is the first specific heat, that fully shows a double peak. The same trend is confirmed by the susceptibilities plots, shown in Fig.6.10b, where the susceptibility of the predicted mode and of the mode $\mathfrak{q} = (\frac{\pi}{2}, \frac{\pi}{6})$ are the first to simultaneously peak around $\beta \sim 4$, followed by the suceptibility of $\mathfrak{q} = (\frac{\pi}{2}, 0)$, that roughly peaks at $\beta \sim 6.5$. Moreover, it is worth to point out that for representation reasons, the first two susceptibilities have been rescaled by a factor 25, thus the susceptibility of $\mathfrak{q} = (\frac{\pi}{2}, \frac{\pi}{6})$, is ambiguous and further investigation should be required.

6.4 Discussion

Once again Monte Carlo simulations proved to be an important tool for empirically investigating the physics of the desired system. We succeeded in validating that the theoretical framework presented above fully retains the first modes peaking at the bifurcation surface. Furthermore, we moved the first steps in understanding the phenomenology beyond the polytope diagram. The only modes that appears to be stable

at low temperatures are the six phases of $\mathfrak{U}_4$. This might also be true for the simulations on L_6, nonetheless, as shown increasing the size up to $N = 12$, we clearly see that the commensurability with L_4, introduces a subsequent low temperature transition to its phases. Further investigations varying the size of the simulated systems will be required to understand the stability of these phases, in the outlook we will sketch a procedure that might more thoroughly shed light on this behaviour. Other than the low temperature stability we observed other behaviours induced by the mechanism of frustration due to competing anti-ferromagnetic interactions. This led to a variety of plots whose nature is unclear, also in this case more work need to be done. mention solution space

Chapter 7

Outlook

To address the empirical observations of the previous chapter, we present two open routes that might quantitatively shed light on the physics beyond the bifurcation surface. First, a mapping of the energy minimization problem to a maximum satisfiability (MAX-SAT) problem. Second, a first step towards a more general solution of the Mean Field self-consistency equations (Eq.4.13) that retains mode coexistence beyond the bifurcation surface.

7.1 Formulation as a MAX-SAT Problem

With a strong awareness on the geometrical structure of the phase diagram, we show introductory investigations that pave the way to a study of the ground states. Our attempt is incomplete and maybe even ill-posed. We relied on a recent technique [58], based on the separate convergence of an upper bound and a lower bound on the energy. The upper bound consists in a mapping of the the energy optimization problem to a maximum satisfiability (MAX-SAT) problem, a well studied approach to NP problems. A combinatorial NP solver that has the intrinsic advantage of proving the globality of the solution found. The lower bound is found within the framework of linear programming for which we refer to the original article. This approach, however, has an intrinsic and an practical problem. The intrinsic problem is that only a single solution is obtained, while the degeneracy of the ground states induced by frustration implies that large regions of phase space are still accessible at zero temperature and should therefore be studied with the appropriate tools. The practical problem lies in software compatibilities of the code provided in the paper which is now obsolete. The implementation of both techniques requires more time than that available for the present work, and we succeeded in replicating it only for the upper bound, which would in principle suffice. However, the absence of the lower bound often requires to run the algorithm for much longer times, making it of poor practical use. Nonetheless, our minor findings are still worth to report.

With respect to standard optimization techniques employed in statistical mechanics, e.g. Simulated Annealing or Genetic Algorithms, MAX-SAT solvers provide two major advantages. First, they formally prove the globality of the optimum found. Second, the yearly competition of MAX-SAT solver performances, guarantees the existence of open source, reliable and highly optimized algorithms. For our purposes,

we will use the library *open-wbo*[1], winner of the 2018 competition and available on github[78][79]. MAX-SAT algorithms, as open-wbo, or any of its competitors, are highly non-scalable and provide a viable tool to compute the ground states only for a limited cell size. For our purpose we have attempted to simulate systems up to $N = 6$. However, most of the configurations[2] did not converge on single core computations within 72 hours.

As a gentle introduction to the workings of the procedure, in Sec.7.1.1, we consider minimizing the energy of a single pair of spins. Next, in Sec.7.1.2, we generalize to the Hamiltonian of interest extending the energy mapping to the whole square lattice in PBC. In Sec.7.1.3, we present the meager results that we obtained, where we also conclude with a discussion on the nature of the ground states, relating our findings to previous results.

To introduce the maximum satisfiability problem, we adopt the standard notation: the operators $\wedge$, $\vee$ and $\neg$ respectively represent the AND, OR and NOT operators. Moreover, we identify the product of Boolean variables with the AND operator. Given a set of Boolean variables $\{s_1, \dots, s_n\}$, $s_i \in \{0, 1\}$, we define a disjunctive clause to be any disjunction of variables or their negation $d = \dots s_i \vee \dots \vee \neg s_j \vee \dots$ By conjunctive normal form, we mean a conjuction of disjunctive clauses, as exemplified in the following equation

$$f = (\dots s_i \vee \dots \vee \neg s_j \vee \dots) \wedge \dots \wedge (\dots s_k \vee \dots \vee \neg s_l \vee \dots), \tag{7.1}$$

and remind that any logic expression f can be rewritten in this form. If there exists a variable assignment such that f holds the value *True*, we say that f is satisfiable. The MAX-SAT problem[80] aims at finding the maximum number of disjunctive clauses that can simultaneously hold true in a formula written in conjunctive normal form. This description naturally reminds the definition of frustrated systems given in Sec.1, where the global energy minimum implies that some sites are not in their local ground states, i.e. not all bonds are simultaneously minimized.

7.1.1 Single Bond

To translate the energy minimization problem, into a Boolean optimization problem we employ the transformation $\sigma \to 2s - 1$, where $s \in \{0, 1\}$ is a Boolean variable. The energy of a single Ising bond takes the form

$$E = -J\sigma_1\sigma_2 = -J\left(4s_1 \wedge s_2 - 2s_1 - 2s_2 + 1\right). \tag{7.2}$$

So that

$$\min\{E\} = -|J| \max\{\text{sign}(J)(4s_1 \wedge s_2 - 2s_1 - 2s_2 + 1\}, \tag{7.3}$$

where to stress that the standard input of MAX-SAT solvers requires each disjunctive clause to have a positive weight we factorized $J = |J|\text{sign}(J)$. Making use of the

[1] See `http://sat.inesc-id.pt/open-wbo/`.

[2] Curiously, those for which the ground state is highly degenerate.

following identities

$$\begin{aligned} -s_1 \wedge s_2 &= (\neg s_1 \vee \neg s_2) - 1, \\ s_1 \wedge s_2 &= (s_1 \vee \neg s_2) + s_2 - 1, \\ s &= 1 - (\neg s)\,, \end{aligned} \tag{7.4}$$

we succeed in the purpose of writing the energy minimization problem in MAX-SAT form

$$\min E = \begin{cases} 5|J| - |J| \max\{4\,(s_1 \vee \neg s_2) + 2s_2 + 2\,(\neg s_1) - 5\} & J > 0 \\ 5|J| - |J| \max\{4\,(\neg s_1 \vee \neg s_2) + 2s_1 + 2s_2 - 5\} & J < 0 \end{cases}. \tag{7.5}$$

A simple truth table then yields the correct energy spectrum. For a ferromagnetic interaction, $J > 0$, we have the following

s_1	s_2	$s_1 \vee \neg s_2$	$\neg s_1$	$\neg s_2$	$4\,(s_1 \vee \neg s_2) + 2s_2 + 2\,(\neg s_1))$
0	0	1	1	1	6
1	0	1	0	1	4
0	1	0	1	0	4
1	1	1	0	0	6

, (7.6)

which yields the correct energy ground state $E = -J$ and the conclusion that the ground states are equivalently $(0,0)$ or $(1,1)$.

For anti-ferromagnetic interactions, $J < 0$, we have the following truth table

s_1	s_2	$\neg s_1 \vee \neg s_2$	$4\,(\neg s_1 \vee \neg s_2) + 2s_1 + 2s_2$
0	0	1	4
1	0	1	6
0	1	1	6
1	1	0	4

, (7.7)

which again yields the correct spectrum $E = -J$ for the equivalent ground states $(1,0)$ or $(0,1)$.

7.1.2 Square Lattice in PBC

Our final goal is minimizing the Hamiltonian of Eq.2.3. Once again, as a starting point, we consider the energy contribution per spin, Eq.2.6, which for convenience we remember here

$$\mathcal{E}(\sigma_{\mathrm{z}}) = -\frac{1}{2}\Big[J_1 \sum_{\mathrm{n}_1 \in \mathrm{N}_1} \sigma_{\mathrm{z}+\mathrm{n}_1} + J_2 \sum_{\mathrm{n}_1 \in \mathrm{N}_1} \sigma_{\mathrm{z}+\mathrm{n}_2} + J_3 \sum_{\mathrm{n}_1 \in \mathrm{N}_1} \sigma_{\mathrm{z}+\mathrm{n}_3}\Big]. \tag{7.8}$$

To begin, we focus on a single neighbourhood. Using Eq.7.5, the cluster energy contribution due to the neighbourhood N_1 only, takes the form

$$\mathcal{E}^{(1)}(s_{\mathrm{z}}) = \begin{cases} -\frac{1}{2}|J_1| \sum_{\mathrm{n}_1 \in \mathrm{N}_1} \Big[4\,(s_{\mathrm{z}} \vee \neg s_{\mathrm{z}+\mathrm{n}_1}) + 2s_{\mathrm{z}+\mathrm{n}_1} + 2\,(\neg s_{\mathrm{z}}) - 5\Big] & J_1 > 0 \\ -\frac{1}{2}|J_1| \sum_{\mathrm{n}_1 \in \mathrm{N}_1} \Big[4\,(\neg s_{\mathrm{z}} \vee \neg s_{\mathrm{z}+\mathrm{n}_1}) + 2s_{\mathrm{z}} + 2s_{\mathrm{z}+\mathrm{n}_1} - 5\Big] & J_1 < 0 \end{cases}. \tag{7.9}$$

For the purpose of using a MAX-SAT solver, we are now interested in writing the energy contribution with the minimal number of disjunctive clauses. To this end we sum over the whole lattice

$$E = \sum_{\mathrm{z}\in s_{\mathrm{L}}} \mathcal{E} = 10N(|J_1| + |J_2| + |J_3|) - 4\max\left\{\sum_{i,j}\left[|J_1|\mathcal{H}^{(1)} + |J_2|\mathcal{H}^{(2)} + |J_3|\mathcal{H}^{(3)}\right]\right\}, \tag{7.10}$$

where we factorized out the constant terms and where the spin dependent contributions $\mathcal{H}^{(i)}$ of the three neighbourhoods are

$$\begin{aligned}
\mathcal{H}^{(1)}(s_{\mathrm{L}}) &= \begin{cases} \sum_{\mathrm{z}\in s_{\mathrm{L}}}\left[s_{\mathrm{z}} + \neg s_{\mathrm{z}} + (s_{\mathrm{z}} \vee \neg s_{\mathrm{z}+\mathrm{e}_1}) + (s_{\mathrm{z}} \vee \neg s_{\mathrm{z}+\mathrm{e}_2})\right] & J_1 > 0 \\ \sum_{\mathrm{z}\in s_{\mathrm{L}}}\left[2s_{\mathrm{z}} + (\neg s_{\mathrm{z}} \vee \neg s_{\mathrm{z}+\mathrm{e}_1}) + (\neg s_{\mathrm{z}} \vee \neg s_{\mathrm{z}+\mathrm{e}_2})\right] & J_1 < 0 \end{cases}, \\
\mathcal{H}^{(2)}(s_{\mathrm{L}}) &= \begin{cases} \sum_{\mathrm{z}\in s_{\mathrm{L}}}\left[s_{\mathrm{z}} + \neg s_{\mathrm{z}} + (s_{\mathrm{z}} \vee \neg s_{\mathrm{z}+\mathrm{e}_1+\mathrm{e}_2}) + (s_{\mathrm{z}} \vee \neg s_{\mathrm{z}+\mathrm{e}_1-\mathrm{e}_2})\right] & J_2 > 0 \\ \sum_{\mathrm{z}\in s_{\mathrm{L}}}\left[2s_{\mathrm{z}} + (\neg s_{\mathrm{z}} \vee \neg s_{\mathrm{z}+\mathrm{e}_1+\mathrm{e}_2}) + (\neg s_{\mathrm{z}} \vee \neg s_{\mathrm{z}+\mathrm{e}_1-\mathrm{e}_2})\right] & J_2 < 0 \end{cases}, \\
\mathcal{H}^{(3)}(s_{\mathrm{L}}) &= \begin{cases} \sum_{\mathrm{z}\in s_{\mathrm{L}}}\left[s_{\mathrm{z}} + \neg s_{\mathrm{z}} + (s_{\mathrm{z}} \vee \neg s_{\mathrm{z}+2\mathrm{e}_1}) + (s_{\mathrm{z}} \vee \neg s_{\mathrm{z}+2\mathrm{e}_2})\right] & J_3 > 0 \\ \sum_{\mathrm{z}\in s_{\mathrm{L}}}\left[2s_{\mathrm{z}} + (\neg s_{\mathrm{z}} \vee \neg s_{\mathrm{z}+2\mathrm{e}_1}) + (\neg s_{\mathrm{z}} \vee \neg s_{\mathrm{z}+2\mathrm{e}_2})\right] & J_3 < 0 \end{cases},
\end{aligned} \tag{7.11}$$

both for a positive and a negative interaction. We considered that each pair of nearest neighbours will appear two times as a disjunction, while the unary terms will appear 4 times as a self contribution plus one time per each of the neighbours. Moreover, we notice that the ferromagnetic contribution can be further simplified using the identities of Eq.7.4. Finally, the ground state energy per spin of the system can be coincisely written as

$$\frac{1}{N}\min E = 10(|J_1| + |J_2| + |J_3|) - \frac{4}{N}\max\left\{\left[|J_1|\mathcal{H}^{(1)} + |J_2|\mathcal{H}^{(2)} + |J_3|\mathcal{H}^{(3)}\right]\right\}. \tag{7.12}$$

One last step needs to be taken into account to produce a usable input for a MAX-SAT solver, the weights all need to be lower than one. To do so, we divide the interaction energies by the maximum coupling, we rationalize the remaining two parameters and divide again by their GCD.

7.1.3 Ground States

As previously stressed, unfortunately, our procedure failed to converge even for lattices as small as L_6. Similarly to what we did in the Monte Carlo simulations, our choice of coupling parameters are the centroid of the faces. The ground states are shown in Fig.7.1. For the sake of completeness, when the MAX-SAT algorithm did not converge within reasonable time (more than 72 hours), the "ground states" presented are the minimum energy configurations found with the Monte Carlo simulations at $T = 0.1$. To further explore the effect of frustration on the ground state, we cross checked the individual energy contribution of each site with a direct calculation from the Hamiltonian of Eq.2.3. As expected, we found that some spins are free to oscillate without affecting the global energy. A behaviour similar to that observed by Wannier[29] on

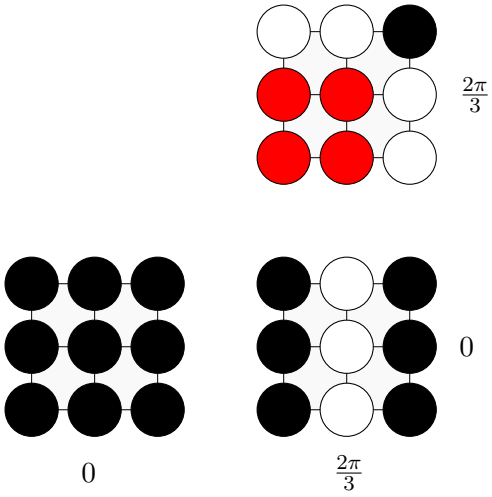

(A) Ground states of the three phases for $N = 3$. Ground state energies per spin are $\min E(0,0) = 0.5$, $\min E(\frac{2\pi}{3}, 0) = -0.41823$, $E(\frac{2\pi}{3}, \frac{2\pi}{3}) = -0.3348$.

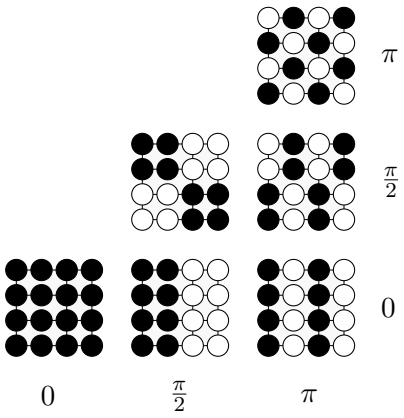

(B) Ground states of the six phases for $N = 4$. All the ground state energies per spin are $\min E(\mathfrak{q}_1, \mathfrak{q}_2) = 0.5$.

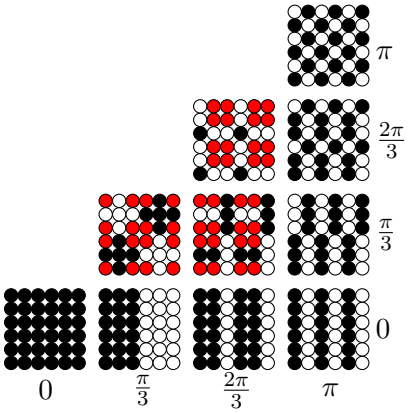

(C) Ground states of the ten phases for $N = 6$. Ground state energies per spin are $\min E(0,0) = -0.5$, $\min E(\frac{\pi}{3}, 0) = -0.467172$, $\min E^*(\frac{2\pi}{3}, 0) = -0.41823$, $\min E(\pi, 0) = -0.5$, $\min E^*(\frac{\pi}{3}, \frac{\pi}{3}) = -0.3348$, $\min E^*(\frac{2\pi}{3}, \frac{\pi}{3}) = -0.297517$, $\min E^*(\pi, \frac{\pi}{3}) = -0.41823$, $\min E^*(\frac{2\pi}{3}, \frac{2\pi}{3}) = -0.3348$, $\min E^*(\pi, \frac{2\pi}{3}) = -0.467172$, $\min E(\pi, \pi) = -0.5$.

FIGURE 7.1: Low energy states for the system on L_6: the states whose energy comes with a * are found with a Monte Carlo simulation, those coming without the * are exact ground states found with the methodology described above.
The free spins are emphasized in red.

the anti-ferromagnetic triangular lattice. If this is the case, the sites are colored in red.

In Fig.7.1b we show the ground states of L_4, which exactly match those previously found by Landau and Binder and already shown in Fig.2.3. This is coherent with the Monte Carlo simulations on L_4, presented in Sec.6.3.1, where the system converged without problems to the expected ground states. In Fig.7.1a we show the ground states[3] of L_3. The lattice is compatible with three phases only. The ferromagnetic phase is trivial. The phase $\mathfrak{q} = (\frac{2\pi}{3}, 0)$ is a striped pattern with two columns pointing in one direction and the third column in the opposite one. The ground state is degenerate with respect to the flip of one entire column (either the right or left black column of the figure). Phenomenologically speaking, the ground state should be static and the spins locked in their position by the surrounding spins. The third phase, $\mathfrak{q} = (\frac{2\pi}{3}, \frac{2\pi}{3})$, is characterized by four free spins that have a zero energy contribution to the Hamiltonian. We remark that the representation with four red sites might be misleading: it is true that each of the four spins can freely flip. However not independently, the flip of a single one of them would affect the energy contribution of the surrounding spins, thus changing the set of sites with zero energy contribution. The different behaviours may also explain the difference of the plots of Fig.6.4b and 6.5b, shown in the previous section.

In Fig.7.1c we show the ground states of L_6. In this case the algorithm converged only for the three corner modes. The other ground states have been taken as the lowest energy states found in the previously presented Monte Carlo simulations and it is not guaranteed (but reasonable to expect) that these are exact zero temperature configurations. The two states on the diagonal exploit the flipping spins, while the phases on the catheti are frustrated but with a locked-in configuration. Finally, we mention that the ground state of $\mathfrak{q} = (\pi, \frac{\pi}{3})$ has been recently reported in paper on iron chalchogenids[10], mentioned in the introduction.

In conclusion, we see two different aspects of frustration, already observed when comparing the Monte Carlo simulations of these two phases in the previous section. On the one hand, the phase $\mathfrak{q} = (\frac{2\pi}{3}, 0)$, exploits locally excited sites, but still with a definite globally locked ground state configuration. On the other hand, the zero energy contribution of certain sites in the $\mathfrak{q} = (\frac{2\pi}{3}, \frac{2\pi}{3})$ phase. This zero temperature fluid behaviour resembles the iconic anti-ferromagnetic triangular lattice studied by Wannier[29]. The above preliminary results are intriguing. In combination with a zero temperature Monte Carlo, new light may be shed on the elusive phenomenon of frustration.

7.2 Solution Space of the Mean Field Equations

In this final section, we introduce a promising route to formally address the observed mode coexistence. In Ch.4 we derived the Mean Field Approximation of the model under investigation with the aim of finding the region of stability of the paramagnetic phase with respect to all the possible modulations. Formally, we derived an infinite

[3] The choice of parameters in this case is the centroid of the faces of D_6 as the faces of D_3 are unbounded.

set of self-consistency equations (see Eq.4.13)

$$\tanh(\mathbf{K}\cdot\mathbf{M}(\mathrm{z},[m_{\mathrm{z}}])=m_{\mathrm{z}}, \tag{7.13}$$

whose trivial solution in the origin is $\mathrm{z}=0$ for all sites z. Next, we Taylor expanded the equations around a supposed bifurcation surface, to investigate whether and where these equations sustain other solutions. The positive answer is found in Fourier space, that lead to recognize the plane

$$\mathbf{K}\cdot\mathbf{F}(\mathrm{q})=1, \tag{7.14}$$

as the bifurcation surface toward the mode q. Thus, we proved that a solution of the self-consistency equation are the modulations $m_{\mathrm{q}}=\exp(i\langle \mathrm{q},\mathrm{z}\rangle)$. Coherently, we observed in the simulations, that the above wave systematically dominates over the others right beyond the first bifurcation surface. Nonetheless, nothing guarantees these to be an exhaustive set of solutions. This is confirmed by the results of the Monte Carlo simulations, that hint to the coexistence of multiple modes on a single phase. Thus, we aim to generalize the previously found solutions with two steps. First, we notice that the magnetization waves are eigenfunctions of the effective field

$$\mathbf{K}\cdot\mathbf{M}(\mathrm{z},[m_{\mathrm{q}}])=\mathbf{K}\cdot\mathbf{F}(\mathrm{q})m_{\mathrm{q}}. \tag{7.15}$$

Second, that the full Taylor expansion of the hyperbolic tangent

$$\tanh(x)=x-\frac{x^3}{3}+\frac{2x^5}{15}-\dots \tag{7.16}$$

has only odd powers, with the major consequence: first, that even products of the magnetization should always vanish; second, that it induces a natural map from the triple product of waves $m_{\mathrm{q}}m_{\mathrm{q}'}m_{\mathrm{q}''}$ to the sums $\mathrm{q}+\mathrm{q}'+\mathrm{q}''$ restricted to the (Symmetry Reduced) Brillouin Zone considered. The underlying reason being that higher odd powers can always be reduced to cubic powers recursively grouping triple products. Therefore, we can define a closure relation

$$C(\mathrm{q})=\{\mathrm{q}_l \mid \mathrm{q}_1=\mathrm{q},\mathrm{q}_l+\mathrm{q}_{l'}+\mathrm{q}_{l''}\in C(\mathrm{q})\}, \tag{7.17}$$

that could be recursively calculated. The dominant mode is found taking the first order Taylor expansion of the self consistency equations, while a more general solution exists and can be written as a linear combination of the waves within the solution space defined by the closure above

$$m_{\mathrm{z}}=\sum_{\mathrm{q}_l\in C(\mathrm{q})} a_l \exp i\langle \mathrm{q}_l,z\rangle. \tag{7.18}$$

The above procedure, if fully developed, might explain the behaviour observed beyond the bifurcation surfaces. However, without the claim that this might lead to the exhaustive set of phases.

Chapter 8

Conclusion

In short, the introduction of a range-3 coupling in the Ising model on the square lattice is sufficient for the stabilization of infinitely possible modulated phases that can be identified with the elements of the Brillouin Zone of the model. Following traditional arguments, we approximate the model in the MFT framework and solve the resulting self-consistency equations in Fourier space. To each solution corresponds a bifurcation surface in parameter space. To simplify the otherwise infinite phases that emerge in the model we developed a framework for the systematic enumeration of phases of increasing complexity. The crucial idea is that enforcing Periodic Boundary Conditions on the lattice limits the number of phases to a finite subset of the whole Brillouin Zone. With this simplification, the stability domain of the paramagnetic phase predicted by Mean Field Theory can be formally written as a convex polytope in half-space representation. To extract information on the boundaries of each phase on finite lattices we employed a Vertex Enumeration algorithm, only available since 2006, while, on the infinite lattice, we employed a convex body reconstruction. Next, we confirmed with Monte Carlo simulations that our theory correctly predicts the radial direction of the first phase transition in parameter space. The simulations hint at further intriguing physics beyond the first bifurcation surface in terms of subsequent phase transitions, modes coexistence and disparate low temperature phenomena induced by frustration. To this end, we propose two possible routes for further exploration: a mixture of MAX-SAT algorithm and zero temperature Monte Carlo, as well as, a more general solution to the self-consistency equations. The versatility of our method makes it applicable to any lattice on any dimension. Specifically, in future work, it might be interesting to revisit the triangular lattice anti-ferromagnet to address the phenomenon of frustration in its original context or revisit the ANNNI model to investigate the elusive devil's staircase.

Appendix A

Vertex enumeration

The mean field approximation, as derived in Ch.4, yields the domain of stability of the disordered phase in the shape of a convex polytope in the so-called H-representation. An implicit formulation of a polytope that does not provide direct information on the boundaries of the faces. A crucial step in the present work is to find the interval in phase space where a specific phase might emerge. In the present Appendix we briefly review the foundational notions of the problem, known as representation conversion problem. Interestingly, in its full generality the problem complexity still remains unknown. In Sec.A.1, we introduce the problem; in Sec.A.2 we mention the available algorithms and explain the reason of our choice; finally, in Sec.A.3 we describe our usage of the algorithm that required an extensive pre- and post-processing.

A.1 Representation Conversion Problem

The core result in the representation of convex polytopes is known as Minkowsky-Weil theorem[81]. Basically, it guarantees the existence of two equivalent representations for convex polytopes. The representation that naturally emerge the mean field derivation of Eq.4.29 is known as *half-space representation* (H-representation)

$$D = \{\mathbf{x} \in \mathbb{R}^N | A \cdot \mathbf{x} \geq \mathbf{c}\}, \tag{A.1}$$

where A is a $N \times N$ matrix, and $\mathbf{c}$ a vector of constants in $\mathbb{R}^N$. A system of inequalities whose common solutions define the body of the polyhedron. The complementary representation, known as *vertex representation* (V-representation) consists in the minimal[1] set of points (the vertices), whose convex hull defines the polyhedron.

For completeness we also mention that a polyhedron is *simple* if all its vertices share the same number of edges, else is called *degenerate*[81].

A.2 Algorithms

The conversion problem is a challenging problem. Many disparate algorithms have been historically proposed, all coming with advantages and disadvantages. These fall roughly in three different classes: *double description* method, *pivotal* algorithms[57]

[1]This definition holds for bounded convex polyhedra, if we wish to include generally unbounded convex polyhedra we should include the so-called extreme rays. Basically, the directors of the polyhedral cones.

and *lexicographic reverse search* method. The first two algorithms are older, their workings is rather intuitive (although the underlying theory is not) and well perform for simple polytopes. These algorithms do not perform well on degenerate polytopes as they have to either loop multiple times on the whole set of vertices or store a great amount of coordinates in memory. For the present purpose, the representation conversion of highly degenerate polytopes, the necessary choice was the lrs algorithm, developed in 2006 by Avis and Fukuda, whose drawback is the complexity of the underlying workings, for which we refer the reader either to [56] or to [55]. Although very efficient, its usage does not come for free, as we will see in the following section.

A.3 Usage of lrs library

Three mutually non parallel planes meet exactly on a single point. A vertex can nonetheless arise as the intersection of multiple planes, this is the case for example for the multicritical vertices (see Sec.5.3). The intrinsic usage of integer arithmetic, on which the lrs algorithm is based on, is problematic. We want to run the lrs algorithm over half-spaces defined by Eq.4.16, whose coefficents are irrational. The required rationalization would tilt the half-spaces by an arbitrarily small amount in an unpredictable direction, different for each face. All the information of vertices arising from multiple faces is lost. Rationalization gives rise to the appearance of a multitude of *spurious vertices* in the surrounding of the position of those exact vertices resulting from the intersection of more than three inequalities.

The problem is easily circumvented applying the following prescription which makes use of some exact results of Ch.5: first one rationalizes the half-space coefficients, appropriately choosing the degree of accuracy. A preliminary run of the algorithm, computing all reciprocal vertex distances, allows to identify the proper distance threshold under which the depicted shifting might occur[2]. Most of the distances are typically lower than 10^{-5}, some of them however might be some orders of magnitude lower. The higher the size of the underlying lattice, the lower may be the distance among vertices. Up to D_{32}, we identify a good distance threshold to be in between the two orders of magnitude reported in the last two columns of Tab.A.1.

Any pair of vertices, whose distance lies in the reported range, should be manually controlled to verify whether they do or do not coincide, this procedure can be heavily reduced introducing exact knowledge on the polyhedron, which allows to identify three sources of spurious vertices: those arising from the multicritical vertices (see Sec.5.3), those emerging on the front edge (see Sec.5.4.2) and those related to the linear ordering (see Sec.5.8).

The vast majority of the spurious vertices appear around the multicritical vertices. As shown in table A.1 per each of the three multicritical vertex, rationalization introduces exactly $n-1$ spurious vertices, where n is the number of inequalities that meet in such vertex. The fan structure implies that the minimum distance in between a multicritical point and its closer neighbour is about $d \sim 0.1$, which makes them easy to identify.

[2]This is a rule thumb. The typical degree of rationalization of the order of 10^{-20} and we do not reasonably expect the vertices to be shifted by more than 10^{-7} units.

N	F	V	E	V_M	V_E	V_A	$\min d$	$\max d$
4	6	8	12	2	0	0	-1	na
6	10	13	21	3	0	0	-1	na
8	14	18	30	4	2	0	-2	na
10	20	27	45	5	2	0	-2	na
12	26	36	60	6	4	0	-2	na
14	34	49	81	7	4	0	-3	na
16	42	62	102	8	6	0	-3	na
18	52	77	127	9	6	2	-3	-17
20	62	94	154	10	8	2	-3	-16
22	74	117	189	11	8	0	-4	na
24	86	134	218	12	10	4	-3	-17
26	100	163	261	13	10	0	-4	na
28	114	188	300	14	12	0	-4	na
30	130	215	343	15	12	2	-4	-16
32	146	246	390	16	14	0	-5	na

TABLE A.1: Polyhedra data for the first 14 sets. Where N is the maximum size of periodicity allowed; F the number of faces; V the number of vertices; E the number of edges; V_M the number of spurious vertices per each critical point; V_E the number of spurious vertices found around the edge; V_A the number of pairs of spurious vertices that have to be controlled analytically; $\min d$, magnitude the minimum vertex distance above the applied threshold; $\max d$ magnitude of the maximum vertex distance below the applied threshold.

The second major source for spurious vertices are the anti-diagonal faces, all tangent to the common edge parallel to $K_2 = K_3 = 0$. This case is slightly different: rationalization might shift the spurious vertices anywhere on the surrounding of the edge, to spot them is necessary to introduce a distance control on the edge rather then on its extremes. In this case we find exactly two spurious vertices per missing face, as shown in table A.1.

The rest of the pairs of spurious vertices, when present, could appear anywhere around the seam and have to be analytically controlled one by one. It is worth to stress that all of them turned out to be spurious. However, this might not be a general behaviour and a manual check is required. The adjacency graphs of the dual polyhedra resulting from this prescription are reported in figure 5.6.

Bibliography

[1] Yoshiaki Itoh and Sumie Ueda. The ising model for changes in word ordering rules in natural languages. *Physica D: Nonlinear Phenomena*, 198(3):333–339, 2004.

[2] Alexandre Feller and Etera R Livine. Ising spin network states for loop quantum gravity: a toy model for phase transitions. *Classical and Quantum Gravity*, 33(6):065005, feb 2016.

[3] Gemma De las Cuevas and Toby S. Cubitt. Simple universal models capture all classical spin physics. *Science*, 351(6278):1180–1183, 2016.

[4] J. Von Boehm and Per Bak. Devil's stairs and the commensurate-commensurate transitions in CeSb. *Physical Review Letters*, 42(2):122–125, 1979.

[5] Per Bak and J. von Boehm. Ising model with solitons, phasons, and "the devil's staircase". *Phys. Rev. B*, 21:5297–5308, Jun 1980.

[6] Chad A. Mirkin, Robert L. Letsinger, Robert C. Mucic, and James J. Storhoff. A dna-based method for rationally assembling nanoparticles into macroscopic materials. *Nature.*, 382:607–609, 1996.

[7] R. Comès, S. M. Shapiro, G. Shirane, A. F. Garito, and A. J. Heeger. Neutron-scattering study of the 38- and 54-k phase transitions in deuterated tetrathiafulvalene- tetracyanoquinodimethane (ttf-tcnq). *Phys. Rev. Lett.*, 35:1518–1521, Dec 1975.

[8] J. M. Hastings, J. P. Pouget, G. Shirane, A. J. Heeger, N. D. Miro, and A. G. MacDiarmid. One-dimensional phonons and "phase-ordering" phase transition in $hg_{3-\delta}Asf_6$. *Phys. Rev. Lett.*, 39:1484–1487, Dec 1977.

[9] R. J. Elliott. Phenomenological discussion of magnetic ordering in the heavy rare-earth metals. *Phys. Rev.*, 124:346–353, Oct 1961.

[10] J. K. Glasbrenner, I. I. Mazin, Harald O. Jeschke, P. J. Hirschfeld, R. M. Fernandes, and Roser Valentí. Effect of magnetic frustration on nematicity and superconductivity in iron chalcogenides. *Nature Physics*, 11(11):953–958, 11 2015.

[11] Johannes Bausch, Toby S. Cubitt, and James D. Watson. Uncomputability of phase diagrams. *Nature Communications*, 12(1):452, 2021.

[12] Simon H. Tindemans and Bela M. Mulder. Designing colloidal ground-state patterns using short-range isotropic interactions. *Phys. Rev. E*, 82:021404, Aug 2010.

[13] Ernst Ising. Beitrag zur Theorie des Ferromagnetismus. *Zeitschrift für Physik*, 31(1):253–258, 2 1925.

[14] Whilelm Lenz. Beiträge zum Verständnis der magnetischen Eigenschaften in festen Körpern. *Physikalische Zeitschrift*, 21:613, 1920.

[15] Stephen G. Brush. History of the lenz-ising model. *Rev. Mod. Phys.*, 39:883–893, Oct 1967.

[16] P. W. Anderson. More is different. *Science*, 177(4047):393–396, 1972.

[17] Robert J. Birgeneau and Gen Shirane. Magnetism in one dimension. *Physics Today*, 31(12):32, 1977.

[18] W. L. Bragg and E. J. Williams. The effect of thermal agitation on atomic arrangement in alloys. *Proc. Soc. London A*, 145:730, 1934.

[19] R. Peierls. On ising's model of ferromagnetism. *Mathematical Proceedings of the Cambridge Philosophical Society*, 32(3):477–481, 1936.

[20] Robert B. Griffiths. Peierls proof of spontaneous magnetization in a two-dimensional ising ferromagnet. *Phys. Rev.*, 136:A437–A439, Oct 1964.

[21] N. D. Mermin and H. Wagner. Absence of ferromagnetism or antiferromagnetism in one- or two-dimensional isotropic heisenberg models. *Phys. Rev. Lett.*, 17:1133–1136, Nov 1966.

[22] Lars Onsager. Crystal statistics. i. a two-dimensional model with an order-disorder transition. *Phys. Rev.*, 65:117–149, Feb 1944.

[23] Bruria Kaufman. Crystal statistics. ii. partition function evaluated by spinor analysis. *Phys. Rev.*, 76:1232–1243, Oct 1949.

[24] Bruria Kaufman and Lars Onsager. Crystal statistics. iii. short-range order in a binary ising lattice. *Phys. Rev.*, 76:1244–1252, Oct 1949.

[25] C. N. Yang. The spontaneous magnetization of a two-dimensional ising model. *Phys. Rev.*, 85:808–816, Mar 1952.

[26] Louis Néel. Antiferromagnetism and ferrimagnetism. *Proceedings of the Physical Society. Section A*, 65(11):869–885, nov 1952.

[27] G. Toulouse. *Theory of the frustration effect in spin glasses: I*, pages 99–103. World Scientific, 1986.

[28] J Vannimenus and G. Toulouse. Theory of the frustration effect in spin glasses. ii. ising spins on a square lattice. *J. Phys. C: Solid State Phys.*, 10(L537), 1977.

[29] G. H. Wannier. The Triangular Ising Net. *Phys. Rev.*, 79(2):357, 1950.

[30] H T Diep. *Frustrated Spin Systems*. World Scientific, 2013.

[31] S Aubry. Exact models with a complete devil's staircase. *Journal of Physics C: Solid State Physics*, 16(13):2497–2508, may 1983.

[32] Walter Selke and Michael E. Fisher. Spatially Modulated phase in ising models with competing interactions. *Journal of Magnetism and Magnetic Materials*, 15-18(PART 1):403–404, 1980.

[33] Michael E. Fisher and Walter Selke. Infinitely many commensurate phases in a simple ising model. *Phys. Rev. Lett.*, 44:1502–1505, Jun 1980.

[34] R. J. Elliott. Modulated structure materials. *Proceedings of the NATO Advanced Study Institute*, Jun 1983.

[35] T. Janssen and A. Janner. Incommensurability in crystals. *Advances in Physics*, 36:519–624, 1987.

[36] H. Mashiyama. Spatially modulated phases in an Ising model with effectively long-range interactions. *Journal of Physics C: Solid State Physics*, 16(1):187–201, 1983.

[37] S. Redner. One-dimensional Ising chain with competing interactions: Exact results and connection with other statistical models. *Journal of Statistical Physics*, 25(1):15–23, 1981.

[38] Filipe C. Thewes and Heitor C.M. Fernandes. Phase transitions in hardcore lattice gases on the honeycomb lattice. *arXiv*, 2020.

[39] M. Grousson, G. Tarjus, and P. Viot. Phase diagram of an Ising model with long-range frustrating interactions: A theoretical analysis. *Physical Review E - Statistical Physics, Plasmas, Fluids, and Related Interdisciplinary Topics*, 62(6):7781–7792, 2000.

[40] Bram Vanhecke, Jeanne Colbois, Laurens Vanderstraeten, Frank Verstraete, and Frédéric Mila. Solving frustrated ising models using tensor networks. *Phys. Rev. Research*, 3:013041, Jan 2021.

[41] Wenxuan Huang, Daniil A. Kitchaev, Stephen T. Dacek, Ziqin Rong, Alexander Urban, Shan Cao, Chuan Luo, and Gerbrand Ceder. Finding and proving the exact ground state of a generalized Ising model by convex optimization and MAX-SAT. *Physical Review B*, 94(13):1–12, 2016.

[42] Robert H. Swendsen and Samuel Krinsky. Monte carlo renormalization group and ising models with uuuuuuuuuuu. *Phys. Rev. Lett.*, 43:177–180, Jul 1979.

[43] Rosana A. dos Anjos, J. Roberto Viana, and J. Ricardo de Sousa. Phase diagram of the Ising antiferromagnet with nearest-neighbor and next-nearest-neighbor interactions on a square lattice. *Physics Letters, Section A: General, Atomic and Solid State Physics*, 372(8):1180–1184, 2008.

[44] D. P. Landau. Phase transitions in the Ising square lattice with next-nearest-neighbor interactions. *Physical Review B*, 21(3):1285–1297, 2 1980.

[45] J. L. Morán-López, F. Aguilera-Granja, and J. M. Sanchez. First-order phase transitions in the Ising square lattice with first- and second-neighbor interactions. *Physical Review B*, 48(5):3519–3522, 8 1993.

[46] Songbo Jin, Arnab Sen, Wenan Guo, and Anders W. Sandvik. Phase transitions in the frustrated Ising model on the square lattice. *Physical Review B - Condensed Matter and Materials Physics*, 87(14):1–12, 2013.

[47] D. P. Landau and K. Binder. Phase diagrams and critical behavior of Ising square lattices with nearest-, next-nearest-, and third-nearest-neighbor couplings. *Physical Review B*, 31(9):5946–5953, 1985.

[48] R. M. Liu, W. Z. Zhuo, S. Dong, X. B. Lu, X. S. Gao, M. H. Qin, and J. M. Liu. Role of further-neighbor interactions in modulating the critical behavior of the Ising model with frustration. *Physical Review E*, 93(3):032114, 3 2016.

[49] Makoto Kaburagi. Ground State Structure of Adsorbates on the Square Lattice Net with up to 3rd Neighbor Interactions. *Journal of the Physical Society of Japan*, 44(1):54–62, 1978.

[50] Junjiro Kanamori and Makoto Kaburagi. Exact Ground States of the Lattice Gas and the Ising Model on the Square Lattice. *Journal of the Physical Society of Japan*, 52(12):4184–4191, 12 1983.

[51] Junjiro Kanamori. Magnetization Process in an Ising Spin System. *Progress of Theoretical Physics*, 35(1):16–35, 1 1966.

[52] Kiyoshi Teramoto and Yoshimasa Itoh. A New Method of Deriving Inequalities to Determine the Ground State of the Lattice Gas. *Progress of Theoretical Physics*, 77(5):1125–1140, 05 1987.

[53] U. Brandt. Ground-state properties of a 2-dimensional Ising-system with competing interactions. *Zeitschrift für Physik B Condensed Matter*, 53(4):283–287, 1983.

[54] F. A. Kassan-Ogly, A. K. Murtazaev, A. K. Zhuravlev, M. K. Ramazanov, and A. I. Proshkin. Ising model on a square lattice with second-neighbor and third-neighbor interactions. *Journal of Magnetism and Magnetic Materials*, 384:247–254, 2015.

[55] David Avis and Charles Jordan. mplrs: A scalable parallel vertex/facet enumeration code. *Mathematical Programming Computation*, 10(2):267–302, 6 2018.

[56] David Avis and Charles Jordan. Comparative computational results for some vertex and facet enumeration codes. *Science Open*, 10 2015.

[57] David Avis and Komei Fukuda. A pivoting algorithm for convex hulls and vertex enumeration of arrangements and polyhedra. *Discrete & Computational Geometry*, 8(1):295–313, 12 1992.

[58] Wenxuan Huang, Daniil A. Kitchaev, Stephen T. Dacek, Ziqin Rong, Alexander Urban, Shan Cao, Chuan Luo, and Gerbrand Ceder. Finding and proving the exact ground state of a generalized Ising model by convex optimization and MAX-SAT. *Physical Review B*, 94(13):134424, 10 2016.

[59] D. P. Landau and K. Binder. Phase diagrams and critical behavior of Ising square lattices with nearest-, next-nearest-, and third-nearest-neighbor couplings. *Physical Review B*, 31(9):5946–5953, 5 1985.

[60] C Hermite. Sur l'introduction des variables continues dans la théorie des nombres. *Journal für die reine und angewandte Mathematik*, 41:191–216, 1851.

[61] Manfred R. Schroeder. *Number Theory in Science and Communication*, volume 7 of *Springer Series in Information Sciences*. Springer Berlin Heidelberg, Berlin, Heidelberg, 1997.

[62] Jörg Schulte. über die jordansche verallgemeinerung der eulerschen funktion. *Results in Mathematics*, 36:354–364, 1999.

[63] C. Jordan. Traitee de substitutions et des equations algebriques. *Gauthier-Yillars*, 1957.

[64] D. Andrica and M. Piticari. On some extensions of jordan's arithmetic functions. *Proceedings of the International Conference on Theory and Applications of Mathematics and Informatics*, 13, 2003.

[65] J. H. Conway, H. Burgiel, and C. Goodman-Strauss. *The symmetries of things*. Wellesley, Mass: A.K. Peters, 2008.

[66] G. Parisi. *STATISTICAL FIELD THEORY*. CRC Press, 1988.

[67] Kerson Huang. *Statistical Mechanics*. John Wiley & Sons, 2 edition, 1987.

[68] R.K. Pathria. *Statistical Mechanics*. International series of monographs in natural philosophy. Elsevier Science & Technology Books, 1972.

[69] R. J. Baxter. *Exactly solved models in statistical mechanics*. Dover Publications, 1982.

[70] P. Weiss. L'hypothèse du champ moléculaire et la propriété ferromagnétique. *J. Phys. Theor. Appl.*, 6:661–690, 1907.

[71] Branko Grünbaum, Volker Kaibel, Victor Klee, and Günter M. Ziegler. *Convex polytopes*. Springer, New York, 2003.

[72] lrslib, Version 7.1.

[73] Mathematica, Version 12.1.

[74] Dirk Jan Struik. *Lectures on Classical Differential Geometry*. Courier Corporation, 1961.

[75] Manfredo P. do Carmo. *Differential geometry of curves and surfaces*. Prentice Hall, 1976.

[76] N. Metropolis, A.W. Rosenbluth, M.N. Rosenbluth, A.H. Teller, and E. Teller. Equation of state calculations by fast computing machines. *Journal of Chemical Physics*, 21:1087–1092, 1953.

[77] M. E. J. Newman and G. T. Barkema. *Monte Carlo methods in statistical physics*. Clarendon Press, Oxford, 1999.

[78] open-wbo.

[79] Ruben Martins, Vasco Manquinho, and Inês Lynce. Open-wbo: A modular maxsat solver,. In Carsten Sinz and Uwe Egly, editors, *Theory and Applications of Satisfiability Testing – SAT 2014*, pages 438–445, Cham, 2014. Springer International Publishing.

[80] Vijay V. Vazirani. *Approximation Algorithms*. Springer Publishing Company, Incorporated, 2010.

[81] Komei Fukuda. Lecture: Polyhedral Computation, Spring 2016. *Lecture Notes*, 2016.